DESIGN AND ANALYSIS OF ARTIFACT-RESISTIVE FINGER PHOTOPLETHYSMOGRAPHIC SENSORS FOR VITAL SIGN MONITORING

by

Sokwoo Rhee

B.S., Mechanical Engineering
Seoul National University, Korea (1995)

M.S., Mechanical Engineering
Massachusetts Institute of Technology (1997)

Submitted to the Department of Mechanical Engineering
in Partial Fulfillment of the Requirements for the Degree of

Doctor of Philosophy

at the

Massachusetts Institute of Technology

June 2000

Signature of Author _____
Department of Mechanical Engineering
May 8, 2000

Certified by _____
Harry H. Asada
Professor of Mechanical Engineering
Thesis Supervisor

Certified by _____
Boo-Ho Yang
Research Scientist of Mechanical Engineering
Thesis Co-supervisor

Accepted by _____
Ain A. Sonin
Chairman, Department Committee on Graduate Students

DESIGN AND ANALYSIS OF ARTIFACT-RESISTANT FINGER PHOTOPLETHYSMOGRAPHIC SENSORS FOR VITAL SIGN MONITORING

by

Sokwoo Rhee

Submitted to the Department of Mechanical Engineering
On May 8, 2000, in Partial Fulfillment of the
Requirements for the Degree of Doctor of Philosophy
in Mechanical Engineering

ABSTRACT

A miniaturized, telemetric, photoplethysmograph sensor for long-term, continuous monitoring is presented in this thesis. The sensor, called a "ring sensor," is attached to a finger base for monitoring beat-to-beat pulsation, and the data is sent to a host computer via a RF transmitter. Two major design issues are addressed: one is to minimize motion artifact and the other is to minimize the consumption of battery power. An efficient double ring design is developed to lower the influence of external force, acceleration, and ambient light, and to hold the sensor gently and securely on the skin, so that the circulation at the finger may not be obstructed. To better understand the mechanism of motion artifact by external forces, a comprehensive mathematical model describing the finger photoplethysmography was developed and verified by finite element method, numerical simulation and experiments. Total power consumption is analyzed in relation to the characteristics of the individual components, sampling rate, and CPU clock speed. Optimal operating conditions are obtained for minimizing the power budget. A prototype ring sensor is designed and built based on the power budget analysis and the artifact-resistive attachment method. It is verified through experiments that the ring sensor is resistant to interfering forces and acceleration acting on the ring body. It is also shown that the device meets diverse and conflicting requirements, including compactness, motion artifact reduction, minimum loading effects, and low battery power consumption. Benchmarking tests with FDA-approved photoplethysmograph and EKG reveal that the ring sensor is comparable to those devices in detecting beat-to-beat pulsation despite disturbances. The long-term monitoring experiment shows that this device can effectively provide a considerable amount of artifact-free vital sign information in everyday life. Finally, guidelines for designing the ring sensor are proposed based on the analyses and the experiment results.

Thesis Committee Members:
Professor Harry H. Asada, Chairman
Professor Roger D. Kamm
Professor Roger G. Mark
Dr. Boo-Ho Yang

To My Lovely Family…

Acknowledgements

It has already been five years since I stood in front of the main gate of MIT for the first time. During that time, so many things have happened to me. Some of them were very exciting and delighting, and some of them were sad and discouraging. After all, I am so glad that I could finish my Ph.D. work and write this thesis.

Most of all, I would like to express my best and sincere thanks to my thesis advisor, Professor Harry H. Asada, for his constant encouragement and guidance. His profound insight and splendid wide vision gave me a great chance to get into the world of new research directions. His valuable support and advice were the greatest factor that enabled me to write this thesis. I also would like to express deep gratitude to the thesis committee members: Professor Roger D. Kamm, Professor Roger G. Mark, and Dr Boo-Ho Yang. They guided and helped me a lot in my research, and contributed greatly to my thesis.

I would like to express thanks to all my lab-mates in d'Arbeloff Laboratory who showed me sincere friendship and care. Also I would like to express deep thanks to the continuous support of my good friends, especially Sangjun Han and Andy S. Kim. They made my life more energetic and enjoyable while I was going through a hard time struggling to make progress in my research. In addition, I would like to say thanks to all my friends at MIT.

Finally, I would like to give my best appreciation to my lovely wife, Eunkyoung Um. She has always been a great supporter of my work. I also would like to say thanks to my parents and my sister, who have been watching me with great love. Their love and care have been the main source of energy that has encouraged me throughout my life at MIT.

Even after I graduate from MIT, I will not be able to forget this wonderful school, and I think what MIT has taught me these five years will be the major thrust that will guide me through the rest of my life.

Contents

1. INTRODUCTION 9

1.1 BACKGROUND AND OBJECTIVES 9
1.2 PRIOR WORK IN THE FIELD 10
1.3 OUTLINE OF THESIS 11

2. THE RING SENSOR 14

2.1 BASIC DESCRIPTION OF THE RING SENSOR 14
2.2 ISSUES 15

3. ARTIFACT-RESISTANT DESIGN 17

3.1 ISOLATING RING ARCHITECTURE 17
3.2 MOVEMENT DETECTION BY SOFTWARE 19
3.3 MOVEMENT DETECTION USING ACCELEROMETER 19

4. POWER SAVING ELECTRONICS DESIGN 21

4.1 DESCRIPTION OF THE BASIC CIRCUITRY 21
4.2 POWER BUDGET 22

5. THEORETICAL ANALYSIS OF FINGER PHOTOPLETHYSMOGRAPHY WITH RING SENSOR 26

5.1 BACKGROUND 26
5.2 APPROACH 27
5.3 MODELING 29
5.3.1 Optical Model 29
5.3.2 Tissue Mechanical Model 32
5.3.3 Dynamics of the Arterial Wall 36
5.3.4 Parameter Calibration and Estimation 39
5.3.4.1 Validation of the Model and Determination of Stiffness of the Tissue by FEM 39
5.3.4.2 Determination of Optical Properties : Capillaries and Veins 41
5.3.5 Completing the Blood Vessel Model 46
5.4 VERIFICATION BY FINITE ELEMENT METHOD, NUMERICAL SIMULATION AND EXPERIMENT 47
5.4.1 Analysis of the Simulation and Experiment : Case 1 48
5.4.2 Analysis of the Simulation and Experiment : Case 2 51
5.5 VERIFICATION OF ADVANTAGES OF THE ISOLATING RING SENSOR BY FINITE ELEMENT METHOD 53

6. SIGNAL PROCESSING WITH CORRELATION FUNCTIONS 57

6.1 BACKGROUND 57
6.2 THEORY 58
6.2.1 General Description of the Signal Conditioning Process 58
6.2.2 Theoretical Description of the Autocorrelation Function 59
6.3 NUMERICAL SIMULATION 63
6.4 EXPERIMENT 65
6.4.1 Experiment Setup 65

6.4.2 Experiment Results *67*

7. PROTOTYPING AND FABRICATION **68**

7.1 PACKAGING 68
7.2 ELECTRONIC COMPONENT SELECTION 69
7.3 THE POWER-OPTIMAL CLOCK FREQUENCY 70
7.4 SOFTWARE DESIGN 72
7.4.1 Software for the Microprocessor on the Ring Side *72*
7.4.2 Software for the Host Computer with Artifact Detection *72*

8. MINIATURIZATION **74**

8.1 BACKGROUND 74
8.2 ISSUES OF MINIATURIZATION 75
8.2.1 How do we reduce size? *75*
8.2.2 What kind of circuit boards will we use? *77*
8.2.3 How do we reduce the power consumption from the viewpoint of hardware? *77*
8.3 PROCESS OF FABRICATION 78
8.3.1 Finalize the circuit and collect the necessary components. *78*
8.3.2 Design a conducting pattern to be put on the ceramic substrate or the printed circuit board. . *79*
8.3.3 Make the circuit board using gold as the conducting material *79*
8.3.4 Put the components on the board and make connections *79*
8.3.5 Do external wirings and debugging *80*
8.3.6 Software – In circuit Programming *80*

9. VERIFICATION AND BENCHMARKING **82**

9.1 SOFTWARE-BASED ARTIFACT DETECTION 82
9.2 ADJUSTMENT OF INNER RING TENSION AND CONTACT PRESSURE 83
9.3 COMPARISON BETWEEN THE ISOLATING RING AND A NON-ISOLATING RING 85
9.4 BENCHMARKING 87
9.5 LONG-TERM MONITORING EXPERIMENT 91
9.6 DESIGN GUIDELINES FOR THE RING SENSOR 92

10. CONCLUSIONS **96**

REFERENCES **98**

List of Figures & Tables

Figure 2-1	Conceptual diagram of the ring sensor
Figure 3-1	Dislocation of ring sensors due to external load
Figure 3-2	Construction of isolating ring
Figure 3-3	Various Signals Detected by the Ring
Figure 3-4	Detection of movement by 3-D accelerometer
Figure 4-1	Block diagram of electronic circuit
Figure 5-1	(a) Uncompressed finger under no external force (d=0). (b) Finger compressed by the ring due to an external force.(d>0)
Figure 5-2	Optical model of the finger and optical elements. Blood vessels have different optical properties from the tissue.
Figure 5-3	(a) Initial state of the ring with LED and photodetector (b) When the finger moves in the ring (Finger tissue is deformed.)
Figure 5-4	Geometry of the LED, the photodetector, artery 1, and the skin capillary layer
Figure 5-5	Change of arterial wall radius (Rr) with transmural pressure (Pt)
Figure 5-6	Pressure-diameter relationship of human digital artery
Figure 5-7	Pressure-diameter relation curve described by sigmoid function
Figure 5-8	Finite element analysis of the finger segment under constant pressure of 120 mmHg.
Figure 5-9	Deformed finger segment under external pressure, generated by FEM.
Figure 5-10	Volumetric changes of the finger segment with various values for Young's modulus.
Figure 5-11	FEM Analysis : Single Ring : E=20000, v=0.49, disp=2mm, angle=90 deg
Figure 5-12	FEM Analysis : Single Ring : E=20000, v=0.49, disp=2mm, angle=20 deg
Figure 5-13	Single Ring : E=20000, v=0.49, disp=2mm, angle=90 deg, 3-D View
Figure 5-14	Single Ring : E=20000, v=0.49, disp=2mm, angle=90 deg, Cross Sectional View at x=0
Figure 5-15	Simultaneous recordings of chamber pressure (P_{ch}), AC components of impedance variation (ΔZ), and DC components of the impedance variation (Z_o).
Figure 5-16	Numerical simulation result of the volume change (AC components) of 1 cm finger segment under external pressure
Figure 5-17	Numerical simulation result of the volume change (DC components) of 1 cm finger segment under external pressure
Figure 5-18	Two cases of finger movements in the ring
Figure 5-19	Visualization of movement at case 1
Figure 5-20	Single Ring – 3-D View : E=20000, v=0.49, disp=2mm, angle=20 deg
Figure 5-21	Single Ring : E=20000, v=0.49, disp=2mm, angle=20 deg, Cross sectional view at x=0
Figure 5-22	Pressure distribution as a function of angle in the finger cross section generated by the lumped parameter model.
Figure 5-23	Pressure distribution as a function of angle in the finger cross section generated by finite element method.
Figure 5-24	Photoplethysmography and pressure at sensor unit from experiment in case 1
Figure 5-25	Photoplethysmography and pressure at sensor unit from numerical simulation in case 1
Figure 5-26	Pressure distribution as a function of angle in the finger cross section generated by the lumped parameter model.
Figure 5-27	Pressure distribution as a function of angle in the finger cross section generated by finite element method.
Figure 5-28	Visualization of movement at case 2.
Figure 5-29	Photoplethysmography and pressure at sensor unit from experiment in case 2
Figure 5-30	Photoplethysmography and pressure at sensor unit from numerical simulation in case 2

Figure 5-31 FEM Analysis : Isolating Ring : E=20000, v=0.49, disp=2mm, angle=90 deg
Figure 5-32 FEM Analysis : Isolating Ring : E=20000, v=0.49, disp=2mm, angle=20 deg
Figure 5-33 Isolating Ring : E=20000, v=0.49, disp=2mm, angle=90 deg, 3-D View
Figure 5-34 Isolating Ring : E=20000, v=0.49, disp=2mm, angle=90 deg, Cross Sectional View at x=0
Figure 5-35 Isolating Ring : E=20000, v=0.49, disp=2mm, angle=90 deg, Cross Sectional View at the Outer Ring
Figure 5-36 Isolating Ring : E=20000, v=0.49, disp=2mm, angle=90 deg, Longitudinal View
Figure 5-37 Isolating Ring : E=20000, v=0.49, disp=2mm, angle=20 deg, 3-D View
Figure 5-38 Isolating Ring : E=20000, v=0.49, disp=2mm, angle=20 deg, Cross Sectional View at x=0
Figure 5-39 Isolating Ring : E=20000, v=0.49, disp=2mm, angle=20 deg, Cross Sectional View at the Outer Ring
Figure 5-40 Isolating Ring : E=20000, v=0.49, disp=2mm, angle=20 deg, Longitudinal Cut-Plane View
Figure 5-41 Isolating Ring : E=20000, v=0.49, disp=2mm, angle=90 deg, Wide Ring, 3-D View
Figure 5-42 Isolating Ring : E=20000, v=0.49, disp=2mm, angle=90 deg, Wide Ring, Cross Sectional View at x=0
Figure 6-1 Signal Processing Flow Chart
Figure 6-2 Periodic Source with 1 Hz Frequency s[n]
Figure 6-3 Random Noise d[n]
Figure 6-4 Combined Signal x[n]
Figure 6-5 Autocorrelation function of x[n]
Figure 6-6 Second autocorrelation function of x[n]
Figure 6-7 Experiment Setup
Figure 6-8 Original ring sensor signal and the result after autocorrelation
Figure 6-9 Autocorrelation function showing the second peak of the heartbeat
Figure 7-1 Isolating ring sensor designed for motion artifact minimization
Figure 7-2 Comparison of Power Budget
Figure 8-1 First Prototype Ring Sensor
Figure 8-2 Ring Sensor with One or Two Circuit Boards
Figure 8-3 Wire Bonding Machine
Figure 8-4 Dimensions of Components
Figure 8-5 Pictures of the miniaturized circuit boards
Figure 8-6 Miniaturized ring sensors
Figure 9-1 Signal contaminated by motion artifact
Figure 9-2 Signal contaminated by ambient light influence.
Figure 9-3 Experiment of pulsation amplitude and skin contact pressure
Figure 9-4 Experiment of tension-strain characteristics of inner ring band
Figure 9-5 Static force experiment
Figure 9-6 Comparison between the ring sensor of the single body design and the isolating ring sensor under external static force.
Figure 9-7 Comparison between the ring sensor of the single body design and the isolating ring sensor under acceleration.
Figure 9-8 No external static force with contact pressure of 75 mmHg.
Figure 9-9 Static force experiment with 75 mmHg contact pressure.
Figure 9-10 Static force experiment with 11 mmHg contact pressure.
Figure 9-11 Heart rate monitored by EKG, Fingertip PPG device, ring sensor
Figure 9-12 A part of the two-hour monitoring test result
Figure 9-13 Guidelines for the design of the ring sensor.

Table 9-1 RMS error (beats/min) of the heart rates from the ring sensor compared with those from the EKG and fingertip PPG device

1. INTRODUCTION

1.1 Background and Objectives

Ambulatory patient care makes up the bulk of medical care and affords the best opportunity for preventive medicine. The renaissance of interest in ambulatory care in general, and for the hi-risk cardiac patient in particular, is gaining ever-increasing momentum. With the aid of modern technology and a better understanding of physiological processes, medical care is experiencing a rapid evolution in both diagnostics and therapeutics. This technical progress now provides the potential for improved care of the patient in the ambulatory environment. From the administrative and economic aspects, moving the focus of care from the hospital to the ambulatory environment can bring about considerable economic benefits. From the patients' viewpoint, they can avoid being confined in the hospital environment solely to guard against any future outbreak, but still protected from those possibilities by online observation [1].

Vital sign monitoring is becoming increasingly important for securing independent lives as the population of aged people increases. Online, continuous monitoring allows us to detect emergencies and abrupt changes in the patient's condition. Especially for cardiac patients, online, long-term monitoring plays a pivotal role. It provides critical information for long-term assessment and preventive diagnosis for which long-term trends and signal patterns are of special importance. Such trends and patterns can hardly be identified by traditional examinations. Those cardiac problems that occur frequently during normal daily activities may disappear the moment the patient is hospitalized, causing diagnostic difficulties and consequently possible therapeutic errors. In this sense, continuous and ambulatory monitoring systems are needed to detect the traits.

Although there have been many ambulatory monitoring systems developed and discussed, none of them have reached the level that can fully cover the patients' everyday lives, mostly due to the fact that those devices are bulky and inconvenient to carry. When taking a shower, for example, people tend to remove any ambulatory monitoring devices. Bathrooms, however, are one of the most dangerous places in the home. More than 10,000 people, mostly hypertensives and the elderly, die in bathrooms every year. Therefore, it is important that the ambulatory monitoring devices should be easy to wear in everyday life. Such long-term, ambulatory devices must be compact, lightweight,

and comfortable to wear at all times. They must be designed for low power consumption for long term use. Furthermore, they must be able to detect signals reliably and stably in the face of motion artifact and various disturbances. Unlike traditional monitoring systems, these devices are used under no supervision of clinicians. Data is collected from the daily lives of patients in an unstructured environment.

The goal of this thesis is to develop the technology for obtaining reliable measurements of vital signs for long-term use. A miniaturized photoplethysmograph (PPG) device in a ring configuration will be designed and tested, which will be used for continuously measuring valuable information such as heart rate. It will be shown that the device meets diverse and conflicting requirements, including compactness, motion artifact reduction, minimum loading effects, and low battery power consumption. Mathematical modeling of the finger under external forces will help understand the underlying principle of vital sign monitoring by the ring sensor. Its benchmarking tests with the FDA approved PPG and EKG will show the validity of the technology.

1.2 Prior Work in the Field

The ambulatory ECG (Holter) device, one of the most widely accepted ambulatory monitoring systems, was developed and extensively studied by N.J. Holter [2]. Bellet also devised a continuous 2-hour tape recording system using a similar device [3]. When the ambulatory ECG device was first introduced, the device was not immediately widespread due to concerns over the lack of previous documentation of coronary artery disease, the device's reliance upon T-wave changes, and the lack of recorder fidelity [1]. After many improvements and validity tests, the ambulatory ECG technology has gained increasing popularity. The ambulatory ECG, however, is not applicable to long-term monitoring for a period of several weeks or months. The machine is bulky, heavy, and uncomfortable to wear due to cumbersome wires and patches. Recently, a variety of vital sign sensors have been developed that are compact and easy to wear. Yamashita, *et al.* [4] attempted to develop a simple telemetry device for monitoring the pulse at a finger. Wristwatch-type pulse oximetry and blood pressure sensors have been developed and commercialized by several companies including Casio (BP-100 and JP200W-1V) and Omron (HEM-608 and HEM-609).

These devices, although much easier to wear, have not yet been used clinically. Many technical issues still need to be solved prior to clinical use. In general, long-term, ambulatory monitoring

systems have not yet reached a technical level that is widely accepted by both clinicians and patients. These devices are still unsatisfactory in size, and cannot provide long-term use due to a lack of battery power. In addition, since the collected data is either erased or recorded in restricted memory space included in the devices, creating a patient history over a long period of time is practically impossible. For long-term use, power consumption should be minimized and a method of archiving the obtained data developed. For example, if the data can be continuously transferred wirelessly elsewhere and stored someplace other than the ambulatory monitoring device itself, its size can be further reduced and its weight become light.

As for the effect of motion artifact on ambulatory monitoring devices, there have been many attempts to analyze and reduce the influence of motion on the monitored signals. Many researchers have attempted to quantify the movement artifact in pulse and oxygen saturation measurements [5][6], and some researchers have used advanced filtering techniques such as an adaptive noise canceler to reduce the impact of motion [7]. In terms of the modeling of photoplethysmography, Higgins, J. L. and Fronek, A. derived a mathematical formulation of reflectance photoplethysmography to evaluate the relationship between skin reflectance and skin blood flow [8]. Their model was based on the modeling of cutaneous blood flow. Yamakoshi [9][10] and Wesseling [11] have conducted numerous experiments about finger photoplethysmography, mainly focusing on the cuff-based pressure measurement technique.

Although there exist many experimental results and mathematical models that can help understand the principles of finger photoplethysmography, they cannot be directly applied to the case of the ring sensor since they have mostly focused on the response of finger photoplethysmography under uniform pressure applied around the finger. In case of the ring sensor, "local pressure" is applied to the finger as the ring moves. Therefore, to deal with the movement of the ring sensor, we need a new mathematical model that can explain the photoplethysmography when the finger is under non-uniformly distributed pressure.

1.3 Outline of Thesis

This thesis will discuss the design and analysis of the ring sensor. The issues involved in the design of the ring sensor, including motion artifact minimization, power consumption minimization, and loading effect problems, will be dealt with both theoretically and experimentally. To assess the

conditions that contribute to the variations of the signal in the presence of mechanical disturbances, a mathematical model of finger photoplethysmography that can explain the variations under external forces will be developed and discussed in detail. Many other practical issues involved in prototyping and signal processing will be depicted.

In chapter 2, the ring sensor concept is introduced and the issues involved are presented. These issues will be further discussed in the later chapters. Chapter 3 is dedicated to an in-depth discussion of one of the major issues: motion artifact. A unique design called the "Isolating ring sensor design" will be presented and its advantages will be discussed. Methods for detecting the signals contaminated by artifacts will be also presented in this chapter. In chapter 4, the issue of power consumption minimization is presented. The basic circuitry of the ring sensor is explained. A mathematical analysis of power consumption is addressed and its minimization process is described. In chapter 5, a theoretical analysis of the response of the finger photoplethysmography under external force is thoroughly discussed. A new mathematical model that includes an optical model, a tissue mechanics model, and a blood vessel model is developed. Using this model, a variation of the finger photoplethysmography with external pressure applied to the ring will be analyzed and predicted. In particular, this model will be able to deal with the effect of local pressure on the finger. Eventually, this model will be used to assess the conditions that can make the ring sensor less sensitive to mechanical disturbances. This mathematical model will be verified by numerical simulations and experiment results. Chapter 6 will discuss signal processing techniques used for extracting the pulse wave from distorted photoplethysmographic signals. A crosscorrelation method will be used to obtain the periodic pulse signal from the noise-dominating signal. Its effectiveness will be discussed in terms of numerical simulations and an analysis of the experiment results. In chapter 7, the prototyping of the ring sensor will be described in detail. The packaging of the device and the selection of electronic components, considering size and power consumption, will be discussed. The actual derivation of the optimal clock frequency of the CPU for power consumption minimization will be given, and the design of the software including the PC monitoring program and the micro code for the ring sensor CPU, will be introduced. In chapter 8, practical issues concerning the miniaturization of the whole circuitry to the size of a real finger ring will be presented. The usage of die form chips, the wire bonding technique and miniature components will be discussed. In chapter 9, extensive experiment results will be presented and analyzed. The ring sensor will be benchmarked to other monitoring devices such as the EKG and FDA-approved

fingertip photoplethysmographic sensors. In addition, the effectiveness of the isolating ring design will be verified by experiments.

2. THE RING SENSOR

2.1 Basic Description of the Ring Sensor

The ring sensor is a miniaturized, telemetric, monitoring device worn by a patient as a finger ring. The ring encapsulates photoplethysmographic, pulse oximetry combined with wireless communication and miniaturization technologies. This device optically captures the pulsation and oxygen saturation of the arterial blood flow, and transmits the signals to a host computer via an RF transmitter. Figure 2-1 shows a conceptual diagram of the ring sensor [12][13]. The ring sensor consists of optoelectronic components, a CPU, an RF transmitter, a battery, and a ring chassis. The optoelectronic components, i.e. micro photodiodes and LEDs, detect the blood volume waveforms and oxygen saturation level in the patient's digital artery. The CPU controls the LED lighting sequence as well as the data acquisition and transmission process. These signals are locally processed by the on-board CPU and transmitted to a host computer for diagnosis of the patient's cardiovascular conditions. The ring sensor is completely wireless and miniaturized so that the patient can wear the device comfortably twenty-four hours a day.

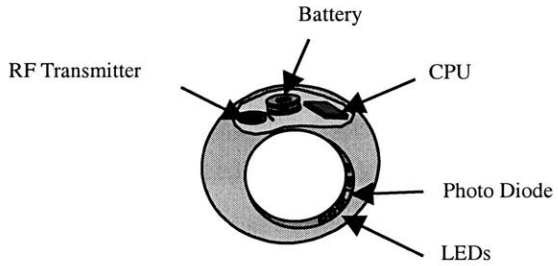

Figure 2-1 Conceptual diagram of the ring sensor

For continuous patient monitoring, the device must be compact, easy to wear, non-intrusive, and non-invasive. It also must be equipped with wireless communication technology since the data must be transferred to base stations without physical wiring. The miniaturized sensor in a ring configuration is a rational design choice for twenty-four hour continuous monitoring, since a finger ring is probably the only thing that a majority of people will be willing to wear at all times. Other personal ornaments and portable instruments, such as earrings and wristwatches, are not continually worn in daily living. Miniature ring sensors provide a promising approach to monitoring a patient at all times. Also, a ring configuration provides the anatomical advantage of being able to use the

transparent skin and tissue at the finger, so that it becomes feasible to monitor arterial blood volume at the finger base using an optoelectronic sensor. Subsequently, a variety of simple cardiac and circulatory disorders may be detected by monitoring arterial blood volume at the finger base.

2.2 Issues

The ring sensor, however, is inevitably susceptive to a variety of disturbances such as a patient's motion and ambient lighting. When the patient moves, the inertia force created at his/her finger causes the ring to move relative to the skin surface and, as a result, measurement may be distorted or even ruined completely. When the ring touches an environment surface, the contact force may cause a distortion of the measurement due to the relative displacement of the sensor to the finger. In addition, ambient lighting is another major source of artifact for optical measurement. These kinds of disturbances degrade the quality of measurement and can make the ring sensor an unreliable device.

Another important issue with this type of wearable sensor is the possible necrosis of finger tissues, or ulcers caused by local ischemia. To attain stable photoplethysmograph signals, it is necessary to apply a certain magnitude of pressure to the skin surface. Such pressure application is nothing harmful for short-term monitoring, but would be a problem for long-term use. With a constant, prolonged pressure at the finger base, the arteriovenous and cutaneous circulation in the finger can be obstructed, and possibly result in subsequent tissue sphacelation. Numerous studies have dealt with the effect of ischemia on tissue and other types of pressure sores, and a few have addressed the critical pressure and duration problem [14][15][16]. These have found that an inverse relationship exists between the critical pressure and duration. Some have also investigated ischemic hyperemia on the finger, which may eventually result in tissue injury [17]. In the case of the finger, blocking the venous return will cause serious problems even at a relatively low pressure since the circulation will be obstructed by the pressure. Therefore, the ring sensor should be designed for minimum circular obstruction by keeping the tissue pressure at a low level.

In addition, the whole electronic circuit must be designed for minimum power consumption in order to operate it for a long time without changing or recharging the battery. Among others, LED is one of the most power-consuming parts involved in the ring sensor. Therefore, the intensity of the LEDs must be lowered, along with a reduction of the duty cycle. This, however, incurs a poor signal-to-

noise ratio problem. The signals obtained with dark LEDs are weak and must therefore be amplified many thousand times. As a result, it becomes susceptive to any disturbance.

There are a number of existing techniques for dealing with artifact and disturbance rejection. The most common is signal processing, as reviewed by [18]. Another standard method is to identify and reject corrupt signals by comparing pulse features with a predetermined template. Other methods use modulation by controlling the power level of multiple lighting sources [18]. All of these methods, however, involve the modification and conditioning of received signals, and do not eliminate or reduce the influence of the sources of the artifact. The artifact problem of the ring sensor is primarily due to the difficulties of attaching the sensor to the skin. This source of artifact must be removed before applying those signal processing methods.

In the following sections, a new design having a double ring configuration will be developed in order to minimize the influence of both mechanical and optical disturbances, while avoiding excessive pressure on the finger.

3. ARTIFACT-RESISTANT DESIGN

3.1 Isolating Ring Architecture

Figure 3-1(a) shows the cross-sectional view of the original ring sensor where the optoelectronic sensor unit, i.e. the LEDs and photodiodes, is attached directly to the body of the ring. (previously developed by the authors [12][13]) The problems with this design are:

- When the ring touches the environment surface, the ring is pushed to one side, creating an air gap between the sensor unit and the skin, or increasing the pressure with which the sensor unit is attached. This causes significant fluctuation in the sensor reading.
- The body of the ring sensor, including the battery and circuitry, tends to be heavy. A small acceleration of the finger and even gravity affecting the ring itself may cause a displacement relative to the skin surface. Securing the ring body requires a large force applied to the finger skin.
- It is difficult to shield the sensor unit from ambient lighting.

To resolve these problems of the original ring design, a new design is presented in this section. The new design, called an "isolating ring configuration," is illustrated in Figure 3-2. The main idea of this design is to separate the sensor unit from the rest of the ring body, which is much heavier than the optical sensor unit alone. The separation is achieved by having two rings that are mechanically decoupled to each other. The inner ring shown in the figure holds the sensor unit alone, while the outer ring contains the CPU, signal processing unit, battery, and RF transmitter. Only a thin, flexible cable assembly connects the two rings. This decoupled design has the following advantages.

Alleviating the influence of external forces applied to the ring

Forces due to mechanical contacts are borne by the outer ring, and are not directly transmitted to the sensor unit on the inner ring. As shown in Figure 3-1(b), the load of the external force is bypassed

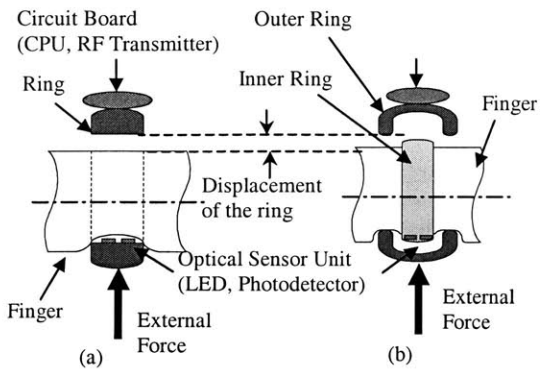

Figure 3-1 Dislocation of ring sensors due to external load
(a) Traditional single body design under external force
(b) New isolating ring sensor under external force

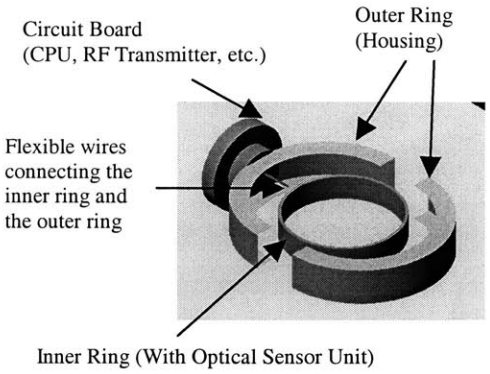

Figure 3-2 Construction of isolating ring

to the finger bone and is supported by the two feet of the bridge-like outer ring. Thereby the force does not directly influence the actual sensor unit attached to the inner ring.

Alleviating the effect of acceleration on the sensor

The inertia of the sensor unit is very small since it contains only a few LEDs and photodiodes. Due to the small inertia of the inner ring, the inertia force acting on the sensor unit is negligibly small. In consequence, the position of the optical sensor does not change significantly when the finger is accelerated.

Reducing skin contact pressure

The outer ring doesn't have to be secured tightly, while the inner ring doesn't need a great pressure to secure it to the body, since it is light. Therefore, the possibility of necrosis caused by local ischemia and occlusion is lowered. This solves a critical problem of wearable sensors and long-term monitoring systems such as the ring sensor.

Reducing the influence of ambient lighting

The outer ring shields the sensor unit and thereby reduces optical disturbances from ambient lighting. The isolating ring structure provides the sensor unit with an optical shield.

Thus the isolating ring structure alleviates those critical problems of the original single-body ring sensor.

3.2 Movement Detection by Software

Transmitted photoplethysmograms are received and analyzed by a home computer. Although the signal is already filtered and refined by the analog signal conditioner in the ring sensor, it still contains high frequency noise due to ambient light sources and motion artifacts. For example, Figure 3-3(a) shows a steady photoplethysmogram with no artifact, whereas Figures 3-3(b) and 3-3(c) show the signal contaminated by the influence of ambient light and motion artifact,

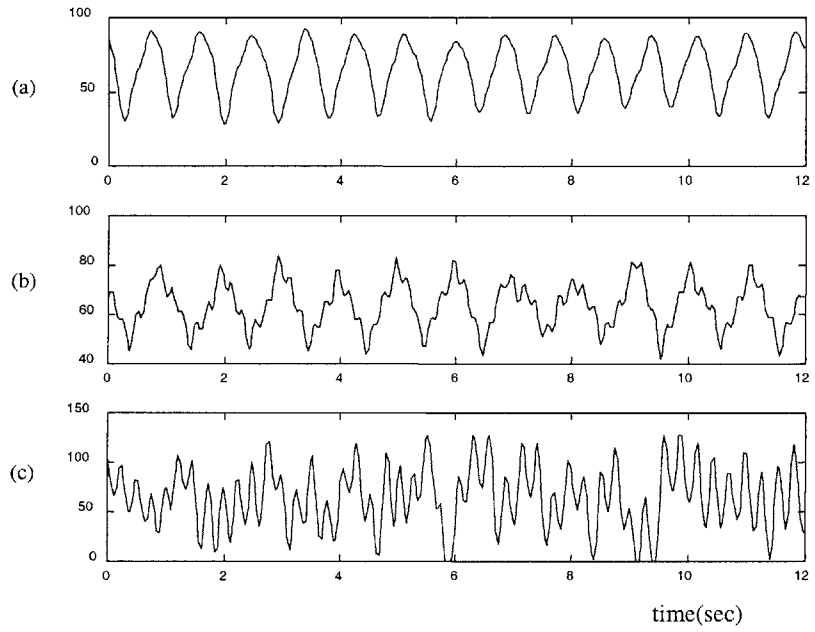

Figure 3-3 Various Signals Detected by the Ring

respectively. It is clearly seen that the contaminated signal carries high frequency noise even though it has already passed through a hardware lowpass filter. When the host computer detects high-frequency noise, the computer does not display the waveforms on the screen.

3.3 Movement Detection using Accelerometer

When the finger moves dynamically, the signal from the ring sensor is drastically distorted and even saturated. In this case, it is almost impossible to recover the original plethysmographic signal.

Therefore, it is better to ignore the monitored signal under heavy motion. Although it is possible to detect the motion to some extent with simple signal processing techniques, software-based motion artifact detection is rather indirect and less accurate. Since most of the motion can be effectively detected with an accelerometer, using a MEMS accelerometer is a good method. Figure 3-4 shows a diagram of the algorithm. Since the monitored signal is just ignored when the ring sensor is moving, it can effectively reject any signal contaminated with artifact from dynamics motion.

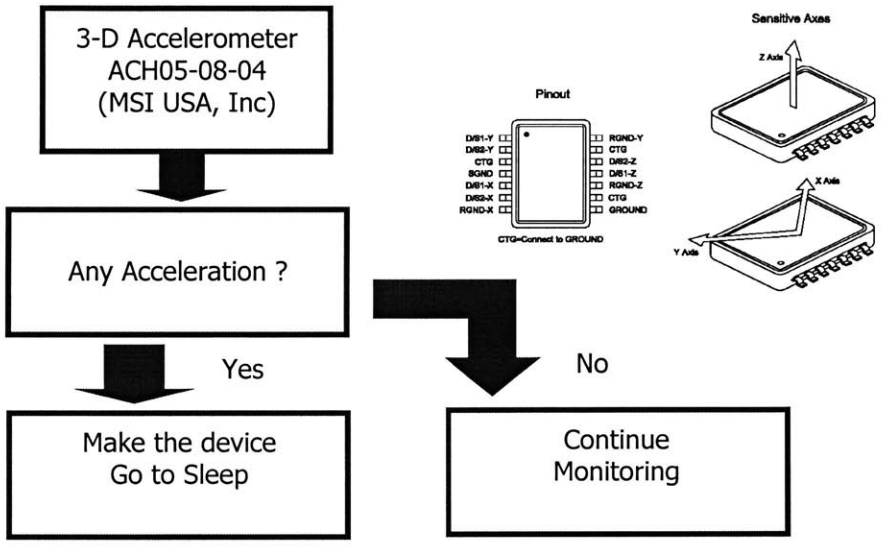

Figure 3-4 Detection of movement by 3-D accelerometer

4. POWER SAVING ELECTRONICS DESIGN

4.1 Description of the Basic Circuitry

Since the device has to be worn for a long time without an external power supply, it is critical to minimize power use as much as possible. The whole circuit must be designed with a consideration of maximum power saving. Figure 4-1 shows a block diagram of the ring sensor circuitry. The basic circuit configuration is a standard photoplethysmographic circuit combined with a wireless transmitter. There are LEDs of two different wavelengths, red and near infrared, and a single photodiode involved in the circuit. The output from the photodiode is amplified and conditioned at the first stage operational amplifier. While the red and infrared LEDs are alternately turned on and off, the signal from the first stage op-amp is sampled by the two sample-and-hold circuits at different timings in order to obtain the reflected light intensity from each LED. Each channel of the signal is conditioned and converted to a digital signal with an AD converter. Using the standard RS-232 protocol, the two channels of digital signals are transmitted via an RF transmitter.

This circuit is a standard one, but the whole system is designed and operated for low-power consumption. Since the battery cell is the dominant factor determining the dimension and weight of the device, large batteries cannot be used for the ring sensor; hence the reduction of power consumption is critically important for miniaturizing the sensor. Each component has to be selected for low-power consumption, and the whole system must operate with a minimum of power consumption. The microprocessor coordinates the whole operation so that reliable measurements

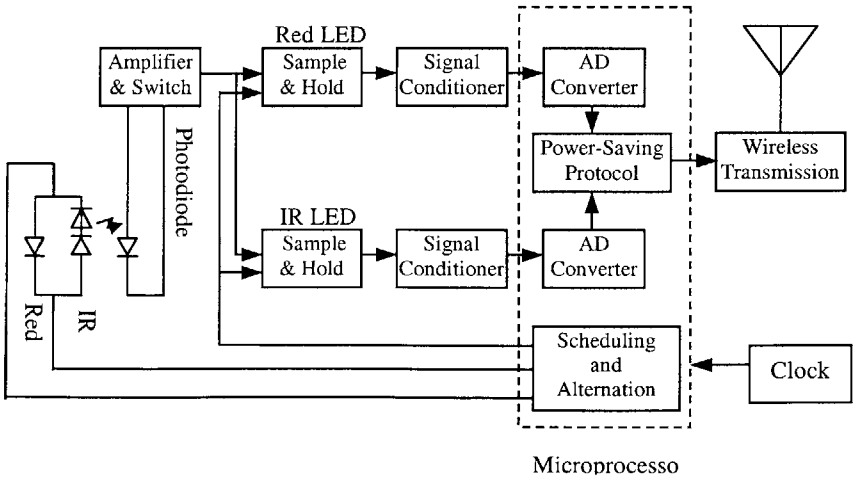

Figure 4-1 Block diagram of electronic circuit

are taken with minimum power. The total power consumption depends both on the individual component characteristics and on the way that the components are controlled and operated. In the following section, a power consumption model will be derived in order to obtain guidelines for selecting components as well as for operating the system.

4.2 Power Budget

Among the many components involved in the ring sensor, the LEDs and the RF transmitter consume over 70% of the total power; hence a saving in the power consumption of these components contributes significantly to the overall power saving. The objectives of this section are to provide a detailed power budget of the ring sensor, and to present an approach to minimize the power consumption pf the LEDs and the RF transmitter while satisfying the specifications of the ring sensor. The power budget may differ depending on the specific algorithms and control schemes needed to operate the LEDs and RF transmitter. In the following, a power budget will be obtained for a specific control algorithm that is simple and feasible for implementing on a miniaturized ring sensor. For different algorithms, a power budget can be obtained without difficulty in the same way as the following formulation.

LED

LEDs consume a large amount of power when emitting light continuously. Therefore they must be switched on only for the short interval when light must be emitted. Namely, the LEDs must be on only when the photodiode is detecting the reflected light that measures the pulsation. Synchronizing the sampling of the photodetector with the LED switching reduces the duty ratio of the LEDs, and thereby reduces the power consumption. In the prototype system, this coordination is performed by the microprocessor. First the LEDs are turned on, second the photo detector signal is sampled at the next CPU cycle, and the LEDs are switched off at the third CPU cycle. This sequence control is performed for both red and infrared LEDs. As the CPU clock cycle increases, the duty ratio of the LEDs decreases, and hence the power consumption decreases. However, the CPU consumes more power as the clock frequency increases. Therefore, a trade-off must be made between the CPU power and the LED power in order to minimize the overall power consumption.

Key parameters associated with the LEDs' power consumption are:

q : internal clock frequency of the microprocessor (Hz)

f : sample-and-hold frequency (Hz)

r : duty ratio of LEDs

C_r : total power consumption of the red LED circuit per second

C_i : total power consumption of the infrared LED circuit per second

In the above lighting sequence, both red and infrared LEDs are turned on for three internal CPU clock cycles, that is, $3 / q$ seconds. Therefore the duty ratio of the LEDs is $r = 3f / q$. The average power consumption of the LEDs is given by

$$P_l(q) = r(C_r + C_i) = \frac{3f(C_r + C_i)}{q} \tag{4-1}$$

Microprocessor

In general, the power consumption of a microprocessor increases with the clock speed. In the prototype ring sensor, a linear relationship exists between the power consumption and clock speed q:

$$P_m(q) = aq + b \tag{4-2}$$

where the coefficients a and b can empirically be determined.

RF Transmitter

The sampled analog signals are converted to digital signals by an A/D converter and transmitted through the RF transmitter controlled by the same microprocessor. The transmission protocol is the standard RS-232 using simple on-off keying. The most power-consuming part of the digital RF transmitter is an oscillatory circuit involving a CMOS power transistor, which consumes a significant amount of power only when the output is high, i.e. 1-bit. In other words, the power consumption is virtually zero when the output is low, i.e. 0-bit. Therefore, power can be saved by reducing the pulse width of each 1-bit. In the standard RS-232 protocol, the width can be reduced

simply by increasing the baud rate. As the baud rate increases, transmission is completed in a shorter period of time, leaving a longer time for the transmitter to be in an idle state with no power consumption. However, a higher baud rate of the transmitter requires a higher clock frequency for the microprocessor, which results in larger power consumption. Similar to the previous case, a trade-off must be made between the CPU power and the transmitter power. We now formulate the power budget of the transmission circuit and optimize the power consumption in terms of the clock frequency.

Key parameters associated with RF transmission are:

d : baud rate of transmission (bps)

n : number of sample points to be transmitted per second (Hz)

m : average number of high bits to be transmitted per second (bps)

C_t : total power consumption of the transmission circuit per second

Transmission of one bit needs at least 6 CPU instructions, including branching, port setting, carrier setting, and bit-shifting instructions. Therefore it takes 6 internal CPU clock cycles. Namely, the fastest baud rate that can be achieved for a given clock frequency is $d = q / 6$. In the prototype ring sensor, the resolution of the A/D converter is 8 bits; hence one sample point is one byte of data. Including the start bit and the stop bit, the standard RS-232 protocol needs five high bits to transmit on average per sample point (one byte), resulting in $m = 5n$. Therefore, the average duty ratio of the RF transmitter transmitting a high bit is $m / d = 30n / q$. The average power consumption due to RF transmission is therefore given by

$$P_t(q) = \frac{30nC_t}{q} \tag{4-3}$$

The total average power consumption of the LEDs, RF transmitter, and microprocessor is

$$P_T(q) = P_l(q) + P_t(q) + P_m(q) = \frac{3f(C_r + C_i)}{q} + \frac{30nC_t}{q} + aq + b \tag{4-4}$$

The optimal internal clock frequency q^* can be obtained by differentiating the above equation and equating it to zero:

$$\frac{dP_T}{dq} = -\frac{3f(C_r + C_i) + 30nC_t}{q^2} + a = 0 \tag{4-5}$$

Namely,

$$q^* = \sqrt{\frac{3f(C_r + C_i) + 30nC_t}{a}} \tag{4-6}$$

5. THEORETICAL ANALYSIS OF FINGER PHOTOPLETHYSMOGRAPHY WITH RING SENSOR

5.1 Background

Real-time, continuous monitoring with the ring sensor allows not only for emergency detection but also for long-term monitoring of otherwise difficult and noncompliant patients such as demented elderly people. However, as a wearable ambulatory sensor, the ring sensor is inevitably subject to measurement noise due to the everyday activities of a patient. In particular, the relative displacement and the rotation of the sensor probe on the finger is a major cause of loss of accuracy, and a common problem for all other photoplethysmographic sensors such as pulse oximeters. The objective of this chapter is to quantify the mechanism of the motion artifact of finger photoplethysmography based on an opto-physiological model of the finger and to facilitate a development of the ring sensor which is less affected by the relative displacement of the finger to the ring.

There have been many attempts to analyze the influence of mechanical interference on the photoplethysmography. Although the experiments and models from those studies help in understanding the principles of finger photoplethysmography, they cannot be directly applied to the case of the ring sensor since they were mostly focused on the analysis of finger photoplethysmography under uniform pressure applied around the finger. In case of the ring sensor, "local pressure" is applied to the finger as the ring moves. Therefore, to deal with the movement of the ring sensor, we need a mathematical model that can explain the photoplethysmography when the finger is under non-uniformly distributed pressure.

In this chapter, we first examine and categorize a variety of movements that influence the photoplethysmographic signals of the ring sensor. To articulate and analyze the influence of each movement, we build a mathematical model of the finger photoplethysmography. The main feature of the model is the integration of multiple domains such as the ring mechanics, finger tissue kinematics, digital arterial wall dynamics and biomechanical optics. In particular, the nonlinear behavior of the arterial wall in response to external pressure, which is the basis of the oscillometric method of blood pressure measurement, is intensively addressed. Also, the optical property of the finger tissue is discussed. The resultant opto-physiological model of the finger and the ring sensor

allows for a simulation of the influence of mechanical displacement of the finger on photoplethysmographic signals. The finite element method is used to verify the tissue model; extensive simulation is conducted and the numerical results are compared with the experimental data for the validation of the model. With this model, the advantage of the isolating ring sensor design is validated with the finite element method.

5.2 Approach

One of the most important issues of wearable sensors is the reduction of noise caused by motion artifacts. Many kinds of motion artifacts, such as fast and vivid motion of the finger, static relative displacement, and rotation of the ring relative to the finger, can interfere with the measurements of the ring sensor. However, since the ring sensor is mainly to be worn by elderly patients and potential patients of cardiovascular disorders, it is reasonable to assume that, of these three things, the static displacement and/or rotation of the ring will predominate over fast movements with large accelerations. For example, if any external static force is applied to the ring so that the center point of the ring deviates from that of the finger, the photoplethysmographic signal will change. The rotation of the ring around the finger will also cause a change in the signal. A mathematical model of the finger and the ring will be very useful in understanding and analyzing the variations of the photoplethysmographic signal due to the displacement and the rotation of the ring. This model has to integrate all of the optical, mechanical and physiological properties of the ring sensor. In other words, the optics of the finger tissue and blood, finger tissue kinematics, geometry of the ring, and dynamics of the arteries and the capillaries must all be incorporated into one model to describe the photoplethysmographic behavior. In particular, the dynamics of the arterial wall should be modeled carefully since the compliance of the arterial wall exhibits nonlinear behavior [11]. The modeling of the optical properties is another point that has to be dealt with very carefully.

Figure 5-1 shows a cross-sectional view of the finger. The cross section of a finger is assumed to be a circle when there are no external forces. Although there are four digital arteries in the finger, we only describe two proper palmar digital arteries in this model since dorsal digital arteries are located far away from the optical sensor. These two proper palmar digital arteries are both positioned at a distance h_0 away from the center of the finger. The tissue is considered as a compliant material with stiffness k_t. To alleviate the sensitivity of the photoplethysmographic signal variation due to

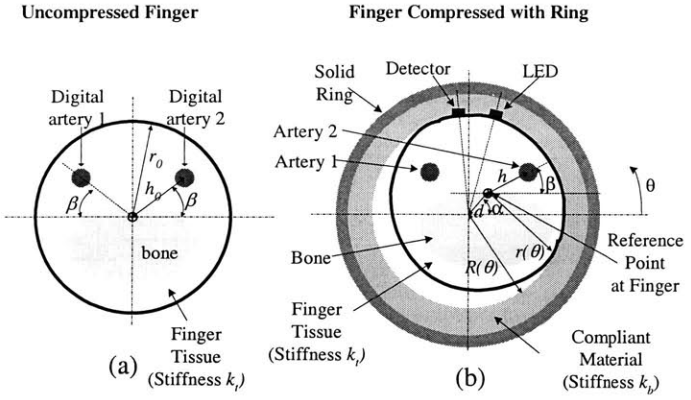

Figure 5-1 (a) Uncompressed finger under no external force (d=0). (b) Finger compressed by the ring due to an external force.(d>0)

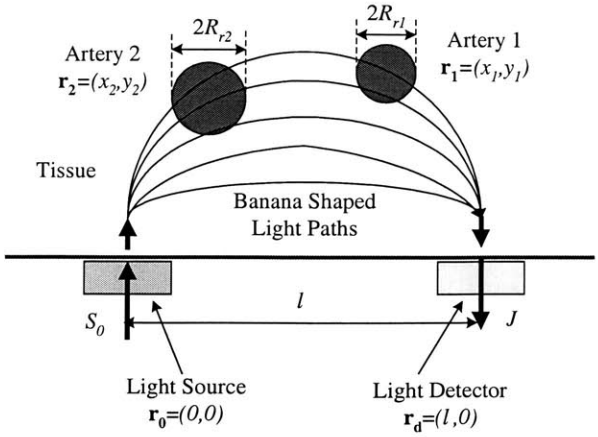

Figure 5-2 Optical model of the finger and optical elements. Blood vessels have different optical properties from the tissue.

movement of the finger, a compliant material of stiffness k_b is attached inside the solid ring. A light source (LED) and a photodetector are located on the compliant material inside the solid ring. When any external force is applied to the ring, it moves in a certain direction at an angle α by a certain relative displacement d. Because of this movement, the pressure at the contact point increases and the relative locations of the digital arteries to the optical elements (the LED and photodetector) change, which leads to a variation in the photoplethysmographic signal. At the same time, a deformation of the finger surface occurs and the cross section of the finger is no longer a circle. Due to this deformation of the tissue, the pressure applied to each of the two digital arteries also changes, which results in a change in the volumetric pulsation of the blood vessel. In addition, the volume of the capillaries in the finger cross section also changes due to the change in pressure. The capillaries occlude more easily than the digital arteries since the internal pressure of a capillary is much lower than that of the arteries. In this research, it will be assumed that the tissue consists of two uniformly distributed materials, whole blood and the blood-free tissue, although it is realized that in most tissues the red blood cells are inhomogeneously distributed to some extent [19]. Under this assumption, the tissue's absorption and scattering coefficients can be determined by combinations of the absorption and scattering coefficients of the whole blood and the blood-free tissue depending on the volume fraction of the blood in the tissue. In this context, the average value of the absorption coefficient of human tissue decreases as the blood is squeezed out of the tissue since the absorption coefficient of blood is much higher than that of blood-free tissue. At systole, the volume fraction of the blood in tissue becomes the maximum, while it falls to the minimum at diastole. Meanwhile, the overall volume fraction of blood in the capillaries decreases in the tissue as the external pressure

around the finger increases, resulting in the decrease of the overall absorption coefficient of the tissue. Thus, the occlusion of capillaries is represented as the overall decrease of absorption and scattering coefficients of the tissue. The pulsating signal of photoplethysmograph is caused by the volumetric change of the digital arteries and capillaries due to the change in the blood pressure.

5.3 Modeling

5.3.1 Optical Model

The light emitted from the LED passes into the tissue and the number of the paths of photons is almost infinite, which makes it difficult to obtain a good optical model. The light absorption, multiple scattering, and diffusion processes all occur at the same time. It is known that the average photon migration path in the tissue is a banana shape [20]. Assuming that the tissue is optically homogeneous, the cross section of a finger can be divided into four regions : two digital arteries, capillaries, veins, and all other regions (We will generically call these regions "blood-free tissue"). The blood that flows in the arteries has different optical properties from that which is in the tissue. Looking at the cross section of the finger, it is possible to consider the digital arteries as two circular regions with different optical properties from the surrounding material. Using the analogy with electrostatics, the photon flux density at the detector can be expressed as a function of the positions of the two arteries, the radii of the arteries, the position of the photodetector, and the optical properties of the tissue and the blood. Feng, S., Zeng, F., and Chance, B. derived an analytical formulation of the photon path distributions in the presence of a spherical region with different absorption and scattering properties from the surroundings in semi-infinite geometry [20]. Figure 5-2 shows the geometry of the light source, the photodetector, the arteries and the capillary layer. The light source is in the steady-state condition (constant source intensity of light S_0) and is located at the origin $\mathbf{r_0}=(0,0)$ of the x-y coordinates. The photon flux density at the detector which is located at $\mathbf{r_d}=(l,0)$ is denoted as J. Although the LED and the photodetector are placed along a circular ring surface, it is assumed that they are located on a straight line $y=0$. This assumption is valid as long as l is much smaller than the internal perimeter of the ring. The pulsation of capillaries is counted by the dynamic change of the optical properties of the tissue surrounding the arteries. Under the assumption that the capillaries are uniformly distributed in the tissue, these optical properties are

determined by the fraction of whole blood in the tissue. Since both the absorption and scattering coefficients of blood are larger than those of blood-free tissue, the combined optical coefficients generally increase at systole, resulting in a decrease of the photon flux density at the photodetector. The blood in the vein also contributes to the variation of the optical coefficients of the tissue. However, it only influences the DC part of the variation since the AC part of the venous pulsation is much smaller than that of the arteries and capillaries. From this insight, the effect of venous blood is included as a DC-level modulation factor of the optical constants of the tissue, and the effect of the volumetric concentration of the veins similar to the arteries is neglected in this model. Consequently, the overall optical constants of the tissue must be determined based on the fractions of blood-free tissue, blood in the capillaries, and blood in the veins.

In an analogy with electrostatics, the arteries are similar to the dielectric material in the electrical field. Noting the presence of two digital arteries which are located at $\mathbf{r_1}=(x_1, y_1)$ and $\mathbf{r_2}=(x_2, y_2)$ with radii of R_{r1} and R_{r2} respectively, the relationship between the light intensity S_0 and the photon flux density J at the detector is described as follows.

$$J = \frac{y_0 S_0}{2\pi}\left(\frac{\kappa}{l^2}+\frac{1}{l^3}\right)\exp(-\kappa l) + J_1(\mathbf{r}_1, R_{r1}) + J_1(\mathbf{r}_2, R_{r2}) \tag{5-1}$$

where the function $J_1(\mathbf{r},R)$ is as follows.

$$\begin{aligned} J_1(\mathbf{r}, R) = {} & 2Dq(R)\frac{(\kappa|\mathbf{f}|+1)y}{|\mathbf{f}|^3}\exp(-\kappa|\mathbf{f}|)\Phi_0(\mathbf{r}) \\ & - 2Dq(R)\left\{\frac{[\mathbf{f}\cdot\mathbf{E_0}(\mathbf{r})](\kappa|\mathbf{f}|+3)y}{|\mathbf{f}|^5} - \frac{{E_0}^y(\mathbf{r})}{|\mathbf{f}|^3}\right\}\exp(-\kappa|\mathbf{f}|) \end{aligned} \tag{5-2}$$

where

$$\mathbf{r} = (x, y), \quad \mathbf{f} = \mathbf{r} - \mathbf{r_d} \tag{5-3}$$

$$\Phi_0(\mathbf{r}) = \frac{y_0 y S_0'}{2\pi D}\frac{(\kappa|\mathbf{r}|+1)}{|\mathbf{r}|^3}\exp(-\kappa\mathbf{r}) \tag{5-4}$$

where $y_0 = 0.7/\mu_s'$,

$$\mathbf{E}_0(\mathbf{r}) = \left(E_0{}^x, E_0{}^y\right)$$
$$= \frac{y_0 S_0}{2\pi D}\left(\frac{3\kappa y\mathbf{r}}{|\mathbf{r}|^4} + \frac{3y\mathbf{r}}{|\mathbf{r}|^5} - \frac{\kappa\hat{y}}{|\mathbf{r}|^2} - \frac{\hat{y}}{|\mathbf{r}|^3} + \frac{\kappa^2 y\mathbf{r}}{|\mathbf{r}|^3}\right)\exp\left(-\kappa|\mathbf{r}|\right) \tag{5-5}$$

$$q(R) = -R\exp(\kappa R)\left\{\frac{\tilde{D}B(1-\mu_a/\tilde{\mu}_a)}{D(1+\kappa R)\sinh(\tilde{\kappa}R)/(\tilde{\kappa}R) + \tilde{D}B}\right\} \tag{5-6}$$

$$p(R) = R^3\exp(\kappa R)\left\{\frac{\tilde{D}A - DB}{\tilde{D}A(1+\kappa R) + DB\left[2 + 2\kappa R + (\kappa R)^2\right]}\right\} \tag{5-7}$$

where the coefficients A and B are given respectively,

$$A = \frac{2\sinh(\tilde{\kappa}R)}{(\tilde{\kappa}R)} + \tilde{\kappa}R\sinh(\tilde{\kappa}R) - 2\cosh(\tilde{\kappa}R) \tag{5-8}$$

$$B = \cosh(\tilde{\kappa}R) - \frac{\sinh(\tilde{\kappa}R)}{(\tilde{\kappa}R)} \tag{5-9}$$

μ_a : Absorption coefficient of tissue (a combination of the absorption coefficients of whole blood and blood–free tissue : determined by the volume fraction of blood in the tissue)

μ_s' : Transport scattering coefficient of tissue (a combination of the absorption coefficients of whole blood and blood–free tissue : determined by the volume fraction of blood in the tissue)

$\tilde{\mu}_a$: Absorption coefficient of blood

$\tilde{\mu}_s'$: Transport scattering coefficient of blood

D : Diffusion constant of tissue $\left(=1/[3(\mu_a + \mu_s')]\right)$

$\tilde{D}$: Diffusion constant of blood $\left(=1/[3(\tilde{\mu}_a + \tilde{\mu}_s')]\right)$

κ :Inverse diffusive absorption distance of tissue $\left(=(\mu_a/D)^{1/2}\right)$

$\tilde{\kappa}$:Inverse diffusive absorption distance of blood $\left(=(\tilde{\mu}_a/\tilde{D})^{1/2}\right)$

Detailed derivations of Eqs. (5-1)~(5-9) can be found in [20].

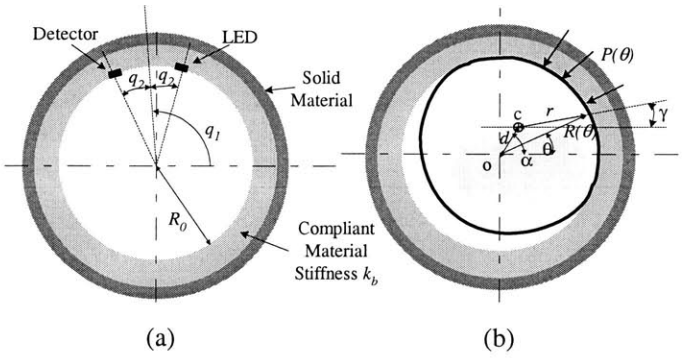

Figure 5-3 (a) Initial state of the ring with LED and photodetector (b) When the finger moves in the ring (Finger tissue is deformed.)

Since the absorption coefficient of blood is larger than that of tissue, the DC value of J increases as the two arteries are located farther from the origin, since more photons reach the detector without passing through the digital arteries. It is also natural that J increases as the radii of the arteries decrease. However, the amplitude of the AC component of J decreases as the distance of the arteries from the origin increases, since the change of the diameters of the arteries (which eventually results in a change of the extent of photon absorption) at distant locations does not influence significantly the photons that reach the detector.

5.3.2 Tissue Mechanical Model

The initial shape of the ring is shown in Figure 5-3(a). The LED and the detector are placed such that their mid-point is at an angle q_1 (rad) from the horizontal axis, and both the LED and the detector are at an angle q_2 (rad) from the radial line that intersects the mid point. As the finger moves inside the ring, the pressure at the contact point increases and both the finger tissue and the compliant material inside the ring go through deformation. This is shown in Figure 5-3(b).

O is the center of the ring and c is the reference point (the initial center point) of the finger located at the bone. As the reference point of the finger moves by displacement d at an angle α, the distance r (represented as a function of γ) from the reference point of the finger to the skin changes from its initial value r_0. At the same time, the compliant material inside the ring also deforms and the distance R (represented as a function of θ) from the center of the ring to the ring inner material also deviates from its initial value R_0. Denoting the pressure at the contact point as P, we can get the force equilibrium equation,

$$
\begin{aligned}
&P(\theta) = [r_0 - r]k_t = [R - R_0]k_b \\
&P(\theta) \geq 0,\ always \Rightarrow r \leq r_0 \ and \ R \geq R_0,\ always \\
&P(\gamma) = [r_0 - r(\gamma)]k_t \quad : P \text{ as a function of } \gamma \\
&P(\theta) = [R(\theta) - R_0]k_b \ : P \text{ as a function of } \theta
\end{aligned}
\tag{5-10}
$$

where k_t is the stiffness of the finger tissue and k_b is the stiffness of the compliant material inside the ring. From Eq. (5-10), we can get the following relationship.

$$
R = R_0 + (r_0 - r)\left(\frac{k_t}{k_b}\right) \tag{5-11}
$$

From the kinematics of the tissue, we can also get the following equations.

$$
r^2 = R^2 + d^2 - 2Rd\cos(\alpha - \theta) \tag{5-12}
$$

$$
R^2 = r^2 + d^2 - 2rd\cos(\pi - (\alpha - \gamma)) \tag{5-13}
$$

Combining Eqs. (5-11), (5-12), and (5-13), the information about the deformation of the finger tissue and the ring inner material is obtained.

$$
R(\theta) = \frac{(r_0 + R_0)^2 - d^2}{2[R_0 + r_0 - d\cos(\alpha - \theta)]} \quad if \ k_b = k_t \tag{5-14a}
$$

$$
R(\theta) = \frac{b - \sqrt{b^2 - ac}}{a} \qquad if \ k_b \neq k_t \tag{5-14b}
$$

where,

$$
a = \left(\frac{k_b}{k_t}\right)^2 - 1
$$

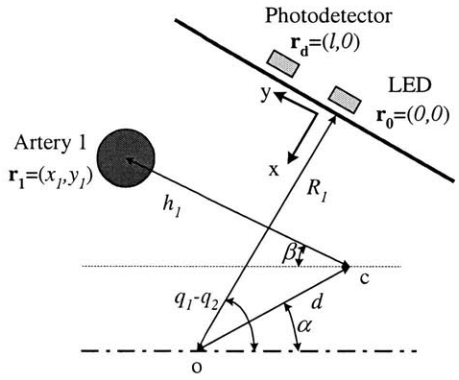

Figure 5-4 Geometry of the LED, the photodetector, artery 1, and the skin capillary layer

$$b = R_0\left(\frac{k_b}{k_t}\right)^2 + r_0\left(\frac{k_b}{k_t}\right) - d\cos(\alpha-\theta)$$

$$c = {r_0}^2 + {R_0}^2\left(\frac{k_b}{k_t}\right)^2 + 2R_0 r_0\left(\frac{k_b}{k_t}\right) - d^2$$

and,

$$r(\gamma) = \frac{(r_0+R_0)^2 - d^2}{2[R_0 + r_0 + d\cos(\alpha-\gamma)]} \quad if\ \ k_b = k_t \tag{5-15a}$$

$$r(\gamma) = \frac{b' - \sqrt{b'^2 - a'c'}}{a'} \quad if\ \ k_b \neq k_t \tag{5-15b}$$

where,

$$a' = \left(\frac{k_t}{k_b}\right)^2 - 1$$

$$b' = R_0\left(\frac{k_t}{k_b}\right) + r_0\left(\frac{k_t}{k_b}\right)^2 + d\cos(\alpha-\gamma)$$

$$c' = {R_0}^2 + {r_0}^2\left(\frac{k_t}{k_b}\right)^2 + 2R_0 r_0\left(\frac{k_t}{k_b}\right) - d^2$$

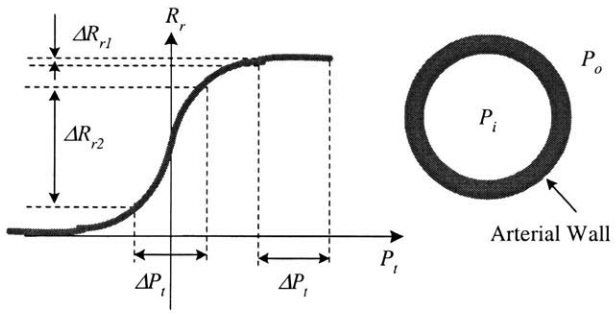

Figure 5-5 Change of arterial wall radius (Rr) with transmural pressure (Pt)

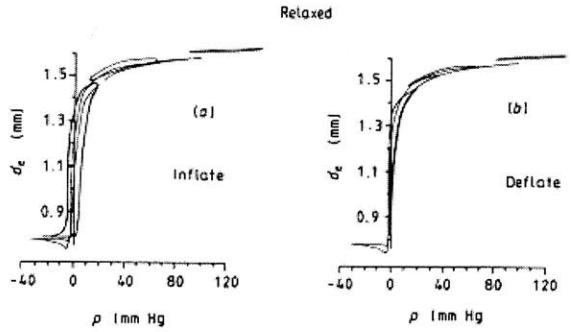

Figure 5-6 Pressure-diameter relationship of human digital artery. The pressure in the x-axis is transmural pressure ($P_i - P_o$), and the y-axis is external diameter. The external diameter is about 0.8 mm when it is completely collapsed, implying that the wall thickness at the collapse is about 0.4 mm. Adopted from [35]

As shown in Figure 5-4, the location of artery 1, which is $\mathbf{r_1}=(x_1, y_1)$ in the optical model given by Eq. (5-1), can be derived using simple kinematics.

$$x_1 = d\sin[\alpha - (q_1 - q_2)] + h_1 \sin[\beta + (q_1 - q_2)] \tag{5-16a}$$

$$y_1 = R_1 - d\cos[\alpha - (q_1 - q_2)] + h_1 \cos[\beta + (q_1 - q_2)] \tag{5-16b}$$

where,

$R_1 = R(q_1 - q_2)$ from Eqs. (5-14a) and (5-14b)

$$h_1 = h_0\left(\frac{r_1}{r_0}\right)$$

where,

$r_1 = r(\pi - \beta)$, from Eqs. (5-15a) and (5-15b)

The location of artery 2, which is $\mathbf{r}_2=(x_2, y_2)$, can also be obtained using similar derivations.

5.3.3 Dynamics of the Arterial Wall

The compliance of the arterial wall changes nonlinearly. There are many factors that influence the arterial wall compliance [30][31], such as temperature, pressure, age, or even the emotions of the person. Among them, pressure is one of the most sensitive factors, and it changes the compliance dramatically. Depending on the transmural pressure P_t, which is defined as the difference between the internal pressure P_i and external pressure P_o, the diameter changes of the digital artery differ even with the same change in blood pressure. Figure 5-5 shows the relationship between the arterial wall radius R_r and the transmural pressure P_t [11][31][32][33][34]. As shown in the figure, even with the same change of transmural pressure ΔP_t, the change of the arterial radii, ΔR_{r1} and ΔR_{r2}, are different depending on the operating point of P_t. The maximum arterial pulsation occurs approximately when the transmural pressure is zero. After this point, the arterial pulsation begins to diminish since the artery becomes occluded by excessive external pressure [11][32]. This is a well-known principle used in oscillometric blood pressure measurement devices.

The internal pressure of the artery, which is actually what we define as "blood pressure," is not actively controllable. However, we can change the amplitude of the volumetric pulsation of the artery by changing the external pressure P_o even under the same blood pressure. In our ring configuration, as the displacement d increases, the pressure around the contact point increases. This also changes the pressure applied to the digital arteries depending on the configuration and position of the ring. To calculate the radii of the arteries (R_{r1} and R_{r2} in Eq. (5-1)), $P(\gamma)$ when $\gamma=\pi-\beta$ and $\gamma=\beta$ must be calculated from Eq. (5-10), and this becomes the external pressures P_{o1} and P_{o2} applied to digital arteries 1 and 2 respectively.

Wesseling *et al.* measured the pressure-diameter relationships of segments of human finger arteries *in vitro* [35]. Figure 5-6 shows their experiment results. The figure clearly shows that there is a

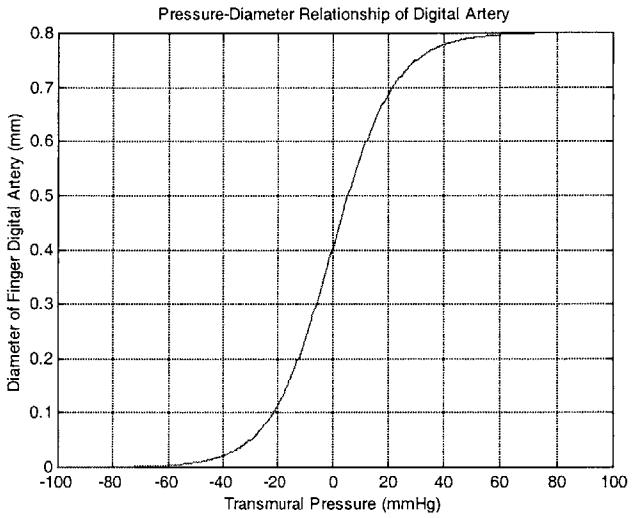

Figure 5-7 Pressure-internal diameter relation curve of digital arteries described by sigmoid function. This curve was fitted to the experiment data in Figure 5-6.

steep slope in the collapse region near zero transmural pressure. According to the experiment, the inner diameter of human digital arteries is approximately 0.8 mm when fully expanded. Considering that there are four digital arteries and two of them (dorsal digital arteries) are smaller than the other two (proper palmar digital arteries), the total volume of fully-expanded digital arteries in a 1 cm finger segment is approximately 0.015 ml.

In this approach, for simplicity, we model the relationship of R_r and P_t as a sigmoid function.

$$R_r = \frac{C_1}{1+\exp\left(-C_2\left(P_t - C_3\right)\right)} \quad \text{(mm)} \tag{5-17}$$

where

$P_t = P_i - P_o$

P_i : *blood pressure inside artery*

P_0 : *pressure outside of artery*

R_r : *radius of digital artery*

Fitting this sigmoid function with the pressure-internal diameter relation curve in Figure 5-6, three constants can be determined as follows.

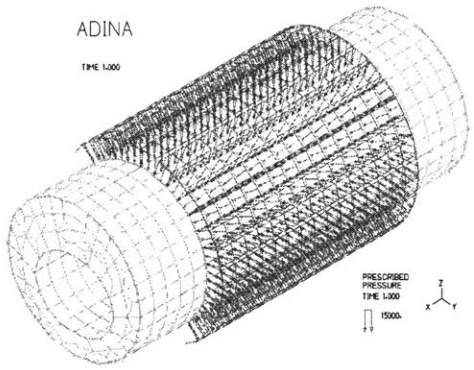

Figure 5-8 Finite element analysis of the finger segment under constant pressure of 120 mmHg. The length of the finger of 4 cm, and a 3cm segment is under pressure.

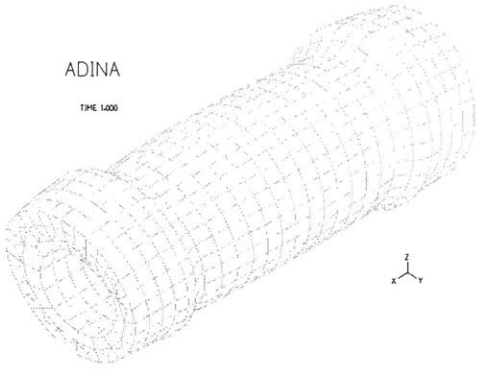

Figure 5-9 Deformed finger segment under external pressure, generated by FEM.

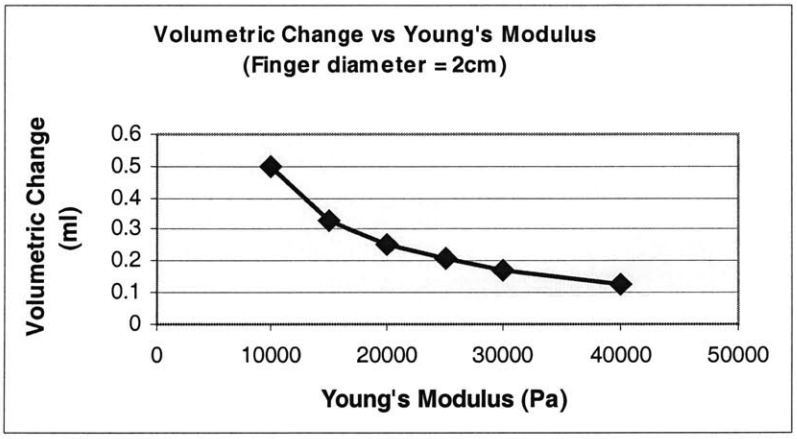

Figure 5-10 Volumetric changes of the finger segment with various values for Young's modulus. The initial diameter of the finger segment is 2 cm, and its length is 1 cm.

$$C_1 = 0.4,\ C_2 = 0.15,\ C_3 = 0$$

The plot of this artery model is shown in Figure 5-7.

Finally, R_{r1} and R_{r2} in Eq. (5-1) can be described as follows.

$$R_{r1} = R_r\left(P_i - P_{01}\right) \tag{5-18a}$$

$$R_{r2} = R_r\left(P_i - P_{02}\right) \tag{5-18b}$$

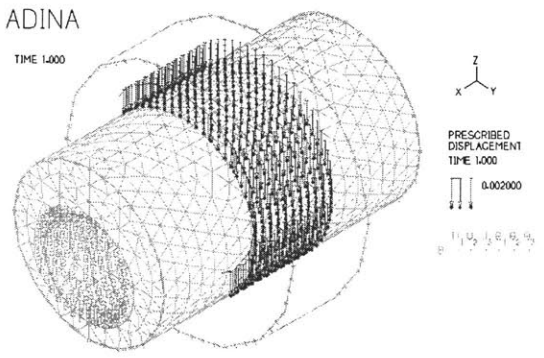

Figure 5-11 FEM Analysis : Single Ring : E=20000, v=0.49, disp=2mm, angle=90 deg

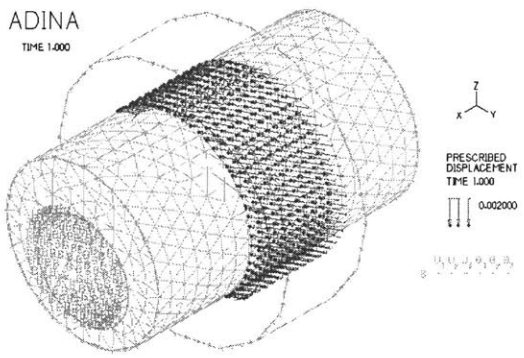

Figure 5-12 FEM Analysis : Single Ring : E=20000, v=0.49, disp=2mm, angle=20 deg

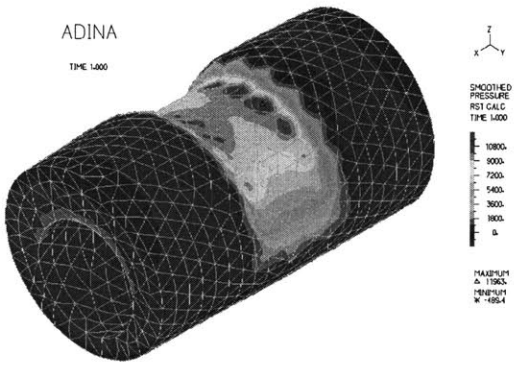

Figure 5-13 Single Ring : E=20000, v=0.49, disp=2mm, angle=90 deg, 3-D View

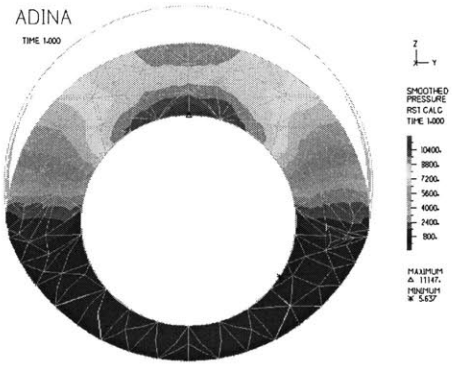

Figure 5-14 Single Ring : E=20000, v=0.49, disp=2mm, angle=90 deg, Cross Sectional View at x=0

where,

$P_{01} = (r_0 - r_1)k_t$, $P_{02} = (r_0 - r_2)k_t$, from Eq. (5-10)

where,

$r_1 = r(\pi - \beta)$, $r_2 = r(\beta)$, from Eqs. (5-15a) and (5-15b)

5.3.4 Parameter Calibration and Estimation

5.3.4.1 Validation of the Model and Determination of Stiffness of the Tissue by FEM

The value of k_t should be determined for the said tissue mechanics model. Although human tissue is a nonlinear, inhomogeneous, anisotropic material, its behavior has been successfully described by isotropic, homogeneous and incompressible constitutive relations [21][22][23]. Since the finger cross section, in this research, is modeled as a group of elastic springs extending in a radial direction, the stiffness of the finger tissue has to be determined. The approach used in this research was to simulate the mechanical deformation of the finger by finite element analysis (FEM), and then find the best value of k_b that describes the behavior closest to the FEM result.

Many researchers have used the finite element method to describe the behavior of human tissue [21][22][23][24][25]. Kamm *et al* conducted an analysis of tissue deformation in the lower leg [21]. He found out that Young's modulus is about 1.2×10^4 (Pa) in the lower leg. Raju conducted FEM of the fingertip and he divided the fingertip into 5 different layers with different mechanical properties [24]. The range of Young's modulus he used for the layers was around 10^3~10^4. Maeno analyzed the contact problem between an elastic finger having a curved surface and an object [22]. He used a rather high elastic modulus of 10^6. Although a number of publications described the elastic modulus of human tissue, no value for the elastic modulus of the finger base could be found. However, there were some researchers who reported experiment results about the volumetric changes of finger segment under a controlled external pressure; Yamakoshi *et al* [9] reported an interesting experiment result about the volumetric change of finger segment. They placed a cuff around the finger segment, and monitored the volumetric change of the finger segment while increasing the cuff pressure. They reported that about 0.26 ml of volume change occurred in the 1 cm finger segment when 120 mmHg cuff pressure was applied around the finger.

Based on their experiment result, we used an indirect approach to estimate the elastic modulus of the finger. We simulated Yamakoshi's experiment with the finite element method, using different values for the Young's modulus of the tissue. The modulus value that produced the closest agreement with the experiment result was employed in the finger model verification. Kamm *et al* [21] used a similar approach in estimating Young's modulus for the lower legs. Figure 5-8 and Figure 5-9 show the finite element model used in this process. FEM analysis was conducted with commercial software (ADINA Version 7.3.2, ADINA, Inc. Watertown, MA). The finger segment was simplified to be a cylinder of 2 cm diameter with 5cm length. A uniform pressure of 120 mmHg was applied to the surface of the cylinder along a 3 cm segment. This length is the same as that of the finger cuff used by Yamakoshi. Multiple 3-D simulations with different Young's moduli

were conducted, and the volumetric change for each simulation was measured. As in Yamakoshi's experiment, the volumetric change was measured only at the 1 cm segment in the center. Figure 5-10 shows the volumetric changes of the finger segment with various values for Young's modulus generated by FEM. This analysis shows that the volumetric change is closest to the expected value of 0.26 ml when the Young's modulus of 2.0×10^4 (Pa) was chosen. Using this value, another 3-D finite element analysis was conducted. Figure 5-11 is the schematic of the FEM analysis when the finger ring moved downward (external force from θ=90 degrees), and Figure 5-12 is the same FEM analysis when the finger ring is moved to the side. (external force from θ=20 degrees). Figure 5-13 and Figure 5-14 show the two simulation results of the deformed finger cross section. The finger diameter is 2 cm and the length of the segment is 4 cm. The width of the ring is 1 cm. The ring was given a displacement of 2 mm from the top. The FEM simulation result in Figure 5-14 shows that the contour lines of the pressure roughly lie in the radial direction. This means that our radial-spring assumption of the finger tissue behavior is actually quite reasonable. While trying to fit the value of k_t to the FEM analysis result, it was also found that the spring constant should vary depending on the location as a function of the angle. This is mainly due to the fact that the thickness of the tissue (the distance from the skin to the surface of the bone) is not uniform with the angle. Fitting the spring constant of the tissue from this analysis, k_t is determined to be as follows.

$$k_t(\theta) = 25\cos\left(\theta + \frac{\pi}{2}\right) + 64 \quad (mmHg/mm) \tag{5-19}$$

where θ is the angle of the tissue of interest. This value of k_t will be used in the numerical simulation of the whole model.

5.3.4.2 Determination of Optical Properties : Capillaries and Veins

Since the tissue is assumed to be a homogeneous composite of blood-free tissue, the whole blood in the capillaries, and the whole blood in the veins, the absorption and scattering constants of the tissue are expressed in terms of the coefficients of the blood-free tissue and the whole blood, and the volume fractions of the three materials.

$$\mu_a = \frac{\tilde{\mu}_{at} V_t + \tilde{\mu}_a (V_c + V_v)}{V_t + V_c + V_v} \tag{5-20a}$$

$$\mu_s' = \frac{\tilde{\mu}_{st}' V_t + \tilde{\mu}_s' (V_c + V_v)}{V_t + V_c + V_v} \tag{5-20b}$$

μ_a : Overall absorption coefficient of the tissue

$\tilde{\mu}_{at}$: Absorption coefficient of the blood-free tissue

$\tilde{\mu}_a$: Absorption coefficient of the whole blood

μ_s' : Overall transport scattering coefficient of the tissue

$\tilde{\mu}_{st}'$: Transport scattering coefficient of the blood-free tissue

$\tilde{\mu}_s'$: Transport scattering coefficient of the whole blood

V_t : Volume of the blood-free tissue

V_c : Volume of the blood in the capillaries and small artery branches

V_v : Volume of the blood in the veins

According to [19], the conventional values of $\tilde{\mu}_{at}$ and $\tilde{\mu}_{st}'$ are 0.03 /mm and 1.0 /mm, respectively. $\tilde{\mu}_a$ and $\tilde{\mu}_s'$ can be also calculated as,

$$\tilde{\mu}_a = \sigma_a \rho \tag{5-21a}$$

$$\tilde{\mu}_s' = \bar{\sigma}_s \rho (1 - \mathrm{HCT}) \tag{5-21b}$$

where $\bar{\sigma}_s$ is the backscattering cross section, and σ_a is the absorption cross section of red blood cells. HCT is the blood hematocrit (~0.45), and ρ is the red-cell density. $\rho = \mathrm{HCT} / \bar{V}$ where $\bar{V} (= 87 \times 10^{-9} \mathrm{mm}^3)$ is the red-cell volume. The conventional value of $\bar{\sigma}_s$ is $0.558 \times 10^{-6} \mathrm{mm}^2$ [19] and σ_a can be calculated as,

$$\sigma_a = \sigma_{ao} (\mathrm{OS_T}) + \sigma_{ar} (1 - \mathrm{OS_T}) \tag{5-22}$$

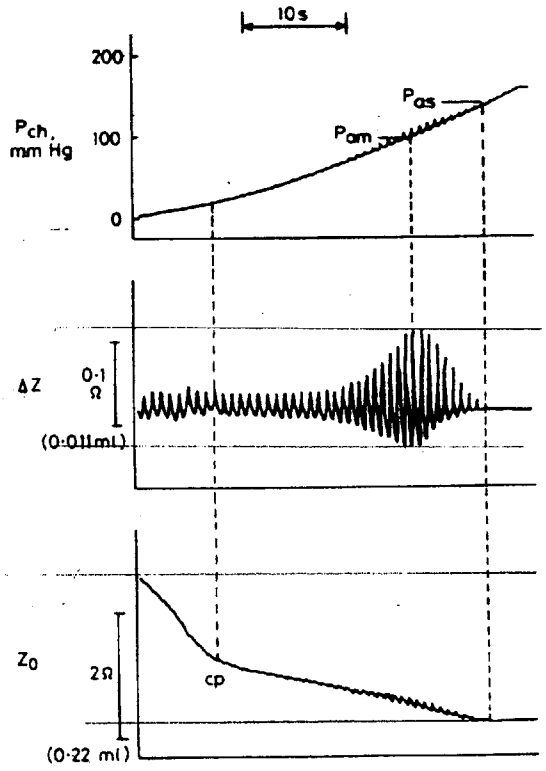

Figure 5-15 Simultaneous recordings of chamber pressure (P_{ch}), AC components of impedance variation (ΔZ), and DC components of the impedance variation (Z_o). The impedance of the electrolyte solution decreases as the finger volume decreases. Adopted from [9].

where OS_T is the oxygen saturation (~0.95 typically) and σ_{ao} and σ_{ar} can be obtained for various light wavelengths from [26]. For λ=660nm (red light), σ_{ao} and σ_{ar} are around 0.044×10^{-6} (mm^2) and 0.455×10^{-6} (mm^2), respectively. For λ=950nm (IR light), σ_{ao} and σ_{ar} are around 0.173×10^{-6} (mm^2) and 0.102×10^{-6} (mm^2), respectively. As a result, $\tilde{\mu}_s'$ is 1.59 /mm, and $\tilde{\mu}_a$ is 0.334 /mm (λ=660nm) or 0.877 /mm (λ=950nm). These values are also in good agreement with the range of absorption and scattering coefficients of human tissue suggested by [27] and [28].

To get the overall optical properties of the tissue, the volumes of the components (i.e. the blood-free tissue, the blood in the capillaries, and the blood in the veins) should be found. Although no values for the volume fractions of these components in the finger cross section could be found in the literature, they can be estimated from available experiment results published in the literature. Yamakoshi *et al.* [9] measured the volume change of a middle finger as the pressure in the cuff placed around the finger increased (Figure 5-15). They reported that the finger volume decreased by 0.26 ml in a 1cm finger segment as the cuff pressure increased from 0 to around 150 mmHg. At this cuff pressure, it is certain that even digital arteries would be occluded. If we assume that this finger

volume decrease of 0.26 ml is mainly due to the absence of blood (i.e. the blood is "squeezed" out of the finger segment), we can say that the volume of the blood in the segment was originally 0.26 ml. They also reported that the AC part of the volume change was maximum at around 90 mmHg, corresponding to the mean arterial pressure, and the maximum volume change was 0.015 ml. Noting that capillaries and veins are already occluded at this high pressure, we can say that this amplitude is the volumetric change of the blood in the digital arteries (the two proper palmar digital arteries and the two dorsal digital arteries), which agrees with the conjecture made in the previous section. Their experiment results also showed that approximately half of the volume change occurs in the lower pressure range. After this point, the slope of volume change becomes less stiff. Yamakoshi *et al.* [10] measured this inflection point, and suggested that it corresponds to the highest venous pressure. Therefore, it can be said that the capillary occlusion begins approximately from this inflection point. Yamakoshi measured this inflection point in several subjects and estimated it to be around 15 mmHg.

From these arguments, about half of the blood in the finger segment can be considered to be venous blood (including venulus), and the other half can be considered to be capillary and arterial blood. From the experiment result of [9], the total volume of the blood in the four digital arteries represents only about 5 percent of all the blood in the finger segment. Considering that about half the blood in the cross section is venous blood, approximately 45% of the blood resides in the capillaries and arterioles other than the four digital arteries. In the same experiment result, it was shown that the volumetric change of the finger segment at low pressure was about 0.003 ml. Unlike the digital arteries that show continuous volume change with pressure, capillaries are thought of as on-off type tubes. The number of occluded capillaries increases as the external pressure increases. In this case, we can model the pulsating volume of the blood in the capillaries and small arterioles (V_c) as a function of arterial blood pressure. Its DC value can be modeled as a linear decreasing function of external pressure, where its AC part is synchronized with arterial blood pressure pulsation with an amplitude of approximately 3 percent (0.003/0.11) of its DC part. V_c is considered to be zero after P_{as}, as was shown in the experiment result of [9]. Since the capillary pressure in the arteriolar end is 30.6~34.3 mmHg [29], most of the capillaries are occluded in the higher pressure range (>~40 mmHg). After about 40 mmHg, V_c is mostly the volume of the arterioles and small artery branches, and volumetric pulsation occurs mostly due to the arteries and arterioles.

$$
\begin{aligned}
V_c &= a\left[\left(\frac{P_a - P_{am}}{P_{as} - P_{ad}}\right)\times 0.03 + 1\right] && (ml) \quad when\ P_o < P_{\inf} \\
V_c &= b\left(\frac{P_{as} - P_o}{P_{as} - P_{\inf}}\right)\left[\left(\frac{P_a - P_{am}}{P_{as} - P_{ad}}\right)\left(\frac{P_{ad} - P_o}{P_{ad} - P_{\inf}}\right)\times 0.03 + 1\right] && (ml) \quad when\ P_{\inf} < P_o < P_{ad} \\
V_c &= c\left(\frac{P_{as} - P_o}{P_{as} - P_{\inf}}\right) && (ml) \quad when\ P_{ad} < P_o < P_{as} \\
V_c &= 0 && (ml) \quad when\ P_o > P_{as}
\end{aligned}
\tag{5-23}
$$

P_a : Arterial blood pressure

P_m : Mean arterial blood pressure

P_{as} : Systolic arterial pressure

P_{ad} : Diastolic arterial pressure

P_o : Pressure applied from outside

P_{inf} : Pressure at inflection point

Fitting the constants *a, b*, and *c* with the curve in Figure 5-15, we can get $a = b = c = 0.12$. From the above argument, it is also clear that V_v is decreasing from 0.13 ml to zero with external pressure ranging from 0 to P_{inf}.

$$
\begin{aligned}
V_v &= 0.13\frac{(P_{\inf} - P_o)}{P_{\inf}} && (ml) \quad P_o < P_{\inf} \\
V_v &= 0 && (ml) \quad P_o > P_{\inf}
\end{aligned}
\tag{5-24}
$$

and,

$$
V_t = \pi R^2 - 0.26 \quad (ml) \tag{5-25}
$$

where R is the radius of the finger cross section (~1 cm). The total volume of the 1cm length finger segment will be,

$$
V = V_t + V_c + V_v + V_a \tag{5-26}
$$

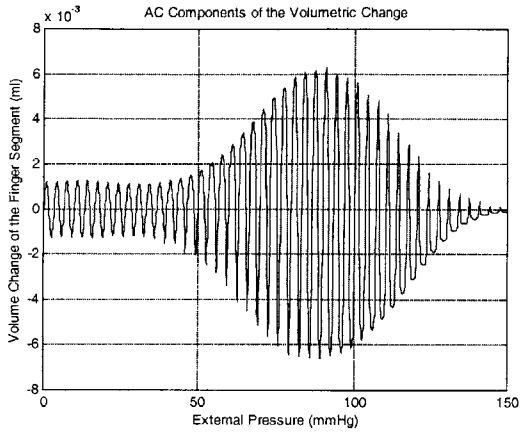

Figure 5-16 Numerical simulation result of the volume change (AC components) of 1 cm finger segment under external pressure

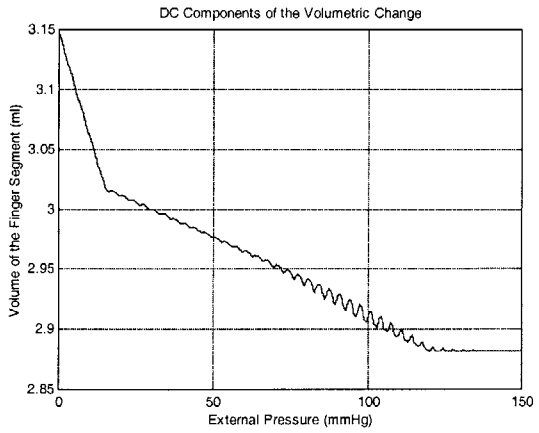

Figure 5-17 Numerical simulation result of the volume change (DC components) of 1 cm finger segment under external pressure

where V is the total volume and V_a is the blood volume in digital arteries. V_a can be determined by the analysis done in the previous section.

Unlike the case of cuff pressure, P_o is not uniform around the finger in the ring sensor configuration. This means that the optical properties of the tissue are not uniform in the finger cross section. Since the important optical properties are those around the sensing area, the pressure around the optical sensors can be used for P_o in this model.

5.3.5 Completing the Blood Vessel Model

Now that we have all the components necessary to complete a blood vessel model of the finger, we can do a simulation of the volumetric change of the finger segment as a function of external pressure by using Eq. (5-26). Figure 5-16 and Figure 5-17 show the result of the numerical simulation. The heart rate was set to be 90 /min, and the blood pressure was set to be 120/90. From the figure, it is clear that the AC part of the volumetric change of blood reaches its maximum around the mean blood pressure. However, it is also seen that the exact maximum point of the simulation is less than the actual mean blood pressure by 5~10 mmHg. This fact has been reported by many researchers [11]. This is one of the well-known defects of the oscillometric pressure monitoring method. The DC part of the simulation result agrees well with the actual experiment result shown in Figure 5-15.

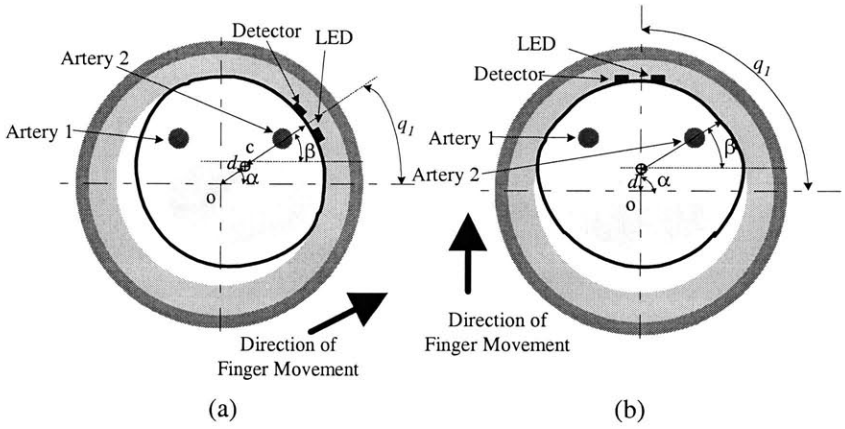

Figure 5-18 Two cases of finger movements in the ring

(a) Case 1 : $\alpha = \beta = q_1$, $q_2 = 10^o$
(b) Case 2 : $\alpha = q_1 = 90^o$, $q_2 = 10^o$

The tissue mechanical model and blood vessel models have been verified by FEM and known experiment results. Combining the mechanical model describing the locations of the two arteries, the arterial wall dynamics equations given by Eqs. (5-26a) and (5-26b), and the optical model equations given by Eqs. (5-1), (5-20a), and (5-20b), the whole model is completed.

5.4 Verification by Finite Element Method, Numerical Simulation and Experiment

Numerical simulations and experiments were conducted with different angles of movement. The numerical simulations were performed using MATLAB version 5.2. The first case (Figure 5-18(a)) is when the direction of movement is aligned with that of a digital artery. In the second case (Figure 5-18(b)), the finger moves in the direction of the mid-point of the two digital arteries. In the numerical simulations, the blood pressure (internal pressure P_i) is given as a combination of two sinusoidal functions, one with a frequency of 1.2 Hz and the other 2.4 Hz. By this combination, we can closely simulate the two-peak feature of a real heartbeat. For the optical coefficients, the values of $\tilde{\mu}_a = 0.877/mm$, and $\tilde{\mu}_s' = 1.59/mm$ are used in the numerical simulations, as was discussed in the previous sections. μ_a and μ_s' are determined by Eqs. (5-20a) and (5-20b). In the experiments, LEDs and the photodetector are packed in a sensor unit board, and the ring is positioned so that the sensor is aligned in the direction of movement in each case. ($\alpha = q_1$)

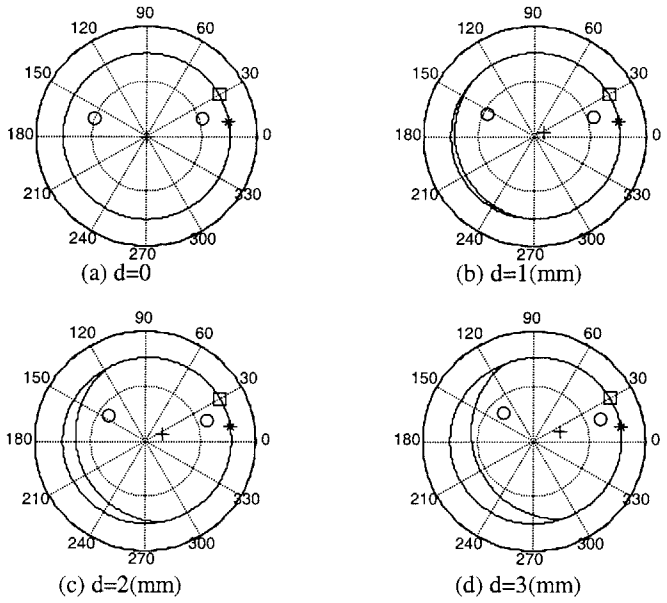

Figure 5-19 : Visualization of movement at case 1. It is shown that the finger shape becomes more oval as *d* increases.

5.4.1 Analysis of the Simulation and Experiment : Case 1

When the direction of the finger movement is aligned with the location of a digital artery ($\alpha=\beta$), it is expected that the amplitude of the photoplethysmograph will change greatly as d (displacement) increases due to two reasons. First, since the sensor is aligned with a digital artery, the distance from the artery and the photodetector will decrease significantly as d increases. This will result in a bigger change in light absorption by the blood with the same change in the diameter of the digital artery. Secondly, since the direction of movement is aligned with the location of a digital artery, the external pressure around the artery, which is P_o, will increase quickly, arriving at the maximum pulsation point of the transmural pressure more easily. This will also give a more highly pulsating signal at the photodetector. Figure 5-19 shows the numerical simulation result of the finger and the ring configuration at case 1 with a gradual increase of displacement d. The large outer circle represents the ring, and the inner line that resembles a distorted circle is the finger surface. The two small circles inside the finger represent the two digital arteries, and the plus sign (+) inside the finger represents the reference point of the finger (which was denoted as point c in previous figures). It can be clearly seen that this reference point moves in the direction of a digital artery as the displacement increases, and the digital artery moves closer to the LED and the photodetector,

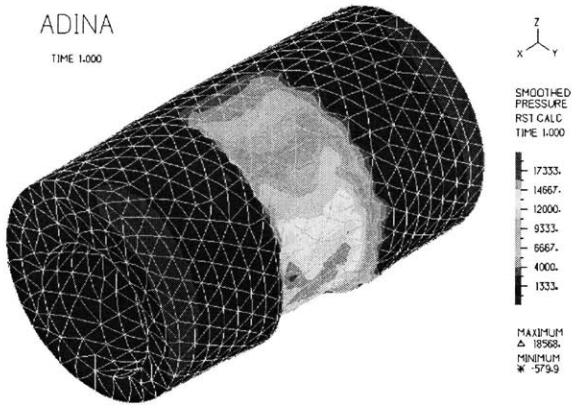

Figure 5-20 Single Ring – 3-D View : E=20000, v=0.49, disp=2mm, angle=20 deg

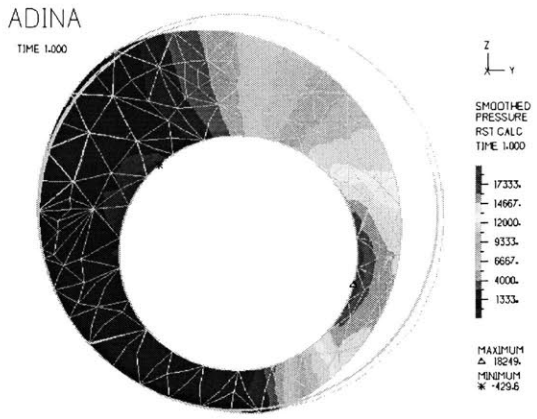

Figure 5-21 Single Ring : E=20000, v=0.49, disp=2mm, angle=20 deg, Cross sectional view at x=0

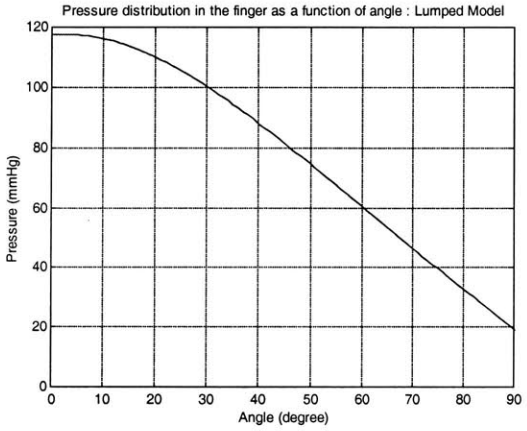

Figure 5-22 Pressure distribution as a function of angle in the finger cross section generated by the lumped parameter model. The angle of displacement is 20 degrees and displacement is 2 mm.

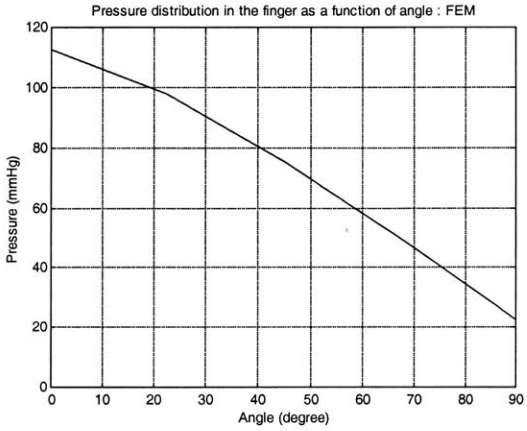

Figure 5-23 Pressure distribution as a function of angle in the finger cross section generated by finite element method. The angle of displacement is 20 degrees and displacement is 2 mm.

which are represented as a small square (□) and a small star (*) on the finger surface at around 20 degrees respectively. The same numerical simulation was done using ADINA. Figure 5-12 shows the configuration, and Figure 5-20 and Figure 5-21 show the result of the FEM analysis. Figure 5-21 is the cut-plane view in the center. It is clearly seen that the pressure at the tissue around θ=20 degrees is the maximum. Since one of the two proper palmar digital arteries resides in this region, the artery will be under significant pressure, resulting in a large pulsation due to the nonlinearity of the compliance of the arterial wall. The pressure around one of the digital arteries (θ=20 degrees) increases as high as almost 120 mmHg, as is shown in Figure 5-22. Figure 5-23 shows the pressure

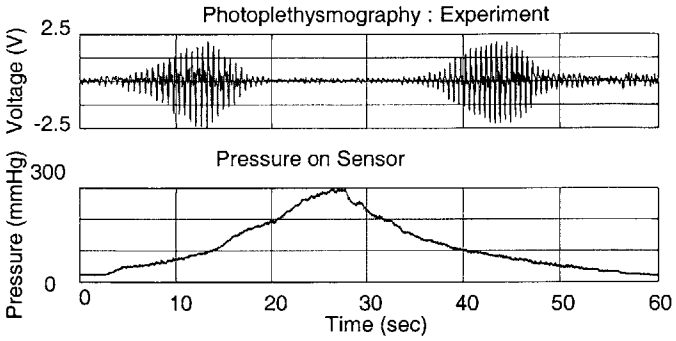

Figure 5-24 Photoplethysmography and pressure at sensor unit from experiment in case 1

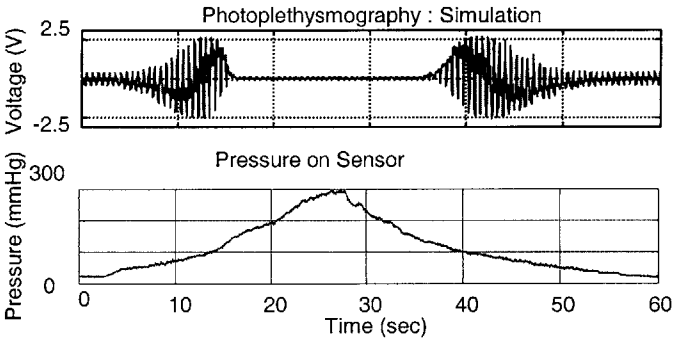

Figure 5-25 Photoplethysmography and pressure at sensor unit from numerical simulation in case 1

distribution as a function of θ calculated by FEM analysis. This curve is similar to the curve in Figure 5-22 that was generated by the lumped parameter model, implying that our lumped parameter model is valid for calculating the pressure distribution.

From the viewpoint of the arterial wall dynamics, it is expected that the amplitude of the photoplethysmograph will increase as the relative displacement of the finger to the ring increases up to a certain point where the transmural pressure goes to zero. After that peak point, the amplitude is expected to decrease since the digital artery will begin to be occluded. The simulation results and the experiment results are shown in Figure 5-24 and Figure 5-25 respectively. The upper plots of Figure 5-24 and Figure 5-25 are the photoplethysmographs, and the bottom figures are the pressures at the sensor unit. Both results show that there is a certain point of external pressure P_o at which the amplitude of the photoplethysmograph becomes the maximum. The experiment result of case 1 shows a small oscillation even at very high external pressure. This is because the pressure is not applied evenly around the finger, but rather, locally applied. Therefore, the pulsation of the blood

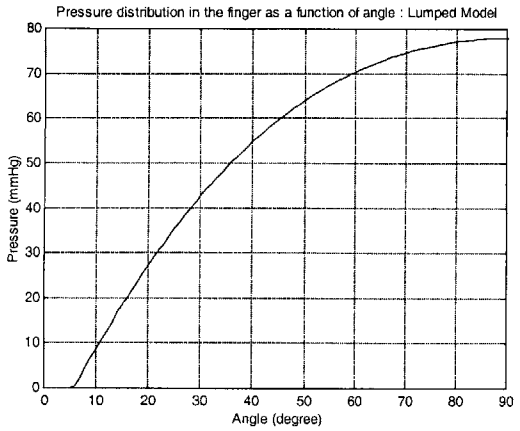

Figure 5-26 Pressure distribution as a function of angle in the finger cross section generated by the lumped parameter model. The angle of displacement is 90 degrees and displacement is 2 mm.

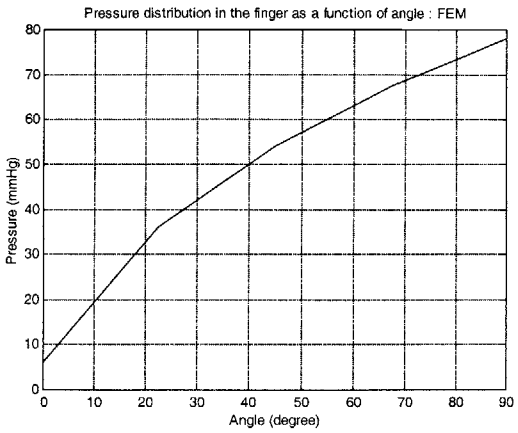

Figure 5-27 Pressure distribution as a function of angle in the finger cross section generated by finite element method. The angle of displacement is 90 degrees and displacement is 2 mm.

vessels located relatively far from the contact point can still be captured by the optical sensor even though the amplitude of the optical signal is very small.

5.4.2 Analysis of the Simulation and Experiment : Case 2

The second case is when the direction of finger movement is towards the middle point of the two digital arteries, i.e, to the palm side (α=90^{o}). In this case, the change in amplitude of the photoplethysmograph with finger displacement is not expected to be as great as in case 1 since the pressure increase at the artery is not as much as in case 1 for the same extent of displacement. In addition, since the distances of the two digital arteries from the sensor unit are geometrically longer than those of case 1, the overall amplitude of the photoplethysmography signal will not be large. This means that the amplitude of the photoplethysmograph will not change much even though the finger moves significantly in the direction of the palm side. This conjecture is also supported by the FEM analysis shown in Figure 5-13 and Figure 5-14. Although the pressure around the two digital arteries increases, it does not increase as much as in case 1. As is shown in Figure 5-26, the pressure around a digital artery (θ=20 degrees) only increases up to 30 mmHg. At this external pressure, the digital artery will not show any significant amplitude of pulsation. The pressure-angle curve generated by FEM analysis shows a similar trend. Thus, it is expected that the amplitude of the signal will remain very small regardless of the finger displacement. The movement of the finger in the ring is graphically visualized using our model in Figure 5-28.

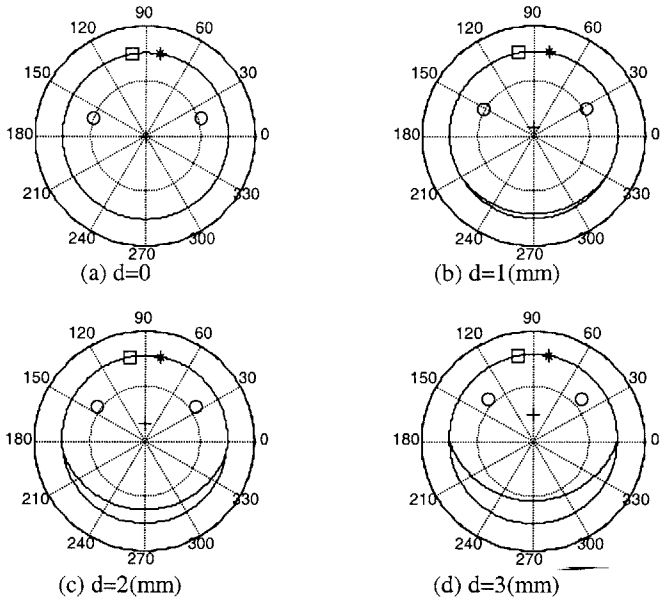

Figure 5-28 Visualization of movement at case 2. It is shown that the reference point (denoted as '+') moves toward the middle point of two arteries as *d* increases.

The experiment result is shown in Figure 5-29, and the simulation result in Figure 5-30. As was expected, the amplitude of the photoplethysmograph in the experiment shows almost no change. In this configuration, it is even hard to recognize the pulse, in both the experiment and simulation. In both results, the amplitude becomes a little larger at low pressures. This slight increase of the amplitude is from the pulsation of the capillaries on the palm side of the finger. Capillaries usually become occluded at an external pressure of around 10~35 mmHg since the internal blood pressure of the capillaries is around that range [29]. This explains the disappearance of pulsation at higher pressures in the experiment result in case 2. In other words, the photoplethysmograph of case 2 catches the pulsation from the capillaries when the external pressure is low. However, as the external pressure increases above 10~35 mmHg, this pulsation disappears as the capillaries become occluded. Since the arterial pulsation cannot be apparently detected by the photoplethysmography in this configuration because the distance between the arteries and the sensor is too far, we can see almost no pulsation at higher external pressures. Rather, the pulsation of the capillaries plays a major role at low external pressures, although its amplitude is much smaller than in case 1, in which the photoplethysmograph is mostly driven by arterial pulsation at higher pressures. The simulation result exhibits a similar behavior.

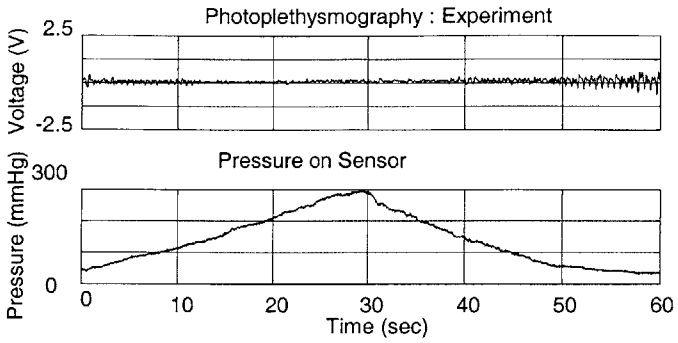

Figure 5-29 Photoplethysmography and pressure at sensor unit from experiment in case 2

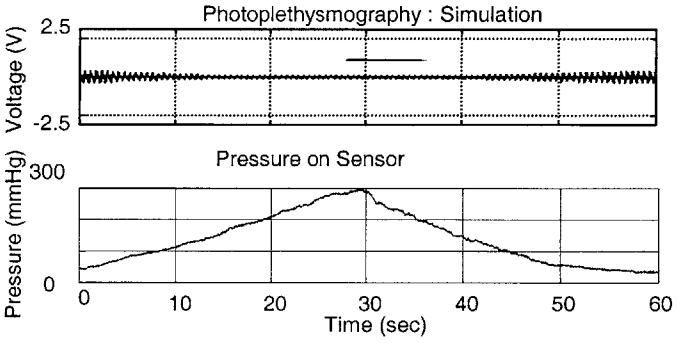

Figure 5-30 Photoplethysmography and pressure at sensor unit from numerical simulation in case 2

Although we can catch a much stronger pulsating signal by applying a high external pressure of around 80~100 mmHg, it is not practical to use this kind of high pressure since it will occlude all the capillaries and block the venous return. This will result in a jamming of the peripheral circulation and the finger will fall into necrosis eventually. Therefore, it is recommended to use a lower external pressure such as 10 mmHg. In this case, we capture mostly capillary pulsation.

5.5 Verification of advantages of the isolating ring sensor by finite element method

As was verified in the model, the photoplethysmographic signal changes much depending on the pressure applied to the blood vessels. From the viewpoint of physiological signal monitoring, it is not recommended that the monitored signal fluctuate due to external disturbance. For example, if the ring sensor moves due to any external force, such as in the case shown in Figure 3-1, the

monitored signal will vary since the pressure applied to the blood vessels changes. From this argument, if the pressure change can be minimized given the same amount of displacement, the signal variation will be minimized. Figure 5-31 and Figure 5-32 show the FEM model of the simplified finger segment with isolating ring sensor. Each ring has 3 mm of width, and the two rings are separated by 12 mm. The optical sensor unit is attached in the middle of the two rings, and the unit is mechanically decoupled from the two outer rings. Figure 5-33 and Figure 5-34 show the pressure distribution of the finger segment when the outer rings are moved by an external force from θ =90 degrees. Figure 5-34 is the cross section of the finger segment in the middle of the two outer rings. From this figure, it is clear that the maximum pressure in this cross section is less than 1400 Pascal ($\approx$ 10.5 mmHg), although the cross section of the contact point is much more distorted and its pressure is much higher (Figure 5-35). Comparing this result with that of Figure 5-14, in which there was a maximum pressure of about 11150 Pascal ($\approx$ 83.8 mmHg), it is obvious that the pressure increase at the sensing point is significantly small in the isolating ring configuration. In other words, when the ring is pushed by the same external pressure, the pressure variation at the sensing point is much smaller in the isolating ring sensor, and this will result in a smaller fluctuation of the photoplethysmographic signal. This argument is also supported by comparing the other two FEM results (Figure 5-21 and Figure 5-38), in which external force is coming from θ = 20 degrees. In the case of the single ring configuration in Figure 5-21, the maximum pressure generated by the 2 mm displacement of the ring is around 18250 Pa ($\approx$ 137 mmHg), while that in the case of the isolating ring sensor in Figure 5-38 is only around 1120 Pa ($\approx$ 8.4 mmHg). It is clear that the pressure variation is much less sensitive to external forces with the isolating ring sensor.

The pressure variation due to displacement of the ring body can be further reduced by making the distance between the two outer rings longer. Figure 5-41 and Figure 5-42 show the FEM analysis of this case. The distance between the two outer rings is 18 mm. The maximum pressure on the finger cross section in the middle is about 300 Pa ($\approx$ 2.3 mmHg), which is even less than the case of Figure 5-34. Therefore, it is better to have more distance between the two outer rings. However, there are limitations to this approach, since the distance cannot be longer than the distance between knuckles. In addition, it is not recommended to make the distance too long since that will make the device inconvenient for people to wear for a long time. Thus, once again, a tradeoff will be needed in the practical design of the isolating ring sensor.

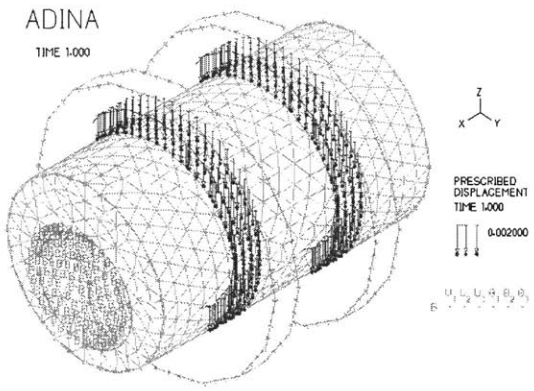

Figure 5-31 FEM Analysis : Isolating Ring : E=20000, v=0.49, disp=2mm, angle=90 deg

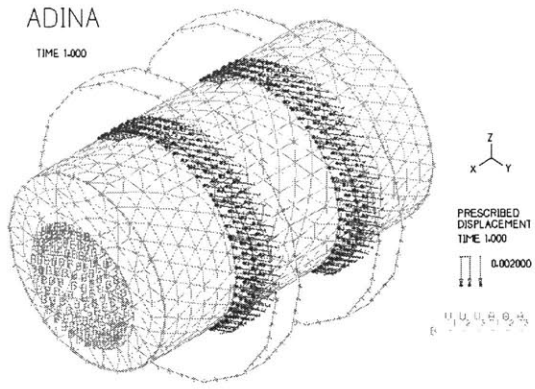

Figure 5-32 FEM Analysis : Isolating Ring : E=20000, v=0.49, disp=2mm, angle=20 deg

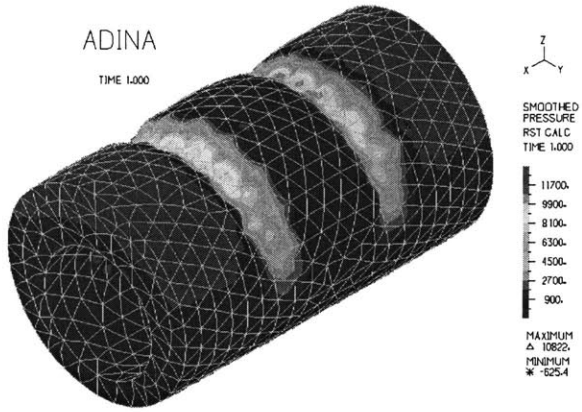

Figure 5-33 Isolating Ring : E=20000, v=0.49, disp=2mm, angle=90 deg, 3-D View

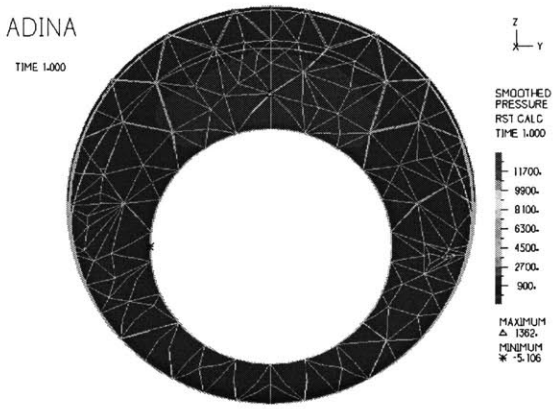

Figure 5-34 Isolating Ring : E=20000, v=0.49, disp=2mm, angle=90 deg, Cross Sectional View at x=0

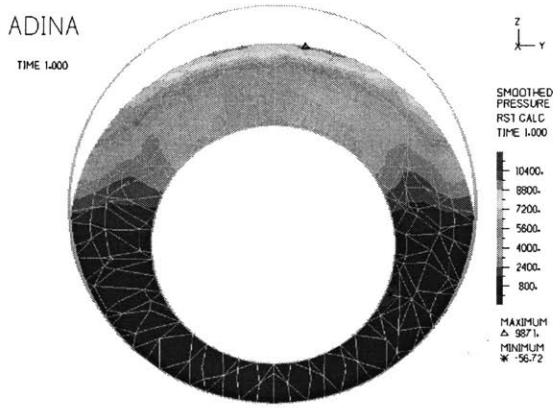

Figure 5-35 Isolating Ring : E=20000, v=0.49, disp=2mm, angle=90 deg, Cross Sectional View at the Outer Ring

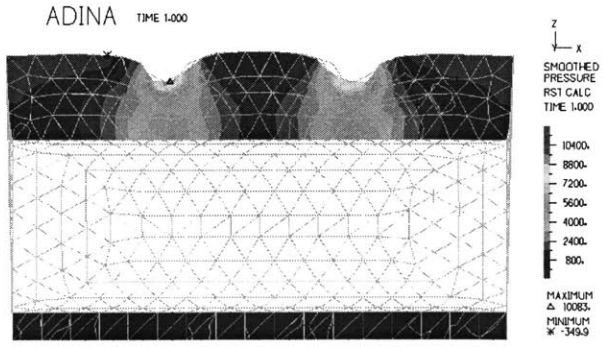

Figure 5-36 Isolating Ring : E=20000, v=0.49, disp=2mm, angle=90 deg, Longitudinal View

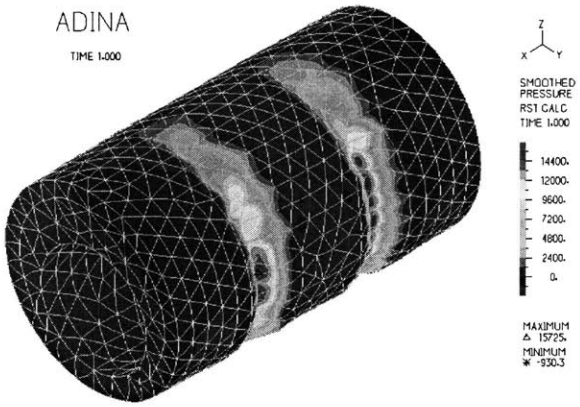

Figure 5-37 Isolating Ring : E=20000, v=0.49, disp=2mm, angle=20 deg, 3-D View

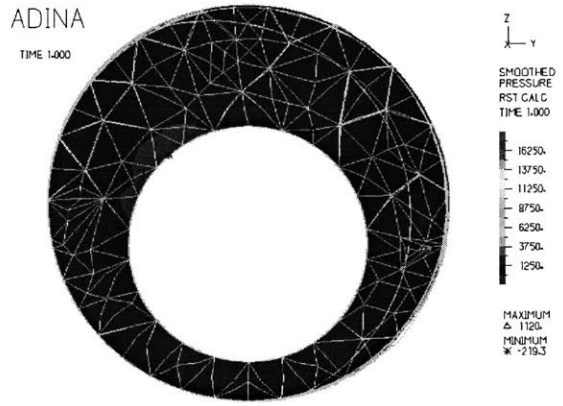

Figure 5-38 Isolating Ring : E=20000, v=0.49, disp=2mm, angle=20 deg, Cross Sectional View at x=0

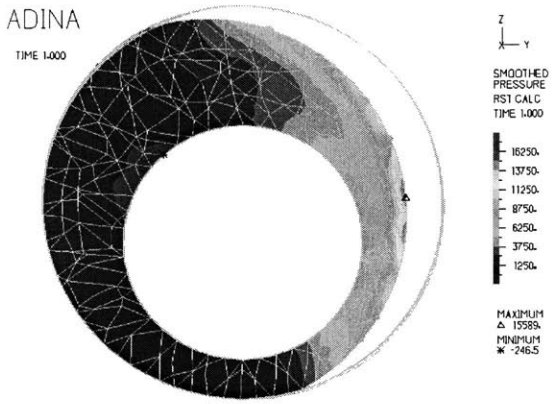

Figure 5-39 Isolating Ring : E=20000, v=0.49, disp=2mm, angle=20 deg, Cross Sectional View at the Outer Ring

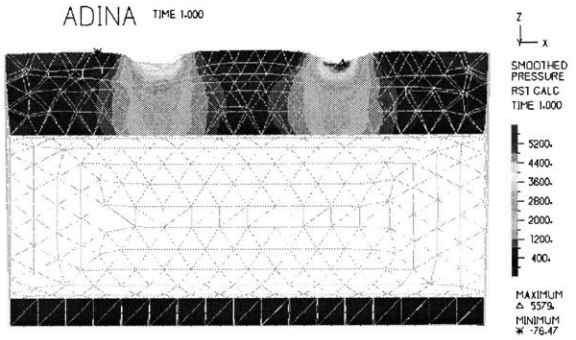

Figure 5-40 Isolating Ring : E=20000, v=0.49, disp=2mm, angle=20 deg, Longitudinal Cut-Plane View

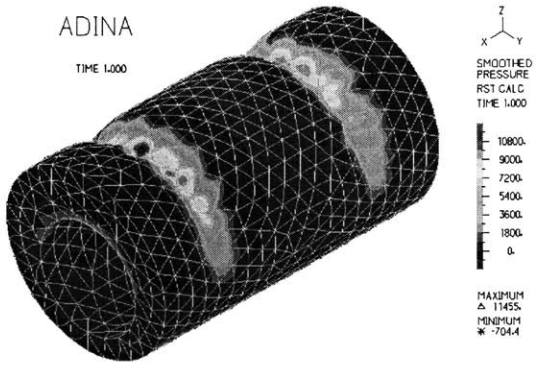

Figure 5-41 Isolating Ring : E=20000, v=0.49, disp=2mm, angle=90 deg, Wide Ring, 3-D View

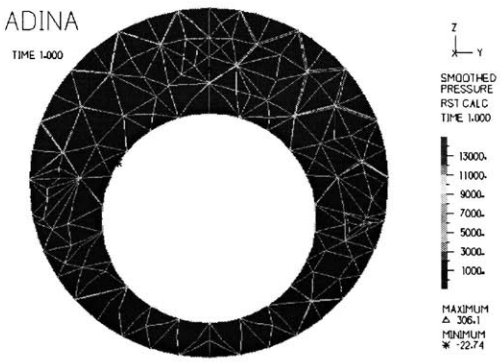

Figure 5-42 Isolating Ring : E=20000, v=0.49, disp=2mm, angle=90 deg, Wide Ring, Cross Sectional View at x=0

6. SIGNAL PROCESSING WITH CORRELATION FUNCTIONS

6.1 Background

In all kinds of wearable sensors, one of the most difficult problems to deal with is the noise issue, especially the questions of how to eliminate ambient light and how to reduce motion artifact. In our ring device, this issue is critical because optical sensors are used to detect an extremely faint signal, which is buried in relatively strong noise from many sources. Unlike other types of sensors, optical sensors are very susceptible to all kinds of disturbances that affect the path of the photons. For example, the air gap between the sensor (the photodiode in this case) and the skin drastically influences on the quality of the received signal. Even a faint trembling of the hand can change the air gap and the obtained signal might swing irrespective of the actual heartbeat. Even a small variation in the intensity of the ambient light can suddenly increase or decrease the amount of photons received by the optical detector.

Although there are thousands of things that can disturb the optical path of the ring device, most of them belong to two categories: motion artifact and ambient light change. Motion artifact is mainly a relatively low frequency disturbance, and it is essentially non-periodic as long as it is not caused by an intentional periodic movement. Change in ambient light is also non-periodic under normal room conditions. These two major noise factors can be effectively treated with a combination of a classical low pass filter and the signal correlation technique.

Of course, if the noise is much stronger than the pulse signal, there is very little chance to reconstruct the original waveform no matter what kind of fantastic signal processing method is used. For example, if the noise is so strong that the detected signal goes beyond the range of detection (i.e. the signal becomes saturated), it is impossible to recover the pulse signal, which is completely buried in the noise. But if we limit the scope of the noise reduction issue in the ring sensor as a 24-hour pulse rate monitoring device, then the correlation method is one of the strongest methods that can be used. In other words, the correlation method can be best used for the continuous monitoring of the pulse rate even in the presence of severe noise sources, since this

method works surprisingly well in separating the periodic component of the heart pulsation and the non-periodic noise components.

In this chapter, a theoretical analysis of how to apply the correlation technique is first explained. Secondly, a numerical simulation is done to verify the usefulness of the correlation method in detecting a desired signal with a low signal-to-noise ratio. Finally, several signal processing results with real experimental data are presented.

6.2 Theory

6.2.1 General Description of the Signal Conditioning Process

The autocorrelation method is a very powerful tool for catching a periodic signal buried in a random signal. This method is especially useful in its application to our ring sensor since the technique works even under a relatively low signal-to-noise ratio. The noise sources that contaminate the heartbeat signal are mostly non-periodic (ex: artifact by random motion) or periodic at a much higher frequency than the heartbeat (ex: ambient light). Therefore, if we get rid of the high frequency noise with a low pass filter and deal with the non-periodic low frequency noise by using the autocorrelation function, both kinds of noise can be effectively reduced. Figure 6-1 shows the flow chart for the signal processing.

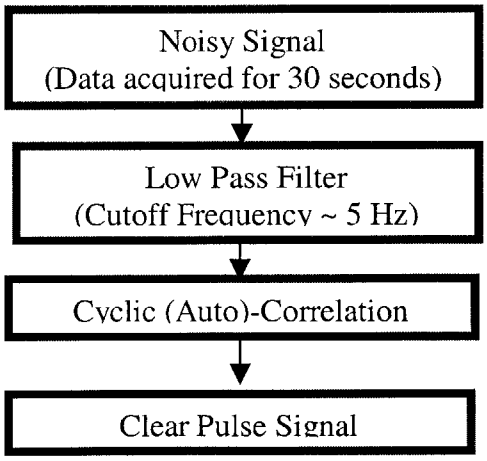

Figure 6-1 Signal Processing Flow Chart

Since a frequency domain analysis is necessary, the continuous stream of the signal detected by the ring sensor is sliced into units of several seconds. (In this case the unit is chosen to be 30 seconds.) This slice of signal passes through a low pass filter. This filter mainly removes the relatively high (higher than 5 Hz) frequency noises, including the 60 Hz frequency component of the room light. This low pass filter is implemented in the device itself in the form of hardware. We can add an extra low pass filter on the software side if necessary.

The low pass filtered signal goes through the autocorrelation function. With this process, most of the non-periodic components are removed from the signal and only the periodic components of relatively low frequency will survive, these most likely being the heartbeat.

Actually, the "windowing" process (the slicing of the stream of signal) is one limiting factor of this signal processing in real time analysis since an abrupt change in the heartbeat cannot be promptly detected. The correlation method works better with a larger window; however, the response delay to a change in heart operation becomes shorter as the size of the window gets shorter. This reveals a kind of trade-off that should be considered in designing the signal processing algorithm.

The autocorrelation function works as a kind of smoothing factor. It compares the multiple waveforms in a signal slice, and derives an average of the waveforms. Due to the averaging effect, the sharp peaks of the waveforms often become blunt and sometimes even disappear after correlation. This is another drawback of this method. The resolution of a signal analysis using the autocorrelation method can be improved to some extent by shortening the length of the window. This ends up being another trade-off.

6.2.2 Theoretical Description of the Autocorrelation Function

The autocorrelation method is an averaging function that appears in the random signal processing area. In this section, a brief explanation of autocorrelation and its application to our ring sensor will be presented.

The time-average of a discrete random signal x[n] is defined as :

$$< x[n] >\equiv \lim_{N\to\infty} \frac{1}{2N+1} \sum_{n\to -N}^{N} x[n] \qquad (6\text{-}1)$$

The autocorrelation function is defined as follows,

$$R_x[k] \equiv < x[n]x[n-k] > = < x[n]x[n+k] > \tag{6-2}$$

The autocorrelation function of a periodic signal with period N is also periodic with period N :

$$\begin{aligned} &if \quad x[n+N] = x[n], \\ &then \quad R_x[k+N] = < x[n]x[n-k-N] > = < x[n]x[n-k] > = R_x[k] \end{aligned} \tag{6-3}$$

For a signal having no periodic component, the autocorrelation function with a relatively large lag k approaches the square of the mean :

$$\lim_{|k|\to\infty} R_x[k] = \mu_x{}^2 \quad if \quad x[n] \ is \ non-periodic \tag{6-4}$$

This means that the autocorrelation function of a non-periodic signal doesn't contain an AC component with a certain value of k of which the absolute value is larger than zero, as long as the sampling frequency is high enough relative to the frequency of the signal. For example, if we sample with 1 kHz, and take data for 30 seconds (the total data point is 30000), the autocorrelation of the non-periodic signal becomes almost constant with a relatively large value of k such as k=1000.

Now let's look at the crosscorrelation function. A crosscorrelation function is defined as :

$$R_{xy}[k] \equiv < x[n]y[n+k] > = < x[n-k]y[n] > \tag{6-5}$$

If x[n] and y[n] are two sinusoidal waves with different frequencies, the crosscorrelation function of those two signals is zero, which means that they are uncorrelated. On the other hand, the crosscorrelation of two sinusoidal waves having the same frequency is a sinusoidal wave at the same frequency.

Let's take two sinusoidal signals with zero means,

$$x[n] = A_x \cos(2\pi f_x n + \phi_x) \tag{6-6a}$$

$$y[n] = A_y \cos(2\pi f_y n + \phi_y) \tag{6-6b}$$

The crosscorrelation function is

$$\begin{aligned} R_{xy}[k] &= < x[n]y[n+k] > \\ &= A_x A_y < \cos(2\pi f_x n + \phi_x)\cos(2\pi f_y (n+k) + \phi_y) > \\ &= \frac{A_x A_y}{2} < \cos(2\pi (f_x + f_y)n + 2\pi f_y k + \phi_x + \phi_x) > \\ &\quad + \frac{A_x A_y}{2} < \cos(2\pi (f_x - f_y)n - 2\pi f_y k + \phi_x - \phi_x) > \end{aligned} \tag{6-7}$$

If $f_x \neq f_y$, both of the terms of Eq.(6-7) are sinusoidal functions of n, so that their means are both zero, and $R_x[k]$ is also zero. If, on the other hand, $f_x = f_y = f$, the second term is a function of k, not n, so that

$$R_{xy}[k] = \frac{A_x A_y}{2} < \cos(2\pi f_y k - \phi_x + \phi_x) > \tag{6-8}$$

which has the same frequency as the original signal eqs.(6-6a) and (6-6b). From this result, we can say that if y[n] is a non-periodic signal (which means the frequency is zero) with a zero mean, the crosscorrelation of a periodic signal x[n] and y[n] becomes zero. If the signal y[n] is non-periodic, but with a mean other than zero, the crosscorrelation function becomes a constant. This means that the crosscorrelation of x[n] and y[n] doesn't have any AC component.

$$if \quad y[n] \ is \ non-periodic, \ R_{xy}[k] = const \tag{6-9}$$

Using this result of Eq.(6-8), we can also get the autocorrelation function of a periodic signal with an arbitrary waveform.

Let x[n] be a periodic signal expressed as a discrete Fourier series :

$$x[n] = \sum_{i=0}^{\infty} A_i \cos(2\pi i \frac{n}{N} + \phi_i) \tag{6-10}$$

From Eq.(6-8), we know that all the different frequency components are uncorrelated with each other. Therefore, we get the following result :

$$R_x[k] = \sum_{i=0}^{\infty} \frac{A_i}{2} \cos(2\pi i \frac{k}{N}) \tag{6-11}$$

Eq.(6-11) shows that the autocorrelation of any periodic function has the same waveform and frequency as the original signal x[n].

The signal received by the ring sensor can be expressed as the following:

$$x[n] = s[n] + d[n] \tag{6-12}$$

where s[n] is the periodic heartbeat signal and d[n] is a non-periodic noise. The autocorrelation function of x[n] is :

$$\begin{aligned} R_x[k] &= < x[n]x[n+k] > = < (s[n] + d[n])(s[n+k] + d[n+k]) > \\ &= < s[n]s[n+k] > + < d[n]s[n+k] > + < s[n]d[n+k] > + < d[n]d[n+k] > \\ &= R_s[k] + R_{sd}[k] + R_{ds}[k] + R_d[k] \end{aligned} \tag{6-13}$$

From Eq.(6-4), we can see that $R_d[k] \approx$ constant; $R_{sd}[k]$ and $R_{ds}[k]$ are also constants according to Eq.(6-9). From Eq.(6-11), $R_s[k]$ contains the waveform and the frequency of the original signal s[n], and this $R_s[k]$ is the only AC component in $R_x[k]$. In the ring sensor application, this means that only the periodic heartbeat signal survives. Non-periodic noises are removed by applying the autocorrelation.

$$R_x[k] = R_s[k] + const \tag{6-14}$$

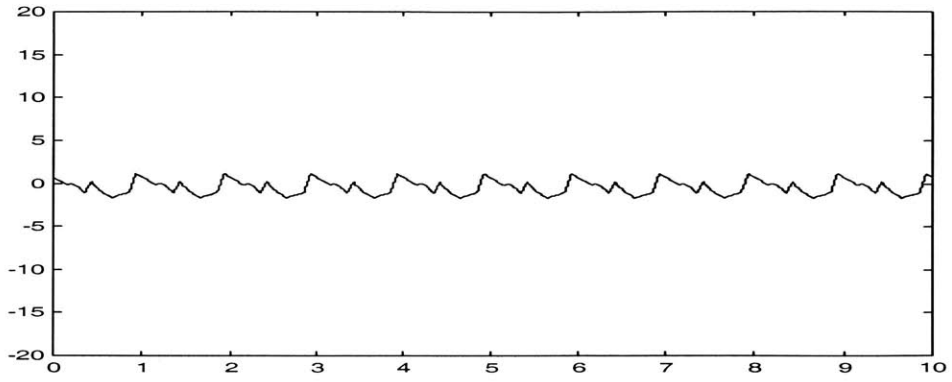

Figure 6-2 Periodic Source with 1 Hz Frequency s[n]

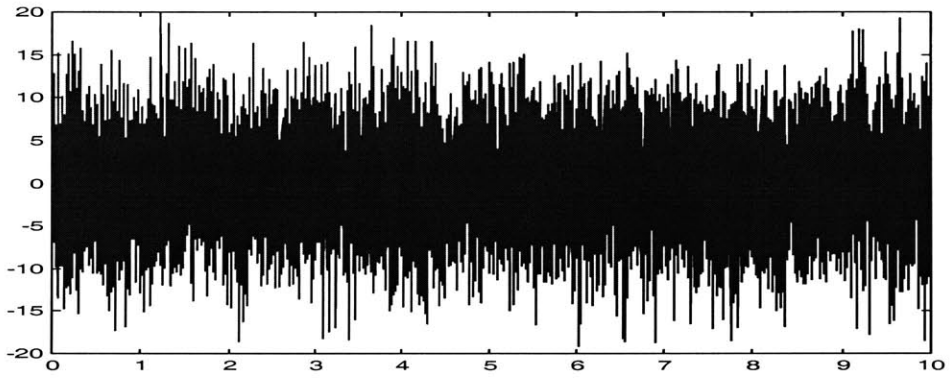

Figure 6-3 Random Noise d[n]

6.3 Numerical Simulation

In order to test the plausibility of the autocorrelation method, an artificially-made periodic signal and a random noise were put into simulation. The periodic signal generated by the software had the frequency of 1 Hz and the signal was sampled at a 1 kHz sampling rate. (This is the s[n] in Eq.(6-12).) The total data acquisition time was 10 seconds. Figure 6-2 shows the periodic input signal.

The random noise was generated with a much higher amplitude to approximate a real situation, which has a low signal-to-noise ratio. This noise is not "white noise." This noise is generated randomly without any consideration of the frequency domain. If we see this noise in the frequency domain, it also shows random behavior. Figure 6-3 shows the random noise generated by a MATLAB function. (This is the d[n] in Eq.(6-12).)

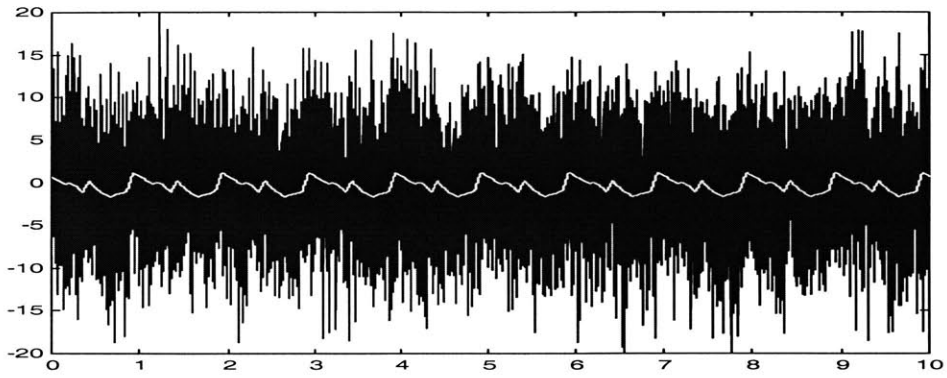

Figure 6-4 Combined Signal x[n]

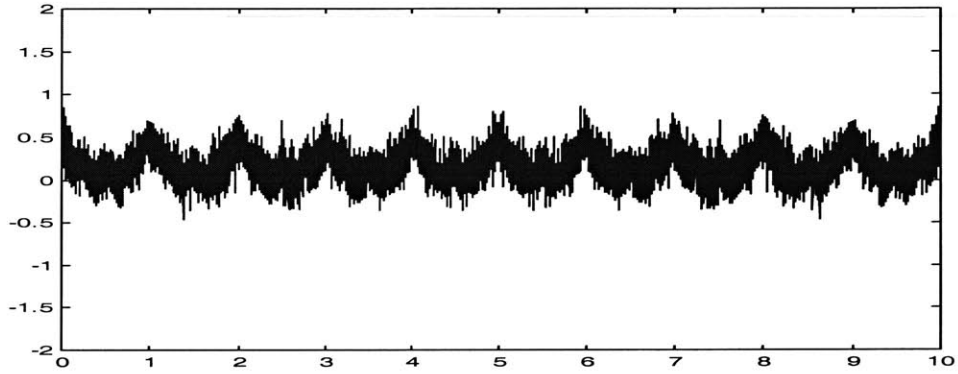

Figure 6-5 Autocorrelation function of x[n]

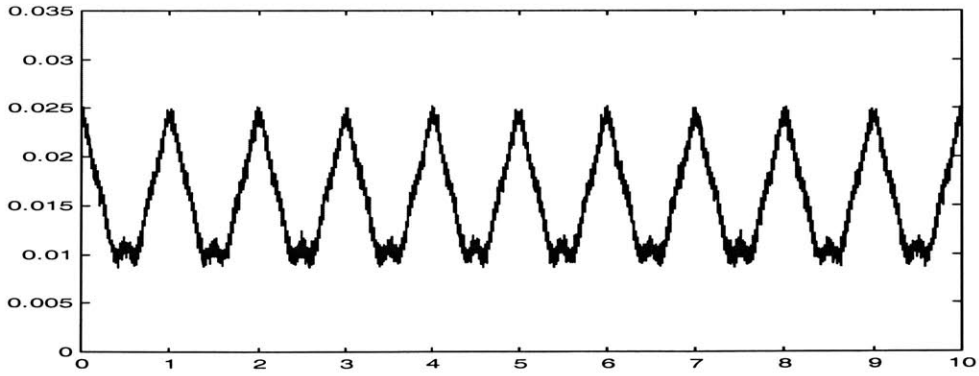

Figure 6-6 Second autocorrelation function of x[n]

Figure 6-4 shows the combined signal of Figure 6-2 and Figure 6-3. This represents the x[n] in Eq.(6-12). The s[n] signal (drawn as a white line for comparison) is completely buried in the noise since the signal to noise ratio is low.

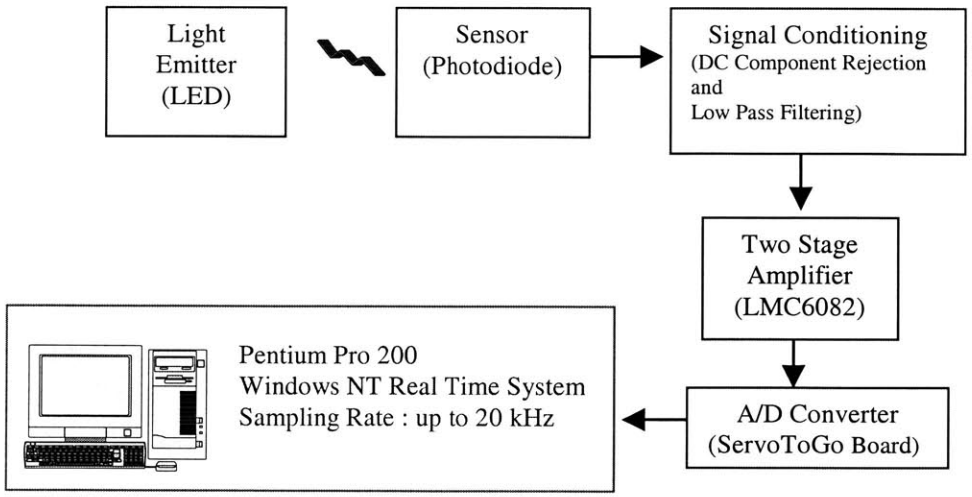

Figure 6-7 Experiment Setup

The autocorrelation function of this combined signal is shown in Figure 6-5. As was expected by Eq.(6-13), we can see that the periodic component of s[n] was recovered, but the recovered signal is still not so clear. If we apply the autocorrelation twice, we get a much better periodic signal. The result of the second autocorrelation function is shown in Figure 6-6.

After applying the autocorrelation, we could recover the frequency of the periodic component exactly. The waveform was not completely recovered due to the low signal-to-noise ratio and the averaging effect, as was stated before. But we could recover the periodic component to some extent. This means that we can at least recover the heart rate of the detected signal from the ring sensor.

6.4 Experiment

6.4.1 Experiment Setup

To support the theoretical result and the numerical simulation, an experiment setup was built. Figure 6-7 shows a schematic diagram of the setup. The signal obtained from the photodiode (detector) goes into a hardware signal processing unit. First, the DC component in the signal is removed, since we only need the oscillating AC part, and a low pass filter is applied to the signal to remove high frequency noise.

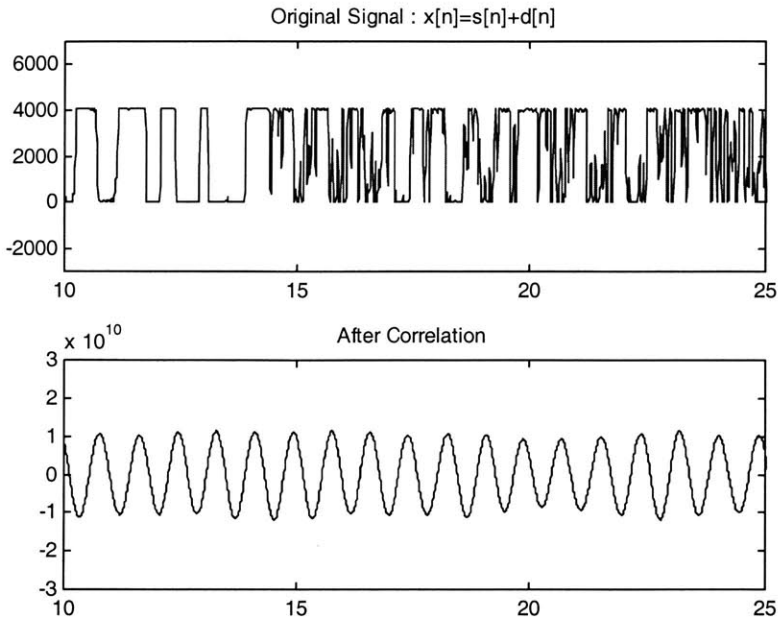

Figure 6-8 Original ring sensor signal and the result after autocorrelation

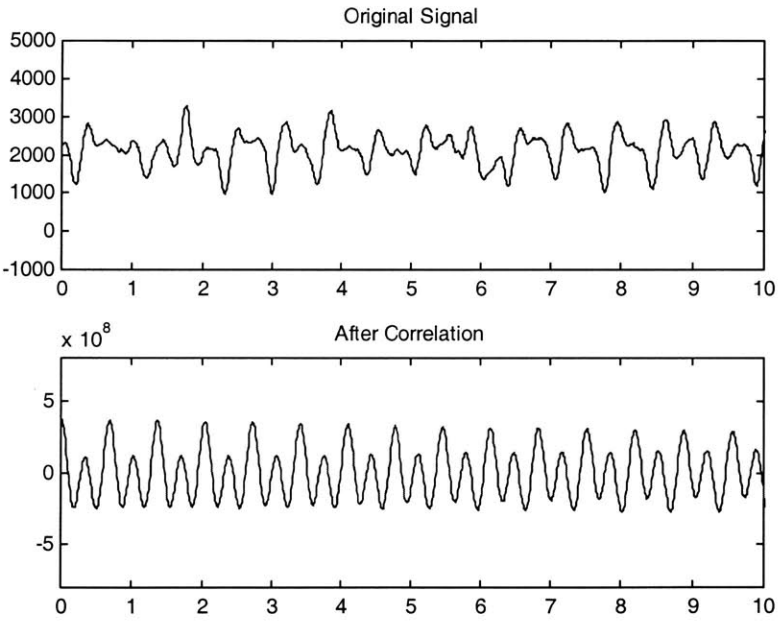

Figure 6-9 Autocorrelation function showing the second peak of the heartbeat

The signal is then amplified by about one thousand times, raising the voltage to around 2~3 volts which is in the detectable range of the A/D converter. The signal can be sampled at a rate of up to 20 kHz by using a custom-built windows NT-based real time data acquisition system. After the data

become ready in the computer memory, they are tempered by software-based signal processing techniques such as autocorrelation.

6.4.2 Experiment Results

The simulation results were also verified by the real experiment results. Figure 6-8 shows the original signal detected by the ring sensor and the signal processed by the autocorrelation technique. The original signal was obtained from the ring sensor when the hand was tightly clenched. As can be seen from the figure, the original signal was seriously distorted and contaminated with noise. The signal even shows a state of bad saturation because of the hand grip. But after the correlation technique was applied, the signal was arranged in a neat shape and the high frequency noise was removed. Although the exact "pulse shape" could not be recovered, it can be seen that the periodic component of the detected signal was reconstructed by the autocorrelation method, which means that we can clearly estimate a pulse rate even in the worst of situations.

This example does not explicitly show the second peak of the heartbeat after autocorrelation since the periodic characteristic of the second peak in the original signal was not apparent and was seriously contaminated by many kinds of noise. The next example shows that even the second peak of the heartbeat can be reconstructed as long as the original signal shows a clear behavior of the second peak. (Figure 6-9)

As we can see in the experiment results, the autocorrelation function method shows a certain limitation in reconstructing the smaller peaks in the waveform. This is mainly due to the averaging effect of correlation. We can better reconstruct the waveform if we use a shorter window for slicing the signal, but this is at the expense of effective noise reduction. If the noise is relatively small, then it is possible to reconstruct the original waveform with a higher resolution. However, in the case of a severely low SNR, we have to stay with getting only the exact pulse rate. In our ring application, in which the main emphasis lies in continuous heartbeat monitoring, the pulse rate itself has great clinical importance.

7. PROTOTYPING AND FABRICATION

7.1 Packaging

Figure 7-1 shows a prototype of the isolating ring sensor. The details of this design are:

- A miniaturized sensor unit is attached to the inner ring whose mass is almost negligible. This sensor unit is a small circuit board (5mm × 5mm × 0.8mm) that contains two light emitting diodes and a photodetector. Since we use point-based light emitting diodes and a subminiature photodetector, this sensor unit weighs only 0.79 grams.
- The main circuit board and batteries, which are heavy and bulky in comparison to the sensor unit, sit on the outer ring. The main circuitry consists of many small elements, most of which are in a surface mount or bare die form. Although the size and weight of the components used are generally small and light, the total mass of this circuit board is not negligible: 3.68 grams. In addition, the button type batteries used for providing power to the circuitry are relatively heavy: 6.31 grams. These components sit on the surface of the outer ring facing outward. The outer ring is made of aluminum; a block of aluminum was machined to a hollow ring as shown in Figure 3-2, and all the parts other than the sensor unit were fixed to the outer ring.
- The inner ring floats inside the outer ring. When a patient wears the ring, both rings are put on the same finger. Since the outer ring covers the inner ring, the external force is born by the outer ring and does not directly act on the inner ring. Although the outer ring may be dislocated due to an external force, the sensor unit on the inner ring will remain stable, since there is no direct mechanical connection between the two rings except for a few thin wires. The two rings are mechanically decoupled.

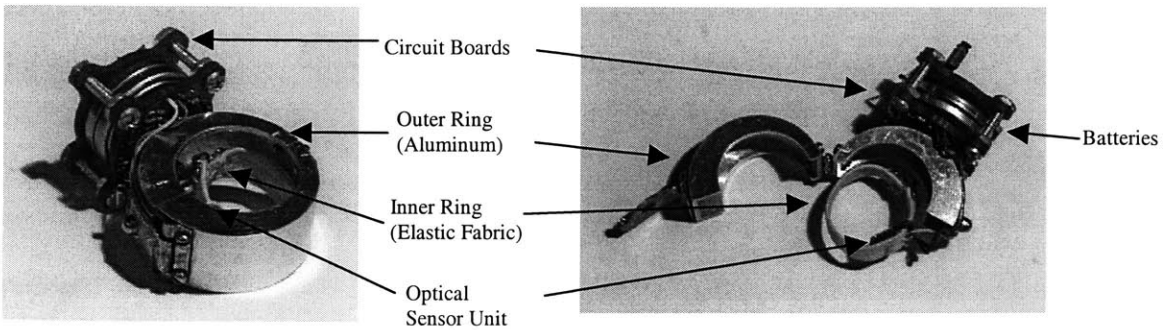

Figure 7-1 Isolating ring sensor designed for motion artifact minimization

7.2 Electronic Component Selection

LEDs and Photodiode

One red LED and two infrared LEDs are used as the light sources. The peak wavelength of the red LED is 660 nm, and that of the infrared LEDs is 940 nm. The photodiode has a peak wavelength of 940 nm and its spectral sensitivity ranges from 500 nm to 1000 nm, which meets our needs. The voltage drop across the red LED is 1.6 V and that of the infrared LEDs is 1.2 V, and the two infrared LEDs are connected in serial. These LEDs are in die form with a size of 0.3mm × 0.3mm.

The First-Stage Amplifier

The slew rate of the first stage amplifier must be high enough to capture the flickering LEDs, while its power consumption must be kept low. We chose an OPA336 surface mount style amplifier from Burr-Brown. This amplifier has a slew rate of 0.03 V/μs and a current consumption of 20 μA.

Signal Conditioner

The signal conditioning part consists of filters and amplifiers. The signal from the first stage amplifier contains a large portion of DC signal, which is cut off by a high-pass filter. The resultant AC signal is on the order of millivolts, needing amplification on the order of 10^3. We used a die-form operational amplifier, MAX407, from Maxim, which consumes an extremely low current of 1.2 μA per amplifier. The slew rate is not an important factor since the frequency of the signal in this stage is less than 10 Hz. The cut-off frequency of the low-pass filter was set at 5 Hz.

CPU

The on-board CPU controls all the operations of the ring sensor, ranging from the sequence control of LED lighting and data acquisition to the conversion of analogue data to digital signals in the RS-232 format for wireless transmission. A PIC16C711 microprocessor from Microchip was selected because of its unique design for low power consumption. It consumes less than 25 μA at the 32 kHz clock frequency in the normal operation mode and almost no power consumption in the sleep mode. This CPU has 4 channels of embedded A/D converter, and 13 channels of digital I/O line. It has 1 KB of EPROM, which is good enough to store all the code needed for computation.

Battery

One critical problem that is practically important is the interference between the RF transmitter and the other parts of the circuit. Since the RF transmitter uses on-off keying, the current drawn to the RF transmitter goes up and down as the output is switched between on and off. This incurs a serious fluctuation in the battery voltage and causes interference with the rest of the circuit, particularly the analog op-amps. To resolve this problem, two separate batteries were used for the prototype ring sensor: one for the RF transmitter alone and the other for the CPU, LEDs, and op-amps. Button-type thin lithium batteries from Duracell were selected. The RF transmitter is powered with a DL2016 battery of 75 mAh rated-capacity and the CPU-LED circuit with a DL2032 battery of 220 mAh rated-capacity. Both batteries have an output voltage of 3 volts.

7.3 The Power-Optimal Clock Frequency

Based on the power budget model obtained in the previous section and the power consumption characteristics of each part selected, the optimal clock frequency for minimizing the overall power consumption will be obtained in this section. The power consumption parameters associated with the red and infrared LEDs are:

$$C_r=2.3\times10^{-3}\,(Ampere), \qquad C_i=0.5\times10^{-3}(Ampere)$$

Note that the unit of these parameters is the Ampere rather than the Watt in order to be consistent with the battery capacity unit of Ampere-hour. The CPU power consumption model, Eq.(4-2), was identified through experiment. The coefficients involved in the model, a and b, are given in Amperes by

$$a=1.993\times10^{-9}\ (Ampere/Hz), \quad b=6.553\times10^{-6}\ (Ampere)$$

For the prototype ring sensor, a sample-and-hold frequency of $f = 1{,}000\ Hz$ was used. The number of sample points that the RF transmitter had to transmit per unit time was set to be $n = 60$. The current consumption of the transmitter circuit was identified as:

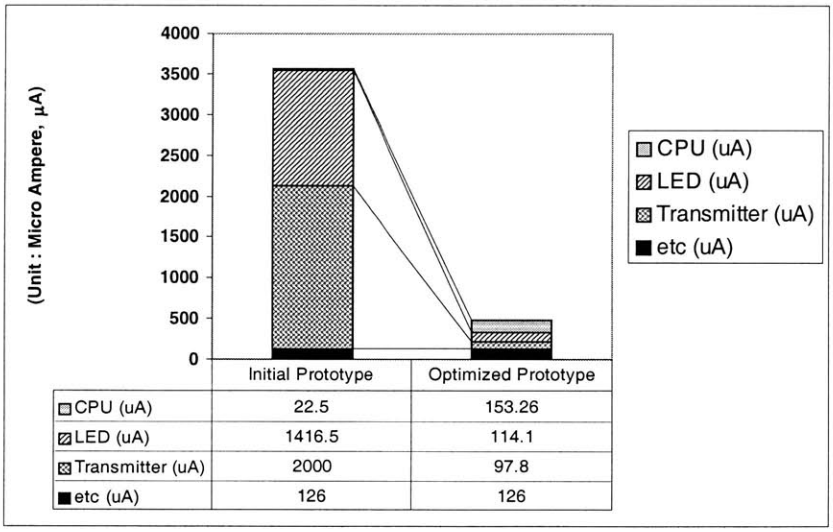

	Initial Prototype	Optimized Prototype
CPU (uA)	22.5	153.26
LED (uA)	1416.5	114.1
Transmitter (uA)	2000	97.8
etc (uA)	126	126

Figure 7-2 Comparison of Power Budget

$$C_t = 4.0 \times 10^{-3} \ (Ampere)$$

Substituting these parameters into Eq.(4-6) yields the optimal clock frequency for the CPU:

$$q^* = 73.61 \ kHz$$

And the minimized current consumption is given by

$$P_T(q^*) = 0.365 \ mA$$

The other electronic components of the ring sensor include multiple op-amps, switches, sample-and-hold, and filters. The total current consumption of these components was found to be *0.126 mA*. Therefore, the optimal total current consumption of the ring sensor is *0.491 mA*, or *1.473 mW* with *3V* batteries.

Figure 7-2 shows the comparison of the power optimal design with the initial non-optimal design. The power optimal design has reduced the power consumption to *1/7* of the original design, where $r = 0.5$, $d = 600$ bps, and $q = 8{,}000$ Hz. In particular, the power consumption of the RF transmitter has decreased to *1/20*, while that of LEDs has decreased to *1/12*. Based on these data, the battery life, i.e. the length of continuous measurement without changing the batteries, can be obtained. In the

prototype ring sensor, two separate batteries are used. The RF transmitter consumes 0.098 mA in the optimal design. Therefore the lithium battery of *75 mAh* capacity can last for 31.9 days. On the other hand, the CPU-LED circuit consumes 0.393 mA, and can run continuously for 23.3 days with a lithium battery of *220 mAh.* If continuous measurement is not required, but some intermittent measurement suffices, the battery life can be extended to a period of several months to a year.

7.4 Software Design

7.4.1 Software for the Microprocessor on the Ring Side

An assembly program has been loaded in the microprocessor on the ring sensor. The first process of the code is the initialization of the CPU. Then it triggers the A/D conversion of a channel. During the A/D conversion delay, it retrieves a number from another A/D channel. Then it transmits the number in RS-232 format. To match the timing of a certain baud rate, we counted the number of instructions executed to send one bit, and calculated the time for a one-bit transmission. Each 8-bit number is sent with a start bit and a stop bit, which complete the RS-232 protocol. This process is done in both channels in turns.

7.4.2 Software for the Host Computer with Artifact Detection

An RF receiver receives transmitted signals in RS-232 form and transmits the data to the home PC through a serial port. The software on the host computer is run in a Windows 95 or Windows NT environment. It is programmed using Microsoft Visual C++ 5.0, and uses the standard serial communication programming technique. It is natural that the program be in the standard Win32 program format, and this format has to start with the initialization of the windows and the variables.

Apart from the standard windows programming routines, most of the program is dedicated to detecting faulty signals and removing those noise signals from the clean heartbeat signal. The multi-threading routines check the serial port continuously to find out if any data have arrived. As soon as some data arrive at the serial port, the program counts the number of red LED signal and the number of infrared signals. If the signal transmission has been done correctly, the two numbers will be almost exactly the same. If this is not the case, then there has been some problem with the signal transmission. In this case, the program considers the received signals as noise and ignores them. If the number of red LED signals and that of the infra-red are more or less the same, then the program

checks the frequency component of the received data. If the data includes any strange high frequency components, the program thinks that these data have been contaminated by motion artifact or ambient light influence, and discards all the data as it has been severely contaminated by noise. If the received signal passes through these filtering processes, the program accepts the data as valid and displays them on the screen. The program also measures the peak-to-peak distance at this stage and calculates the pulse rate. The same process is done continuously whenever any data is detected available at the serial port.

8. MINIATURIZATION

8.1 Background

A finger ring sensor for 24-hour patient monitoring was developed. However, the size of the first prototype, as shown in Figure 8-1, was too large to be of use in real life. For the ring sensor to be practical, it had to be reduced to a size no larger than a college ring. If the various electronic components, including the battery, can be packed within this size constraint, people will simply wear it, be incognizant of its presence, and they may even take a shower while wearing it. The first prototype was also too heavy and unwieldy, a factor responsible for the majority of the motion artifact observed. Therefore, the final ring must be compact and light enough so that the person who wears it does not feel its presence. In the initial effort, we plan to consolidate all the circuit elements on to a small, multi-layer printed circuit board (Figure 8-2).

The ultimate and most ideal way to reduce size is to design a mixed signal ASIC chip so that all the circuitry can be condensed and packed up in one masked-chip. Unfortunately, this approach is too costly; it requires a long lead-time, and was found to be impractical at the present stage of development. Since we cannot go for an ASIC at this time, we have no alternative but to use commercially available discrete electronic components for the ring sensor construction.

As is well known, there are certain limits to the size of electrical components. The conventional integrated circuit, for example, is too large to be considered for ring construction if it is used in its regular plastic package. However, a substantial size reduction can be achieved by putting IC chips, in die form, directly on a circuit board without the plastic package. It would also be advantageous to use discrete resistors and capacitors of the smallest size available. Since soldering is obviously difficult with these components, a thermal-sonic wire-bonding machine using 0.001" gold wire is used to connect the components to the circuit board.

Besides size reduction, power consumption minimization is another obstacle. As the size of the ring is reduced, it becomes impractical to put relatively large batteries on the ring sensor. As a result, due to the small batteries, the operating life of the ring is substantially reduced, and the power saving strategy becomes far more critical. Nevertheless, we have devised a number of important

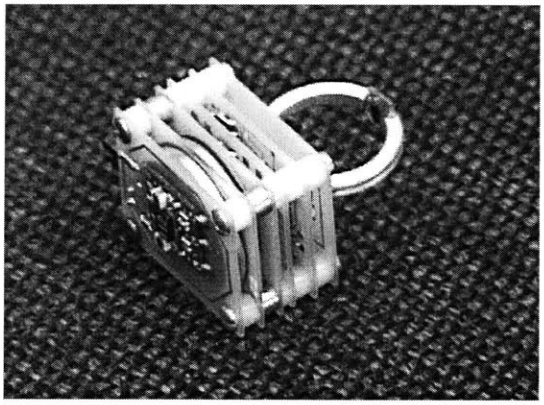

Figure 8-1 First Prototype Ring Sensor

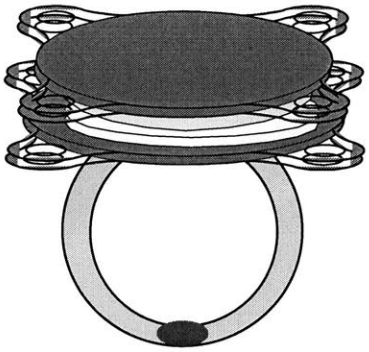

Figure 8-2 Ring Sensor with One or Two Circuit Boards

power reduction schemes which successfully extend the useful life of these small batteries: adopting faster LEDs, a higher CPU clock speed, and a faster transistor for the RF transmission circuit.

8.2 Issues of Miniaturization

8.2.1 How do we reduce size?

The components we usually use have their own limits. For example, the size of an IC chip is characterized by its package. If we stick to these kind of normal components it is impossible to reduce the size of the ring to the extent desired.

Despite its packaged size, the functional core of an IC chip is actually very small. This core part is called a "die" and its size is far smaller than the package itself. The reason why the die is embedded in a large plastic package is to make soldering and handling easier. Although difficult, we can use

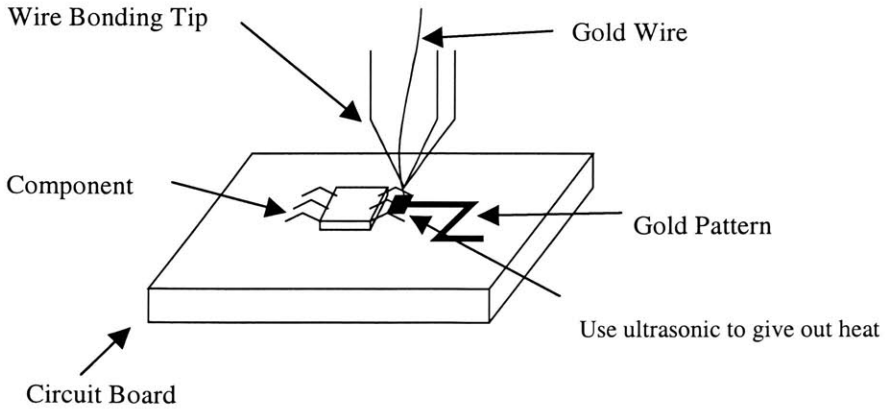

Figure 8-3 Wire Bonding Machine

the IC chips in their "die" form rather than in their plastic package, thereby resulting in a ring construction of minimal size. Since these chips in die form cannot be connected with normal soldering iron, we need to use equipment called the "wire-bonding machine." This machine connects components with very thin gold wire. Basically it works like an extremely tiny welding machine which melts gold with ultrasonic energy at an elevated temperature of 150 degrees C. In the ring sensor, the inter-connections between various active and passive components are manually done under a microscope with the aid of a mechanical mouse for the positioning of the circuit substrate relative to the welding head. A schematic diagram depicting the operation of this machine is shown in Figure 8-3.

For passive components such as resistors and capacitors, we can purchase them in very small thin or thick film style which are designed for wire bonding. These components are very small compared to the conventional ones we normally use (Figure 8-4). The pads (called "termination") which replace

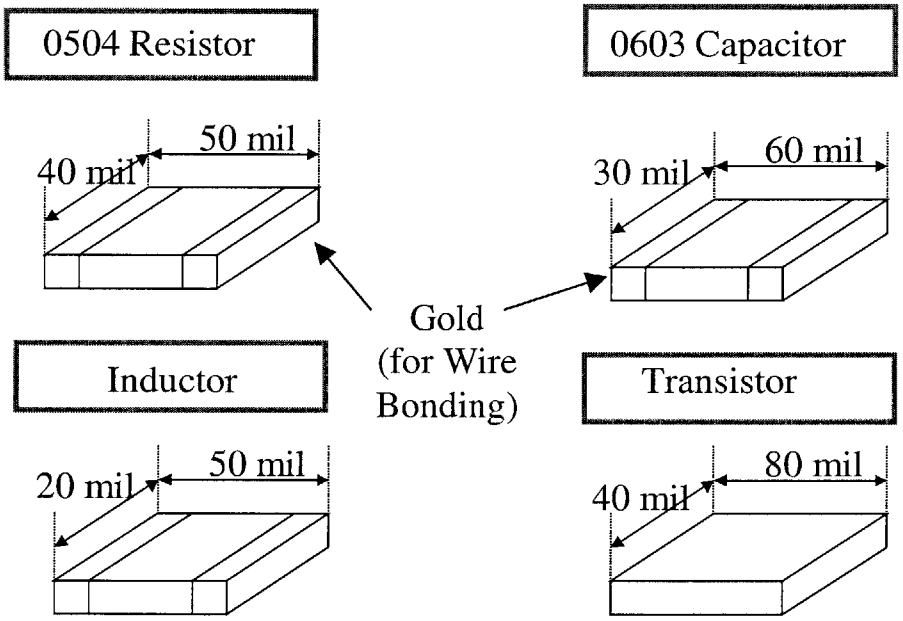

Figure 8-4 Dimensions of Components

the leads of conventional components are made of gold or aluminum when they are designed for wire bonding. There are certain kinds of components with their pads made of nickel or silver; they are not designed for wire bonding, but rather for surface mount assembly. If we have to use this type of component because of practical considerations dictated by commercial availability, we can

not resort to wire bonding. In that particular case, we would use conducting epoxy to do the connections on the circuit board.

8.2.2 What kind of circuit boards will we use?

There are several choices for the circuit board material, but ceramic substrates are what is commonly used. Ceramic substrate is rigid, strong, and it can withstand the high temperature encountered in the thermal sonic wire bonding operation. More importantly, all the resistors used in our design can be deposited as film resistors on the substrate without actually taking up any physical space because these thin film-type resistors can be over-coated with a thin layer of insulating glazing material so that other components, such as capacitors, transistors and IC dies, can be situated on top of the underlying resistors. Since the film resistors are deposited at the factory through screen printing, our work load is substantially reduced during fabrication. Despite the advantage in size and work load reduction, ceramic substrate has not been used in our current development due to its high cost and a prohibitively long lead time.

One practical solution lies in the use of conventional G-10 epoxy printed circuit board material. This approach offers some unique advantages. One can make multiple circuit patterns on multiple layers in the same board. The benefit is that the space taken up by the inter-connecting circuit tracings is greatly reduced, and we can make the circuit board, and therefore the ring, smaller. In addition, the fabrication cost of printed circuit boards is less than that of ceramic substrates, and the lead time is much shorter(usually only a couple of days). Of course, in this case we cannot enjoy the benefit of a ceramic circuit board which comes with the film resistors already put on by the factory.

8.2.3 How do we reduce the power consumption from the viewpoint of hardware?

Power saving is of critical concern in a miniaturized ring sensor application since, inevitably, tiny batteries must be chosen in place of those used in the first prototype. In the first place, power consumption can be reduced by shortening the duty rate of the LED blinking cycle. To implement this, we need a photodiode which can respond to a short duration light pulse much faster. For this reason, we need to use a PIN photodiode rather than an ordinary PN photodiode. The PIN type photodiode usually has a 10 times faster response time than the PN photodiode. To reduce the on

time of the LEDs, it is necessary to turn the LEDs on and off faster. For this, we need a higher CPU clock speed.

For the telemetry transmission, we can save power by increasing the baud rate of the RS-232 protocol. Since the number of bits to be transmitted per unit time is fixed, we can reduce the time duration when the transmitter is turned on by making each bit shorter through the use of a higher baud rate. For this to be successful, the rise and fall times of the transmitter need to be reduced, and this can be achieved by adopting a faster transistor for the RF transmitter circuit.

In conclusion, in order to save power, we need to adopt a faster photodiode, a higher CPU clock, and a faster transistor for the transmitter.

8.3 Process of Fabrication

8.3.1 Finalize the circuit and collect the necessary components.

Since we have already built a prototype, we have a finalized circuit diagram. The circuit we will use to build a miniaturized ring sensor is almost the same as that of the prototype ring except for a few changes. The changes were made largely due to power saving considerations. First, the number of red LEDs has been reduced from two to one in the prototype. This will save about 500 microamperes. Although we have reduced the number of LEDs, we have already verified that it is still sufficient for the operation. The crystal for the CPU clock was changed to 120 kHz in order to reduce the duty rate of the LEDs.

Ambient light elimination was implemented from the software side. The circuit is equipped with two channels of signal conditioners. To activate ambient light elimination, we just turn off one of the two LED channels permanently. In other words, we turn on the detector when no light source is turned on. The signal coming to the detector at this moment will be purely from ambient light sources. We subtract this from the value measured when one of the LEDs is on, so that we get a value in which the influence of ambient light has been removed.

About the components, all the IC chips used in this circuit were in die form. The sizes of these die form chips range from about 50 by 50 mil to more than 100 by 100 mil, which are still much smaller than the packaged versions for surface mounting.

8.3.2 Design a conducting pattern to be put on the ceramic substrate or the printed circuit board.

The next step is to design the circuit pattern of the board. This is the most time consuming step, and it takes a lot of brain power. First, we measure the dimensions of all the components, and determine the positions of the components on the board. To make the circuit board as small as possible, the spaces between components must be minimized without breaking the design guidelines.

8.3.3 Make the circuit board using gold as the conducting material

As mentioned earlier, we can make the circuit board out of ceramic material or use a conventional printed circuit board. For the present, we have adopted the ordinary printed circuit board in order to reduce the lead time. As a result, we must install all of the resistors manually, which not only takes more time but also increases the possibility of mistakes.

8.3.4 Put the components on the board and make connections

The ceramic substrate is designed basically for the wire bonding technique. In the case that the components are not designed for wire bonding (that is, the terminations are not made of gold or aluminum), we use conducting epoxy to connect the terminations to the gold pattern on the board. The wire bonding must be done very carefully because the gold wire breaks extremely easily, and it

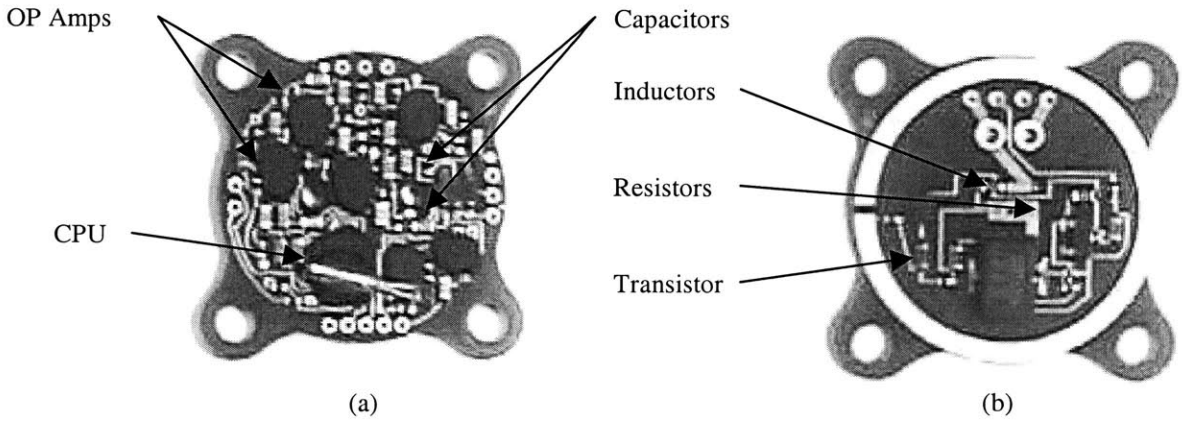

Figure 8-5 Pictures of the miniaturized circuit boards
(a) CPU and Signal processing board
(b) Transmitter board

is hard to get rid of the broken wire and do new bonding. Even after finishing the bonding, the wire bonded components must be gently taken care of. To prevent the gold wire from being broken, it is recommended to put non-conducting epoxy on the bond and harden it with heat, so that the wire is shielded by the epoxy. A picture of the complete circuit board for the miniaturized ring is shown in Figure 8-5.

8.3.5 Do external wirings and debugging

After we finish wiring the board, we have to do some external wiring. Since the large components such as batteries, oscillators and switches are not bonded on the board, they have to be connected to the circuit by external wires. In addition, there is another small circuit board for the LEDs and the photodiode. This small board will be glued on the opposite side of ring from the main circuit board. This small board must be connected to the main board by thin ordinary wire. If we want to attach external antenna, this must be wired, too.

The last step is debugging. It would be almost a miracle if the entire circuit worked immediately after finishing the fabrication, especially given the kind of small device it is. Most of all, the gold wire is very liable to break, as was mentioned already. We must check all the gold wire bonding to make sure it is not broken. If any kind of soldering has been done, we must check to make sure it has been done completely. Another important check point is the components themselves. The die form chips are very susceptible to electrostatics, and this must be checked carefully in the case that the ring doesn't function. The picture of the complete miniaturized ring sensor is shown in Figure 8-6.

8.3.6 Software – In circuit Programming

The CPU used in the present miniaturized ring sensor was designed to allow in-circuit programming. We can erase the assembly codes in the CPU by exposing the EPROM portion of the CPU to an ultraviolet light source from a standard EPROM eraser. After the CPU memory becomes blank, it can then be reprogrammed by connecting five wires from the board to the corresponding pins of an EPROM writer. This useful feature allows the ring sensor to become totally re-programmable. The operating software for the ring sensor can be upgraded whenever an improved version of the software becomes available.

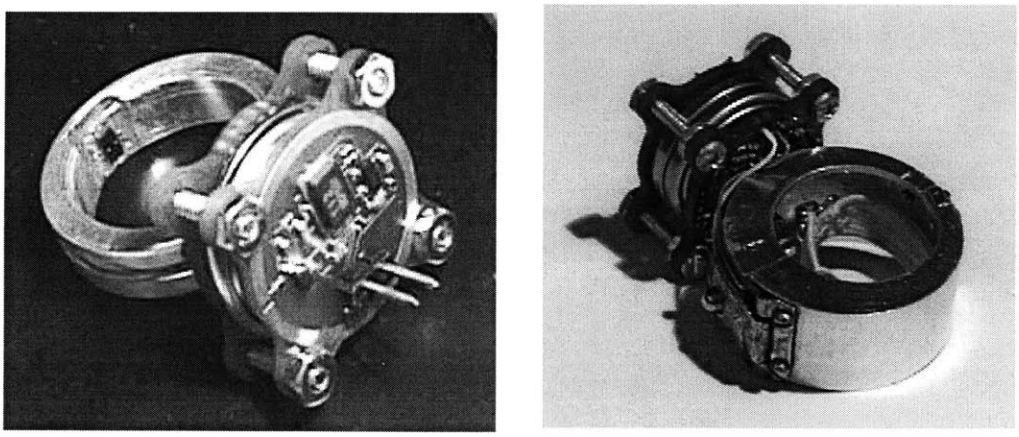

(a) (b)

Figure 8-6 Miniaturized ring sensors
(a) Single ring configuration
(b) Isolating ring sensor

9. VERIFICATION AND BENCHMARKING

The prototype ring sensor will now be evaluated experimentally. There are several issues that need experimental verification and evaluation.

9.1 Software-based Artifact Detection

To establish the validity of this instrumentation system, two kinds of experiments were conducted. The first experiment was designed to test how well this system detects motion artifact. After the signal from the ring sensor becomes stabilized, the wearer shakes his hand so that the signal becomes distorted due to the motion artifact. Figure 9-1(a) shows the actual signal received at the host computer and Figure 9-1(b) shows the data displayed on the screen. As the signal began to be contaminated by the motion artifact from t=12 (sec), the software on the host computer detected a high frequency noise as well as a saturation of the signal to conclude that this was not a valid signal, and ignored the received signal and displayed just a flat line. Figure 9-2 shows the next

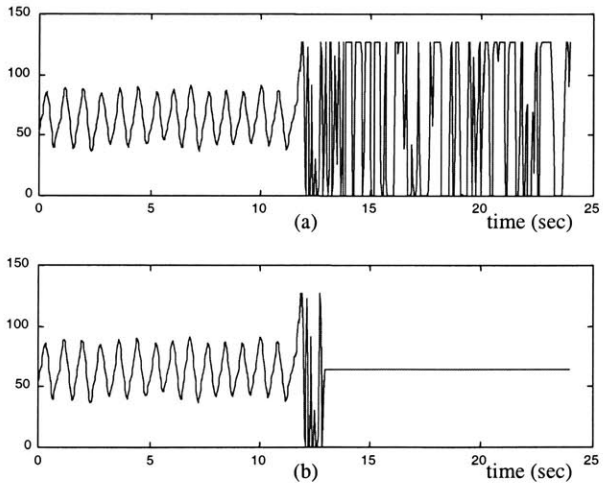

Figure 9-1 Signal contaminated by motion artifact

(a) Actual signal received by the host computer from the ring sensor. The person began to shake his hand from t=12 (sec).

(b) Signal displayed on the screen. The host computer detected the motion artifact and ignored the signal, putting only a flat line after t=12 (sec).

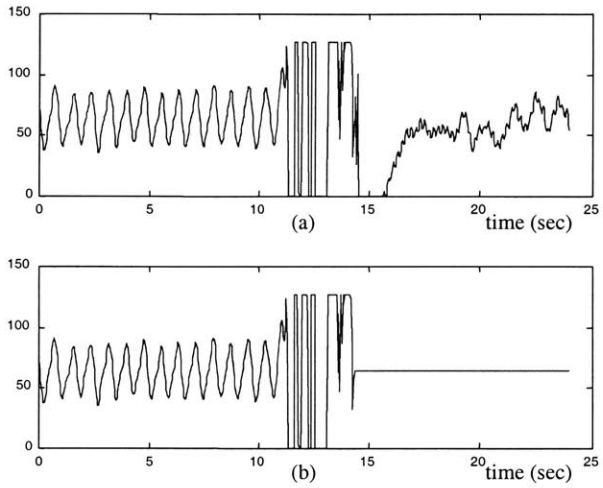

Figure 9-2 Signal contaminated by ambient light influence.
(a) Actual signal received by the host computer. The person took off the ring sensor at t=11 (sec). After this point the signal is purely the noise from ambient light.
(b) The host computer detected high frequency noise from the ambient light, and displayed just a flat line after the detection.

experiment which tested the detection of noise from an ambient light source. At around t=11 (sec), the person took off the ring and put it on the table. Naturally, the signal after this point would not be a valid signal, and only noise from the ambient light would register. Figure 9-2(a) shows the actual data received by the host computer. The software detected the high frequency noise but no saturation. Therefore, it concluded that this signal was not the valid signal. Figure 9-2(b) shows the actual display on the screen as a flat line after the person took off the ring, which indicates that the system was not confused by the ambient light source and could clearly discriminate this noise from the valid signal.

9.2 Adjustment of Inner Ring Tension and Contact Pressure

In the isolating ring structure, the inner ring must hold the sensor unit securely and stably with an appropriate pressure against the finger skin. It is known that pressurizing the tissue increases the pulsation amplitude of the blood vessels and thereby provides a better signal to noise ratio. However, as the contact pressure increases, the possibility of necrosis and blood occlusion also increases. As mentioned previously, the pressure with which the sensor unit is attached to the skin must be tuned to a proper level by making a trade-off between these two conflicting requirements.

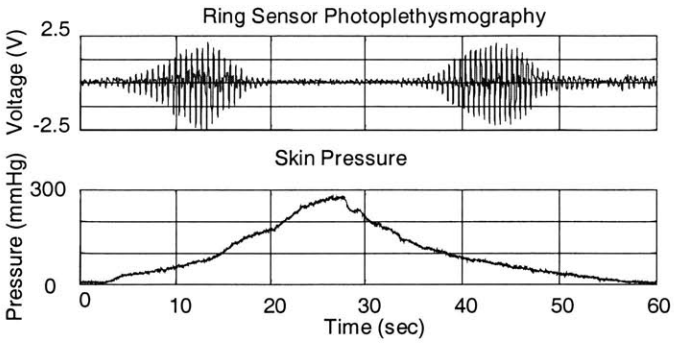

Figure 9-3 Experiment of pulsation amplitude and skin contact pressure

Figure 9-3 shows the experiments concerning contact pressure vs. pulsation amplitude. The sensor unit of the inner ring was placed near a digital artery in order to obtain a large pulsation signal. The subject was a 29 year old healthy male. A micro pressure gauge was attached to the inner ring to measure the pressure with which the sensor unit was placed against the finger skin. The pressure was gradually increased to 250 mmHg, and then gradually decreased. At first, the pulsation amplitude measured by the ring sensor changed in accordance with the contact pressure. It increased until the contact pressure reached the 100 mmHg level, and then decreased. At around 160 mmHg, the blood vessels completely collapsed and the pulsation disappeared. While a relatively high pressure, of around 100 mmHg, is needed to get the maximum amplitude of photoplethysmography, this level of pressure cannot be used since it will completely block the venous return, and the finger tissue will eventually die due to the lack of oxygen. Therefore, it is recommended that the inner ring be designed so that it applies a relatively low pressure, of around 10 mmHg, to the finger.

The inner ring must apply this pressure and maintain the desired level regardless of any disturbances. The thickness of the finger base, however, varies for several reasons. The inner ring must therefore have the compliance to maintain the same pressure in the face of variation in the finger conditions. To this end, a polyester braided elastic band (70% polyester, 30% rubber, from Rhode Island Textile Company) was used for the prototype inner ring. This has been used for underwear in the apparel industry, and proven to be comfortable to wear. This material has a unique nonlinear elasticity: the spring constant is high for small strains, while it becomes very low beyond a certain limit. Therefore, it allows the inner ring to keep the tension almost constant despite a wide range of finger diameter changes.

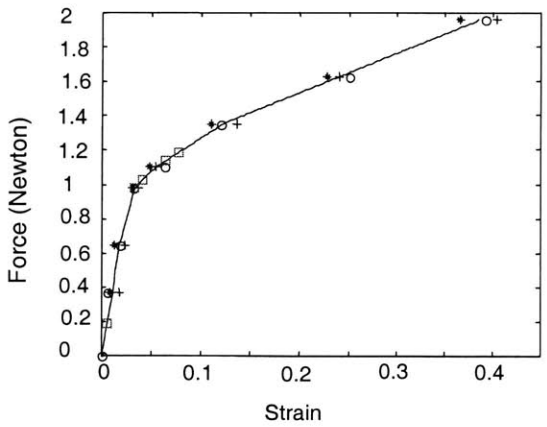

Figure 9-4 Experiment of tension-strain characteristics of inner ring band

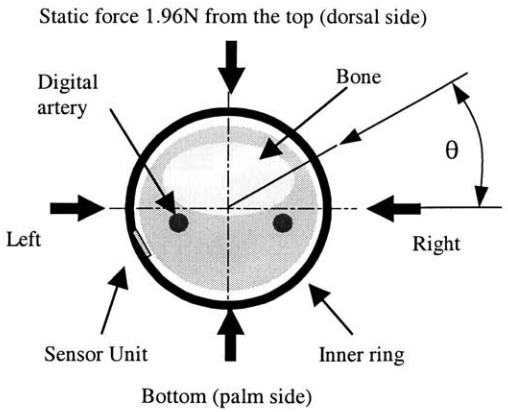

Figure 9-5 Static force experiment

Figure 9-4 shows the experiment on the tension-strain characteristics of the polyester braided elastic band. Note that the slope is steep up to 4% of the strain, i.e. a high Young's modulus. Beyond this limit, the slope lowers to 1/15 of the initial steep slope. Therefore, in this range of large strain, the tension of the inner ring does not vary much, even though the finger diameter is varying. In other words, the sensitivity of the inner ring tension to the finger diameter change is very low. The pressure applied to the skin surface is given by

$$P = \frac{2T}{Dw} \tag{9-1}$$

where P is the contact pressure, T the tension, D the diameter of the elastic band, and w the width of the inner ring, i.e. the elastic band. Combining the tension-strain characteristics in Figure 9-4 and the above equation, the contact pressure can be obtained based on the unsprung length of the inner ring belt and the finger diameter. This calculated contact pressure showed good agreement with actual measurements obtained by using the micro pressure gauge.

9.3 Comparison between the Isolating Ring and a Non-Isolating Ring

To demonstrate the effectiveness of the new isolating ring sensor, several tests were conducted. First, a force was applied to the outer ring from various directions (see Figure 9-5), and the pulse waveforms were measured with the isolating ring sensor, and these were compared with the

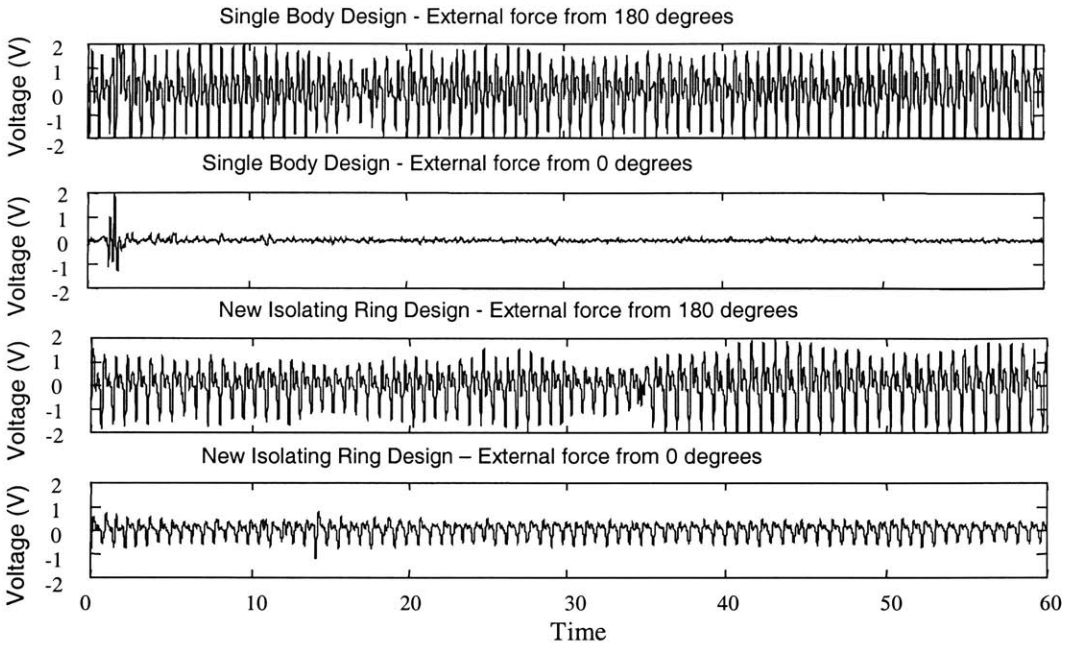

Figure 9-6 Comparison between the ring sensor of the single body design and the isolating ring sensor under external static force.

measurements of the conventional single body ring sensor. Figure 9-6 shows the resultant waveforms taken from the same 29 year old healthy male. The top two waveforms captured by the single body ring sensor show a significant influence from the external load. When the force is applied from the direction of $\theta = 0$ degree, i.e. the opposite side of the optical sensor unit, the signal was totally destroyed due to an air gap created between the sensor unit and the skin. In this case, the optical sensor was open to the air and strong ambient light dominated the measurement. The isolating ring sensor, on the other hand, shows stable measurements despite the external loads, as shown by the bottom two waveforms in the figure. The sensitivity to external loads is an order-of-magnitude lower with respect to the amplitude of the detected pulse, than the sensitivity of the single body ring sensor.

Figure 9-7 shows experiments of acceleration disturbance. Pulse waveforms were recorded while the finger was shaken. As indicated along the horizontal axis, the finger was shaken for 10 seconds and kept stationary for the following 10 seconds. The process was repeated for different accelerations. The top two waveforms were taken by the single body ring sensor under vertical ($\theta = 90$ degrees) and horizontal ($\theta = 0$ degree) accelerations, respectively. Note that the waveforms are very susceptive to acceleration. The bottom two waveforms captured by the isolating ring sensor

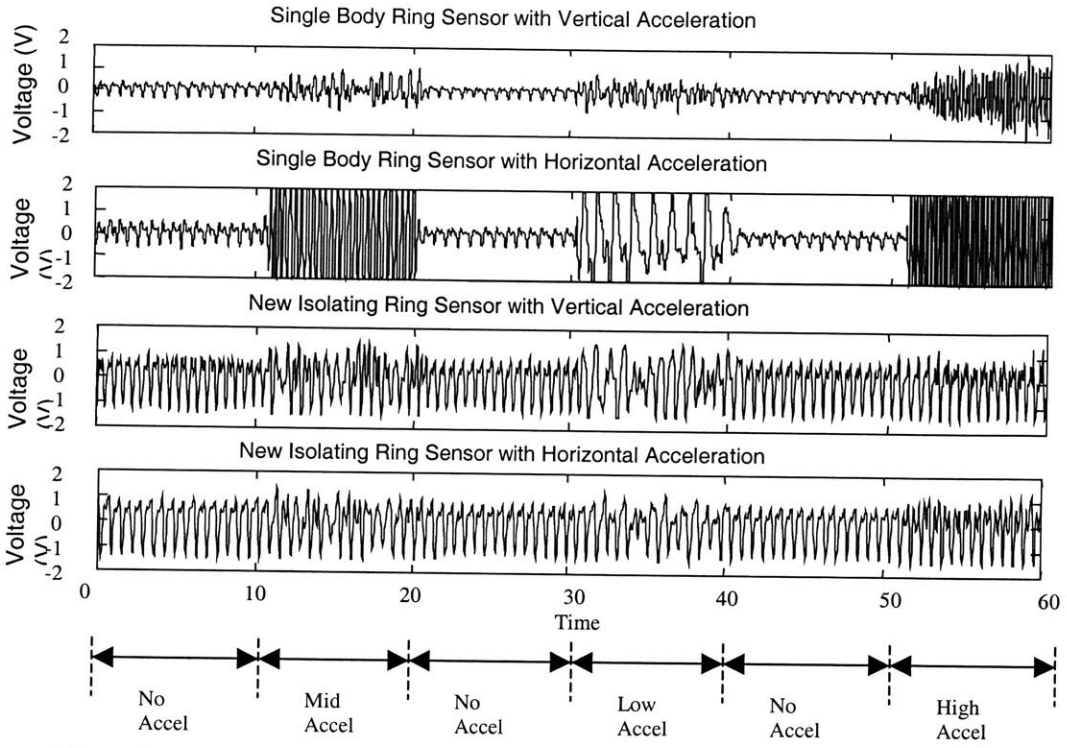

Figure 9-7 Comparison between the ring sensor of the single body design and the isolating ring sensor under acceleration.

show a much lower sensitivity. Even under high acceleration, the isolating ring sensor can correctly capture the basic pulse frequency.

9.4 Benchmarking

The new ring sensor was benchmarked with other FDA-approved devices. An electrocardiogram (EKG) from AD Instruments Pty, Ltd. (NSW, Australia) and a standard fingertip photoplethysmograph from IBS Corp. (MA, USA, FDA-approved) were used for benchmarking. The three devices were attached to a subject at the same time, and data were recorded simultaneously. The fingertip PPG was attached to the tip of the middle finger of the right hand, while the ring sensor was at the base of the middle finger of the left hand. The EKG probes were attached to the standard three points of the body.

Two benchmarking tests were conducted. First, the FFT power spectrum of the ring sensor waveform was compared with those of the EKG and the fingertip PPG. Second, the heart rate obtained from the ring sensor signal was compared with those obtained from EKG and the fingertip

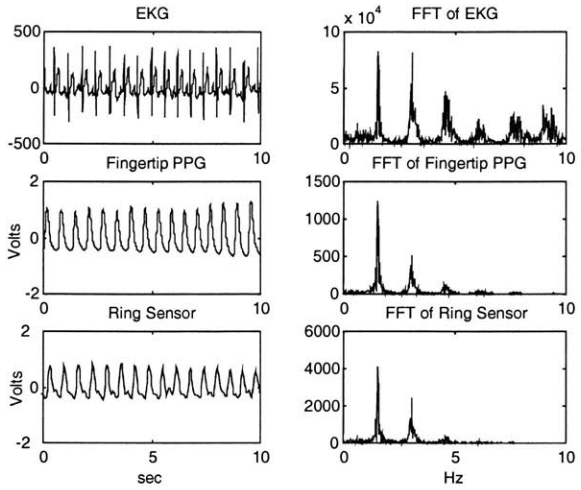

Figure 9-8 No external static force with contact pressure of 75 mmHg. "Fingertip PPG" is the photoplethysmograph at the fingertip using the FDA-approved device (IBS Corp)

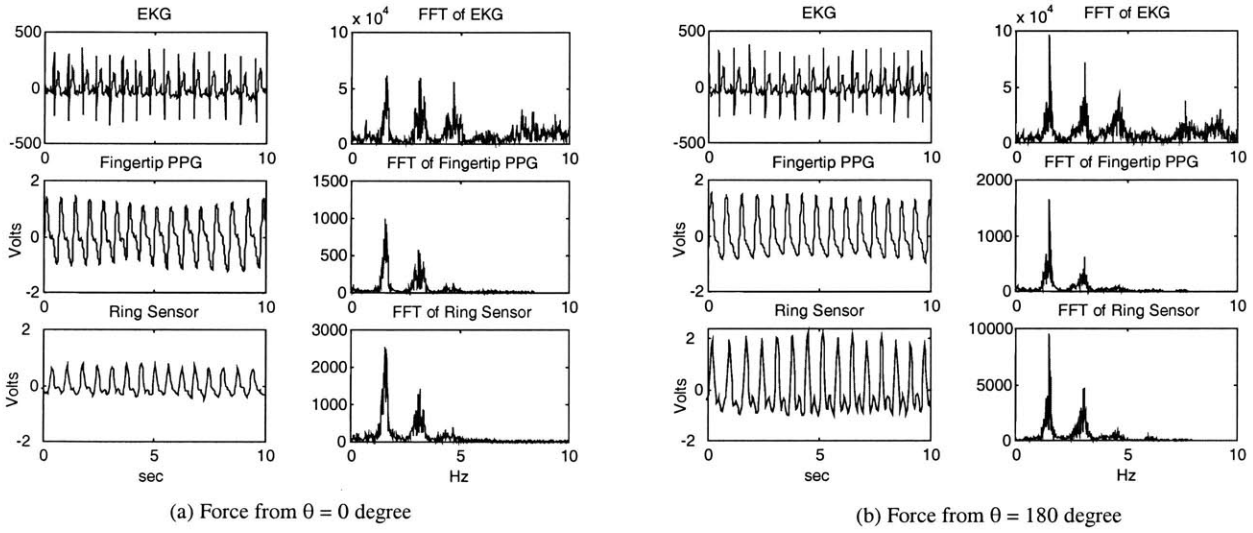

(a) Force from θ = 0 degree

(b) Force from θ = 180 degree

Figure 9-9 Static force experiment with 75 mmHg contact pressure. "Fingertip PPG" is the photoplethysmograph at the fingertip using the FDA-approved device (IBS Corp)

PPG. Both benchmarking tests were repeated for different conditions with respect to external loads and contact pressure.

Waveform Power Spectrum

Figure 9-8 shows the waveforms of the three devices recorded simultaneously, and also their FFT power spectra. The subject was the same 29 year old healthy male. The FFT power spectra were computed for the waveform data recorded for 10 seconds, i.e. approximately 16 pulses. The first peak frequencies of the three spectra are exactly the same, *1.50 Hz*, while the second peak, of

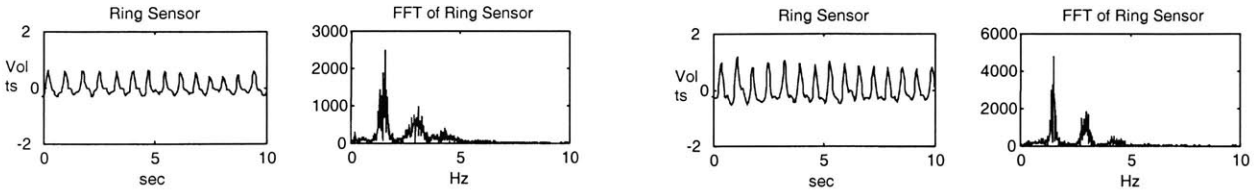

(a) Force from θ = 0 degree

(b) Force from θ = 180 degree

Figure 9-10 Static force experiment with 11 mmHg contact pressure.

around *3 Hz*, is within *1.6* percent of variation. There is no significant difference between the fingertip PPG and the ring sensor power spectra.

The ring sensor must work despite interference due to contact with an environment surface, as discussed previously. To verify that the ring sensor can function properly even under static loads, the benchmarking test was repeated with external forces applied to the ring body. Figure 9-9 shows the waveforms and power spectra of the ring sensor with a static force of 1.96 N applied to the outer ring from different directions. The EKG and fingertip PPG data are shown for comparison. Note that no external load was applied to the EKG and fingertip PPG. While the amplitude of the ring sensor signal varied depending on the external load, the first and the second peak frequencies in the power spectra remained the same. The ring sensor's peak frequencies have no significant differences from those of the EKG and fingertip PPG, even though a static load was applied to the ring sensor.

The skin contact pressure used for the above experiments was 75 mmHg, a relatively high pressure that may block venous return, as discussed previously. To evaluate the robustness of the measurement in relation to the contact pressure, the experiments were repeated for a low contact pressure. Figure 9-10 shows the waveforms and power spectra of the ring sensor when the contact pressure was lowered to 11 mmHg. The ring sensor still shows a consistent result with regard to the first peak frequency, even though a the static load of 1.96 N was applied from two directions. However, the waveforms were completely distorted when the hand was shaken. Distorted waveforms similar to the ones in the top two plots of Figure 9-7 were obtained in this case. Therefore, the waveforms tend to be much more susceptive to hand motion as the contact pressure is lowered. As long as the ring sensor is used under stationary conditions, however, the contact pressure can be as low as 11 mmHg and still allow for reliable pulse waveforms.

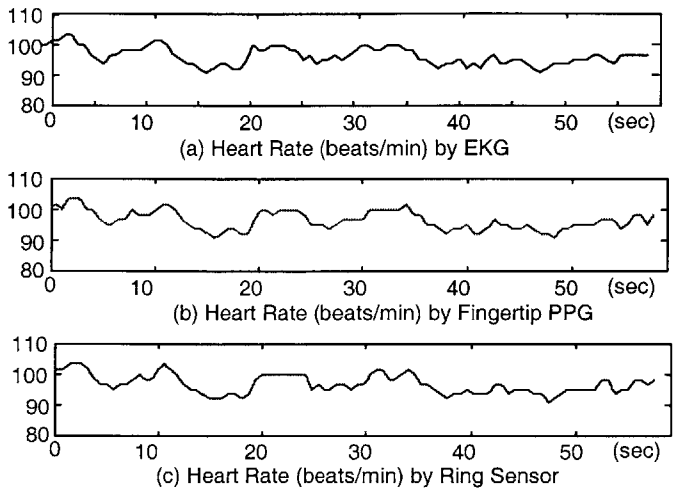

Figure 9-11 Heart rate monitored by EKG, Fingertip PPG device, ring sensor

Heart Rate Monitoring Tests

The consistent detection of the first peak frequency demonstrated in the above experiments implies that the ring sensor can be used as a beat-to-beat heart rate sensor. Figure 9-11 shows the beat-to-beat heart rate measured in the same subject when a light cardiac load was applied. The heart rate was determined by detecting the base point in each pulse and measuring the interval between adjacent base points. For benchmarking, EKG and fingertip PPG data were simultaneously recorded, and the heart rate was extracted from each signal using the standard beat-sampling technique [36]. The experiment was conducted for 60 seconds. The variation of heart rate measured by the ring sensor had a close correlation with those of the EKG and fingertip PPG. Table 9-1 shows the root mean square errors of the beat-to-beat heart rate, compared with the EKG and fingertip PPG. For a contact pressure of 75 mmHg, the difference between the ring sensor and EKG is 1.23 beats per minute, while that between it and the fingertip PPG is 1.22 beats per minute. For comparison, the table also shows the root mean square error between the EKG and fingertip PPG. The discrepancy between the ring sensor and the other two is as small as that between the EKG and fingertip PPG. When the contact pressure was lowered to 11 mmHg or increased to 146 mmHg, the discrepancy tends to increase. Nevertheless, the error is still as small as 1.6 beats per minute. These results clearly show that the ring sensor's accuracy is comparable to those of the FDA-approved devices and that the ring sensor can function even under static loads and acceleration, provided there is a proper contact pressure.

Contact pressure	EKG and Ring Sensor	Fingertip PPG and Ring Sensor	EKG and Fingertip PPG
11 mmHg	1.44	1.39	0.83
75 mmHg	1.23	1.22	0.77
137mmHg	1.41	1.27	0.96
146mmHg	1.60	1.54	0.94

Table 9-1 RMS error (beats/min) of the heart rates from the ring sensor compared with those from the EKG and fingertip PPG device

9.5 Long-Term Monitoring Experiment

Since the ring sensor was originally designed for vital sign monitoring for an extended time, a validation of the performance of the ring sensor during long-term monitoring is necessary. Although it is desirable to conduct an experiment for several days or months, a limited extended-time experiment (two hours) was performed. During this time, a healthy subject (a 30 year old male) tried mimicking everyday life: walking, writing, typing, running, and so on. Since the ring sensor monitoring system was designed to reject artifact-contaminated signals, the ring sensor will not accept any signal when the hand is moving. Therefore, if a person moves a lot, the total time that the ring sensor can properly monitor the physiological information will be shortened. On the other hand, if the person is not too active, the ring sensor can obtain quite a bit of information in a given time period. The major motivation of this experiment was to see how much time the ring sensor could obtain meaningful measurements within a specified time. Unless the ring sensor can get meaningful measurements as often as necessary, this device cannot be clinically employed. Though it is clear that the frequency of stable measurements will highly depend on each individual, this two-hour experiment gave a basic idea about how often the ring sensor can provide decent measurements in everyday life.

Figure 9-12 shows a part of the two-hour monitoring experiment. The upper figure is the raw data obtained from the ring sensor, and the bottom figure is the result after signal processing for artifact detection. The software sliced all the 2-hour data (7200 seconds) into packets of 5 seconds. The

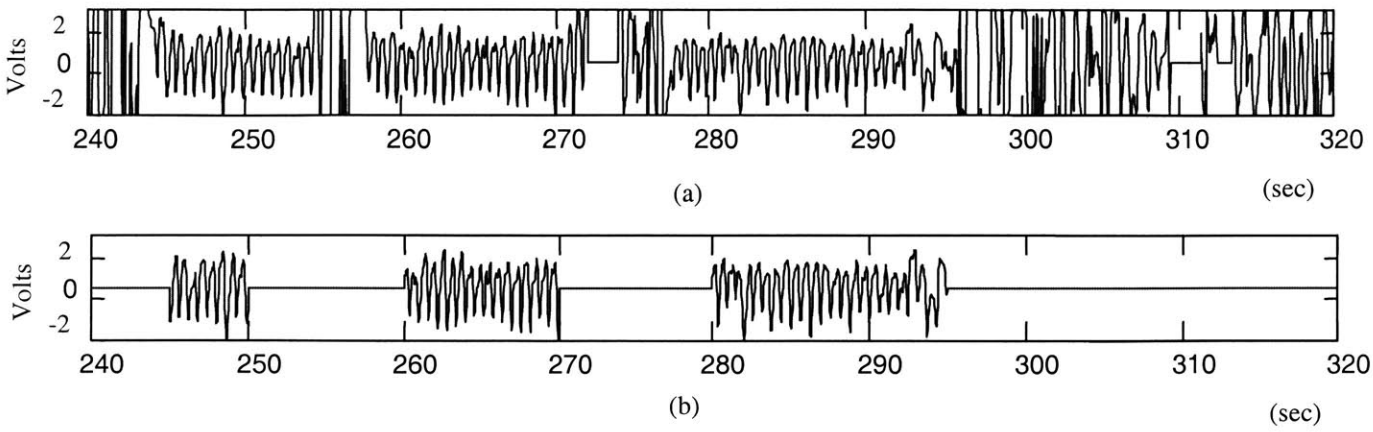

Figure 9-12 A part of the two-hour monitoring test result. The software detected motion artifact and removed the contaminated signal.

(a) Raw data of the ring sensor

(b) Data after artifact detection process

packets were endorsed to be free of artifact only when no motion artifact was detected in the 5 seconds. Applying this rather conservative algorithm, it was found that 511 packets (2555 seconds) could be marked to be "clean (free of artifact)" out of 1440 packets (7200 seconds). This means that it was possible to detect pulse information without motion artifact for 35% of the monitoring time. Of course, this number is not absolute at all since the time of stable measurement can be longer or shorter depending on the time that the hand is in stationary posture. Nevertheless, it is certain that the ring sensor can give stable measurements for a considerable portion of everyday life, and this experiment supports the fact that this device can practically provide valuable physiological information in everyday life.

9.6 Design guidelines for the ring sensor

Once we have a clear picture of the mechanism of finger photoplethysmography under various conditions, it is possible to use the result in the design process of the ring sensor. We know that there are several parameters involved in the design of the ring sensor, such as the location of the sensor, the intensity of the light source, the tension of the inner ring, and the distance between the two outer rings. The effects of variations in these parameters are generally coupled to each other and sometimes create conflicts in design. For example, increasing the tension of the inner ring will clearly make the signal less prone to noise but, on the other hand, it may block the venous return if the tension is too high, perhaps resulting in serious circulation problems in the finger. Therefore, it

is important to consider these multiple factors carefully and efficiently. There are several things to be considered during the designing of the ring sensor.

1. The tension of the inner ring must be properly adjusted. Usually, it is not recommended to make the inner ring so tight as to give a contact pressure of more than 20 mmHg. The veins usually occlude at around that pressure, as was explained previously in chapter 5.3.4. The recommended contact pressure is about 10 mmHg. At this pressure, the vascular circulation in the finger is not obstructed, and we can still get reliable measurements, as was explained in chapter 9.4. If the ring sensor is used only for a short time, the pressure can be a little higher. Even in this case, it should not exceed about 40 mmHg, which is the pressure of capillary occlusion.
2. The location of the sensor is another important parameter. To get more reliable measurements, it is better to put the sensor as close as possible to one of the palmar digital arteries. It was shown by mathematical model and experiment that you could expect a better measurement (i.e. a large signal amplitude) when you take the measurements near the digital arteries. Comparing Figure 5.24 and Figure 5.29 shows that the measurement is better when the signal is taken from the artery side, even in the low-pressure range, and this is even more apparent in the high-pressure range. Of course, it is not recommended to use a high tension of the inner ring to increase the pressure at the arteries. We can still get good optical measurements on the artery side even when the contact pressure is relatively low.
3. It is always better to have the two outer rings far away from each other. As was verified by FEM analysis in chapter 5.5, the pressure variation at the measurement point becomes smaller as the distance becomes longer. This results in a smaller variation of the detected signal when the ring sensor moves due to external force. Nevertheless, this distance cannot be very long due to the physical constraints of the hand. In other words, this distance cannot exceed the distance between two knuckles in the finger.
4. The intensity of the LED has to be carefully selected. Although it is generally better to have a high intensity, the constraints of the electrical circuitry and battery capacity do not allow this. As was discussed in detail in chapter 4 and 7.3, it is always necessary to minimize the power consumed by the LED. The conventional value of the rated capacity of lithium coin-type batteries is on the order of 100 mAh. To run the ring sensor for a long time, it is better

to keep the current consumption of the whole circuit at less than 2~3 mA on average even if we use duty rate control for the LED and the sleep mode for the circuitry. Meanwhile, the practical value of maximum discharge current of lithium coin batteries for pulse operation is around 7~10 mA. This means that the current consumed by the LED cannot exceed this value with any kind of duty rate control. Using this current, it is hard to illuminate the LED to a considerable intensity. In addition, the duty ratio of the LED on-off timing is also limited by the physical response time of the LED itself and the photodiode. In summary, it is recommended that the instantaneous current consumed by the LED should be kept around 5~7 mA, and the average power consumption should be kept under 2~3 mA by using a duty rate control of less than 1/3. After all, the power consumption of all the circuitry, including the LEDs, should be optimized following the method presented in chapter 4. If the ring sensor will be used for relatively short-term monitoring, a high LED intensity can be used.

5. It is always better to minimize the mass of the ring sensor. The bottleneck is usually the mass of batteries, since they are the heaviest components in the device. This requirement conflicts with the power consumption issue presented above, since the size of the battery need to be larger if we want more power in the LED. If the ring sensor will be used for short-term monitoring, we can put in small batteries.
6. The diameters of the outer rings are related to the ambient light and signal sensitivity to external force. To make it resistant to ambient light, it is better to make the outer ring tighter so that there will be less gap between the outer ring and the finger surface. On the other hand, if the outer ring is too tight, the dislocation of the ring sensor will result in more variation of the signal.
7. Signal filtering should be also designed considering two conflicting factors. If the filtering is heavy, the output signal will be more immune to the noise, but the waveform will be much more changed from its original shape. For example, if only the pulse rate is of interest, it is desirable to use a heavy low pass filter, or other signal processing techniques such as cross-correlation, as was described in chapter 6. If it is necessary to obtain the actual waveform of the PPG, the use of heavy filters is not recommended.

These design guidelines are summarized in Figure 9-13.

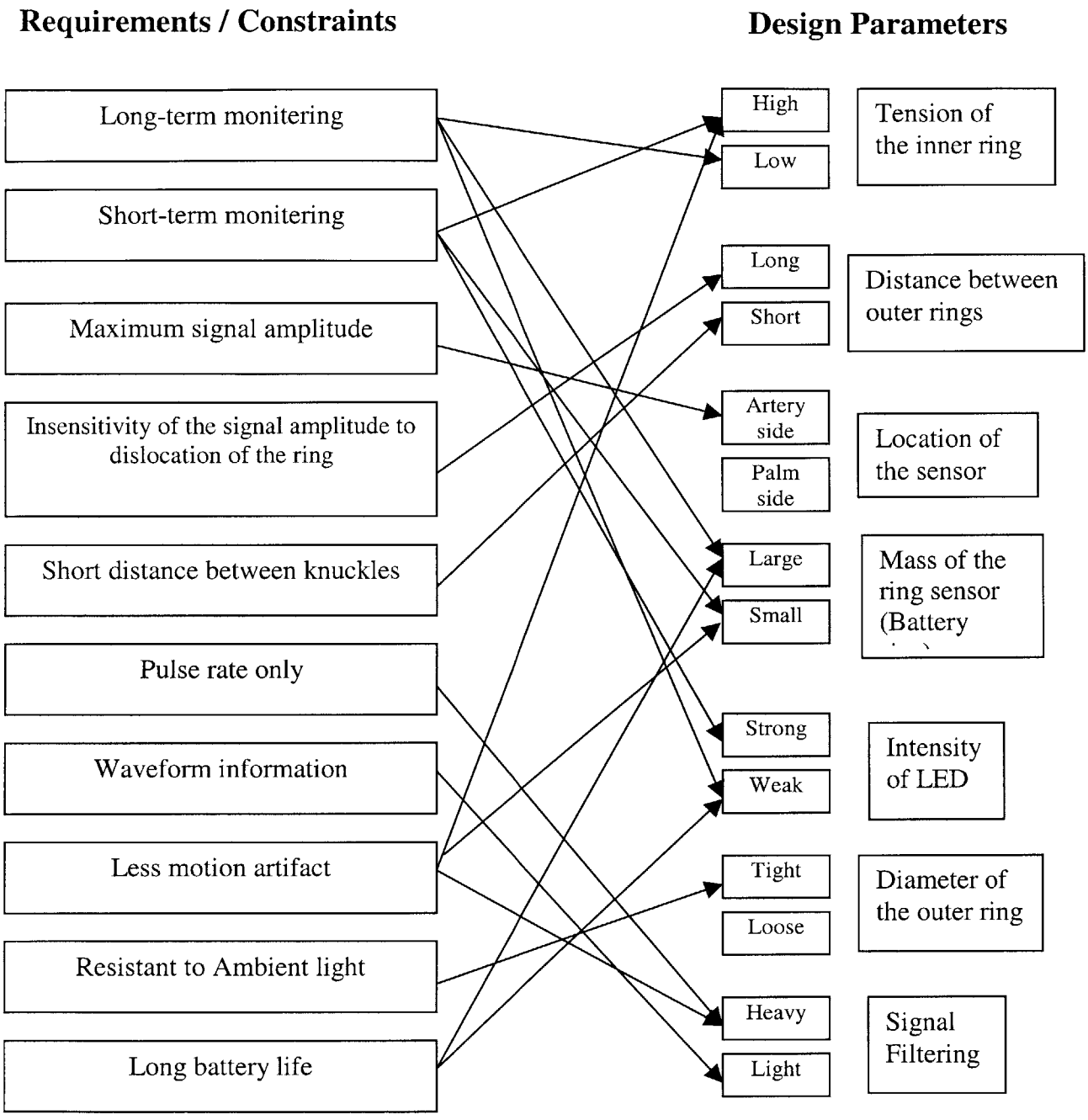

Figure 9-13 Guidelines for the design of the ring sensor

10. CONCLUSIONS

An artifact-resistive and power-efficient design of ring sensors has been presented. The main results of this thesis are:

- The isolating ring design developed in this research decouples the optical sensor unit from other components, and allows the sensor unit to be shielded from external static loads and ambient lighting. The new ring design also attenuates the influence of finger acceleration, since the heavy components are mechanically decoupled from the sensor unit. This allows us to hold the sensor unit with a small contact pressure, so that the circulation at the finger may not be obstructed.
- The power consumed in the ring sensor has been analyzed in relation to the characteristics of the individual parts, sampling rate, transmission rate, LED lighting schedule, and CPU internal clock frequencies. Based on this power budget analysis, low-power components have been selected, power-efficient LED lighting and RF transmission methods have been developed, and the optimal CPU clock frequency has been obtained.
- A finger model for the photoplethysmography of the ring sensor was developed. This model is an interdisciplinary physiological model that integrates an optical model, mechanical model, and the dynamics of the arteries and the capillaries. The parameters were tuned based on the literature and experiment results. This model was verified by the finite element method. Numerical simulations of the model showed good agreement with the experiment results. This model is especially useful in describing the nature of the finger-based health monitoring device. For example, from the viewpoint of noise minimization issues, there are many advantages to having this mathematical finger model if designing a ring sensor that is less sensitive to the noise caused by finger movements. Since there are many design parameters, such as the compliance of the inner material of the ring and the configuration of the sensor, that have to be tuned in the development of a ring sensor, this finger model will be a good analytic method of optimizing those parameters.

- A signal processing technique that can effectively detect the pulse in the existence of artifacts caused by motion and ambient light was presented. Although the autocorrelation function technique has certain limitation in itself, it shows a generally good result in rejecting non-periodic noise when combined with a classical noise reduction technique such as low pass filtering. Numerical simulation results were also presented to support this concept and they showed that this method can be used even with a low signal-to-noise ratio, which exists in the case of our ring sensor. The experiment results also showed that the periodic component of the heartbeat buried in non-periodic noise can be effectively reconstructed by this method.
- A prototype ring sensor has been designed, built, and tested. Experiments have verified that the ring sensor can detect beat-to-beat pulsation in the face of interfering force and acceleration acting on the ring body. With small battery cells, the ring sensor can continuously detect and transmit plethysmograph signals for 23.3 days, while the battery life can be extended to several months with an intermittent measurement scheduling.
- The issues concerning the miniaturization and fabrication of the ring sensor were discussed in detail. It was shown that the bulky first-generation prototype ring sensor can, indeed, be effectively reduced to the size of an ordinary ring without sacrificing any of the functionality.
- The prototype ring sensor has been benchmarked with the FDA-approved PPG and EKG. FFT spectral analysis revealed that the ring sensor is comparable to the FDA-approved devices with regard to the first and second peak frequencies of the power spectra. Furthermore, the ring sensor is comparable to those devices in the measurement of beat-to-beat pulse variations. The discrepancy is less than 1.23 pulses per minute in RMS value. The experiment results also showed that a relatively low pressure of around 10 mmHg can be effectively used for inner ring, and still guarantees stable waveform measurement even under external static force.
- The two-hour continuous monitoring experiment showed that the ring sensor could effectively provide artifact-free vital sign information for a considerable portion of everyday life.
- Finally, guidelines for the design of the ring sensor were proposed based on the analyses and the experiments.

The theoretical analysis, experimental data and benchmarking tests have demonstrated that the ring sensor can be used as a wearable sensor for the long-term, continual monitoring of patients in the home and other environments.

REFERENCES

[1] D. David, E.L. Michelson, and L.S. Dreifus, "Ambulatory Monitoring of the Cardiac patient," Philadelphia, U.S., 1988, F.A. Davis Company, Chapter 1

[2] N.J. Holter, "New method for heart studies : Continuous electrocardiography of active subjects over long periods is now practical," Science 134:1214, 1961

[3] S. Bellet, L. Roman, J. Kostis, st al : Continuous electrocardiographic monitoring during automobile driving," Am J Cardiol 22:856, 1968

[4] M. Yamashita, K. Shimizu, and G. Matsumoto, "Development of a Ring-Type Vital Sign Telemeter," Biotelemetry XIII, 1995

[5] Barker, S. J. and Shah, N. K., "The Effect of Motion on the Performance of Pulse Oximeters in Volunteers," Anesthesiology, 86, 101-108 (1997)

[6] Plummer, J. L., Zakaria, A. Z., Ilsley, A. H., Fronsko, R. R. L. and Owen, H., "Evaluation of the Influence of Movement on Saturation Readings from Pulse Oximeters," Anaesthesia, 50, 423-426 (1995)

[7] Vicente, L. M., Barreto, A. B. and Taberner, A., "Adaptive Pre-Processing of Photoplethysmographic Blood Volume Pulse Measurements," Southern Biomedical Engineering Conference - Proceedings Mar 29-31 1996 Sponsored by:University of Dayton; IEEE IEEE p 114-117

[8] Higgins, J. L. and Fronek, A., "Photoplethysmographic Evaluation of the Relationship between Skin Reflectance and Skin Blood Volume," Journal of Biomedical Engineering, Vol 8,April, 130-136 (1986)

[9] Shimazu, H., Kawarada, A., Ito, H. and Yamakoshi, K., "Electric Impedance cuff for the indirect measurement of blood pressure and volume elastic modulus in human limb and finger arteries," Medical & Biological Engineering & Computing, 1989, 27,477-483

[10] Shimazu, H., Ito, H. and Yamakoshi, K., "Noninvasive method for estimating the mean capillary pressure and pre- and postcapillary resistance ratio in human fingers," Medical & Biological Engineering & Computing, 1986, 24,585-590

[11] Wesseling, K. H., de Wit, B., van der Hoeven, G. M. A., van Groudoever, J. and Settels, J. J., "Physiocal, Calibrating Finger Vascular Physiology for Finapres," Homeostatis, 36

(2-3), 67-82 (1995)

[12] Rhee, S., Yang, B-H. and Asada, H., "The Ring Sensor: a New Ambulatory Wearable Sensor for Twenty-Four Hour Patient Monitoring," Proc. of the 20th Annual International Conference of the IEEE Engineering in Medicine and Biology Society, Hong Kong, Oct, 1998

[13] Yang, B-H., Rhee, S. and Asada, H., "A Twenty-Four Hour Tele-Nursing System Using a Ring Sensor," Proc. of 1998 IEEE International Conference on Robotics and Automation, Leuven, Belgium, May, 1998

[14] M. Kosiak, "Etiology of Decubitus Ulcers," Archives of Physical Medicine and Rehabilitation Vol 42 : 19-29, 1959

[15] S.M. Dinsdale, "Mechanical Factors in Pathogenesis of Ischemic Skin Ulcers in Swine," Thesis, University of Minnesota, 1970

[16] R.K. Daniel, D.L. Priest and D.C. Wheatley, "Etiologic Factors in Pressure Sores : An Experimental Model," Archives of Physical Medicine and Rehabilitation Vol 62 : 492-498, 1981

[17] M.S. Rendell and J.M. Wells, "Ischemic and Pressure-Induced Hyperemia : A Comparison," Archives of Physical Medicine and Rehabilitation Vol 79 : 1451-1455, 1998

[18] M.J. Hayes, P.R. Smith, D.M. Barnett, M.D.L. Morgan, S. Singh, D.D. Vara, "Quantitative investigation of artefact in photo-plethysomgraphy and pulse-oximetry for respiratory excercise testing.", Frontiers in computer-aided visualization of vascular functions, Proc CNVD 97, VDI, 1998, 117-124.

[19] Takatani, S. and Graham, M.D., "Theoretical Analysis of Diffuse Reflectance from a Two-Layer Tissue Model," IEEE Transactions on Biomedical Engineering, Vol. 26, No. 12, December 1979, 656-664

[20] Feng, S., Zeng, F. and Chance, B., "Photon Migration in the Presence of a Single Defect : a Perturbation Analysis," Applied Optics, Vol. 34, No. 19, 3826-3837 (1995)

[21] Dai, G., Gertler, J. P. and Kamm, R. D., "The Effect of External Compression on Venous Blood Flow and Tissue Deformation in the Lower Leg," Journal of Biomedical Engieering, December 1999, Vol. 121, 557-564

[22] Maeno, T., Kawai, T. and Kobayashi, K., "Analysis and Design of a Tactile Sensor

Detecting Strain Distribution Inside an Elastic Finger," Proceedings of the 1998 International Conference on Intelligent Robotics and Systems, Victoria, B.C., Canada 1658-1663

[23] Srinivasan, M.A. and Dandekar, K., "An Investigation of the Mechanics of Tactile Sense Using Two-Dimensional Models of the Primate Fingertip," Journal of Biomechanical Engineering, Feb.1996, Vol. 118, 48-55

[24] Raju, B., "Encoding and Decoding of Shape in Tactile Sensing," MS Thesis, Department of Mechanical Engineering, Massachusetts Institute of Technology, 1998

[25] Vannah, W.M.. and Childress, D.S., "Indentor tests and finite element modeling of bulk muscular tissue in vivo," Jornal of Rehabilitation Research and Development, Vol. 33, No. 3, July 1996, pp. 239-252

[26] Van Assendelft, O.W., "Spectrophotometry of Hemoglobin Derivatives," Assen, The Netherlands: Royal Vangorcum, 1970, ch. 3, pp. 47-151

[27] Hull, E.L., Nichols, M.G. and Foster, T.H., "Quantitative broadband near-infrared spectroscopy of tissue-simulating phantoms containing erythrocytes," Physics in Medicine and Biology, 43 (1998) 3381-3404

[28] Wagnieres, G., Cheng, S., Zellweger, M., Utke, N., Braichotte, D., Ballini, J. and Bergh, H., "An optical phantom with tissue-like properties in the visible for use in PDT and fluorescence spectroscopy," Physics in Medicine and Biology, 42 (1997) 1415-1426

[29] Landis, E.M. and Pappenheimer, J.R., "Exchange of Substances through the capillary walls," In Handbook of Physiology, Hamilton, W.F. and Dow, P. (Eds), 1963, 961-1034

[30] Tanaka, H. and Thulesius, O., "Effect of Temperature on Finger Artery Pressure Evaluated by Volume Clamp Technique," Clinical Physiology (1993) 13, 535-545

[31] Ando, J., Kawarada, A., Shibata, M., Yamakoshi, K. and Kamiya, A., "Pressure-volume Relationships of Finger Arteries in Healthy Subjects and Patients with Coronary Atherosclerosis Measured Non-invasively by Photoelectric Plethysmography," Japanese Circulation Journal, Vol. 55, June 1991, 567-575

[32] Yamakoshi, K., Shimazu, H., Shibata, M. and Kamiya, A., "New Oscillometric Method for Indirect Measurement of Systolic and Mean Arterial Pressure in the Human Finger. Part 1 : Correlation Study," Medical & Biological Engineering & Computing (1982), 20, 307-313

[33] Raamat, R., Talts, J., Jagomagi, K. and Lansimies, E., "Methematical modeling of non-invasive oscillometric finger mean blood pressure measurement by maximum oscillation criterion," Medical & Biological Engineering & Computing, 1999, 37, 784-788

[34] Shimazu, H., Ito H., Kawarada, A., Kobayashi, H., Hiraiwa, A. and Yamakoshi, K., "Vibration technique for indirect measurement of diastolic arterial pressure in human fingers," Medical & Biological Engineering & Computing, 1989, 27,130-136

[35] Langewouters, G.J., Zwart, A., Busse, R. and Wesseling, K.H., "Pressure-diameter relationships of segments of human finger arteries," Clinical Physics and Physiological Measurement, 1986, Vol. 7, No. 1, 43-55

[36] J. D. Pruett, J. D. Bourland, and L. A. Gedded, "Measurement of Pulse-Wave Velocity using a Beat-Sampling Technique," Annals of Biomedical Engineering, Vol. 16, pp. 341-347, 1988

[37] Yamakoshi, K., Shimazu, H., Shibata, M. and Kamiya, A., "New Oscillometric Method for Indirect Measurement of Systolic and Mean Arterial Pressure in the Human Finger. Part 2 : Correlation Study," Medical & Biological Engineering & Computing (1982), 20, 314-318

[38] Serina, E.R., Mockensturm, E., Mote, C.D. and Rempel, D., "A structural model of the forced compression of the fingertip pulp," Journal of Biomechanics, 31 (1998), 639-646

[39] Mendelson, Y. and Ochs, B.D., "Noninvasive Pulse Oximetry Utilizing Skin Reflectance Photoplethysmography," IEEE Transactions on Biomedical Engineering, Vol. 35, No. 10, October 1988, 798-805

[40] Gemert, V., Jacques, S.L., Sterenborg, M. and Star, W.M., "Skin Optics," IEEE Transactions on Biomedical Engineering, Vol. 36, No. 12, December 1989, 1146-1154